Numerical simulation of measured neutron signals for plasma diagnostics on tokamaks

Björn Wolle

IPP III/222 August 1997

MAX-PLANCK-INSTITUT FÜR PLASMAPHYSIK

85748 GARCHING BEI MÜNCHEN

MAX-PLANCK-INSTITUT FÜR PLASMAPHYSIK
GARCHING BEI MÜNCHEN

Numerical simulation of measured neutron signals for plasma diagnostics on tokamaks

B. Wolle

IPP III/222 August 1997

Die nachstehende Arbeit wurde im Rahmen des Vertrages zwischen dem Max-Planck-Institut für Plasmaphysik und der Europäischen Atomgemeinschaft über die Zusammenarbeit auf dem Gebiet der Plasmaphysik durchgeführt.

REVIEW ARTICLE

Numerical simulation of measured neutron signals for plasma diagnostics on tokamaks

B Wolle

Institut für Angewandte Physik, Universität Heidelberg, D-69120 Heidelberg, Germany

Abstract. Neutron diagnostics are of increasing importance for future fusion devices. Consequently, efforts are being made to improve the accuracy of underlying experimental and computational methods. The present article reviews the modelling and the analysis of measured neutron signals relevant for plasma diagnostics on tokamaks. The underlying numerical simulation of neutron signals involves various aspects. Firstly, a realistic characterization of the plasma as a neutron source is needed. Secondly, detailed knowledge about changes in energy spectra and total number of the initially emitted neutrons due to scattering and absorption in the volume between neutron source and detector system is required. Finally, the detection properties of the measuring systems have to be taken into account. Presently, a sophisticated numerical procedure which directly relates detector signals to physics properties of the emitted neutrons from the plasma is not available and progress is found to be incremental rather than revolutionary. This is mainly attributable to problems with modelling the plasma neutron source based on measured plasma data and modelling difficulties for the neutron transport. However, more recent results of plasma parameters derived from neutron measurements provide evidence for the improvements in the measurement, simulation and analysis procedures over the past two decades.

Contents

1. Introduction

During the past few decades intensive research has been undertaken in plasma physics, and in particular in the field of thermonuclear fusion. As a result, the field includes a very substantial body of knowledge ranging from the most theoretical to the most practical topics. Progress has been made most effectively when an early confrontation between theory and experiment has been possible. However, such comparisons require both, theoretical calculations for realistic configurations and conditions, as well as rather detailed and accurately measured plasma properties. For this reason much of the effort in experimental plasma physics is devoted to developing, providing and proving the experimental techniques and the associated theoretical and computational techniques for diagnosing the properties of fusion plasmas.
Fusion plasmas can be divided into two kinds: those produced by rapid compression of small fuel pellets by light or ion beams (inertial confinement fusion), and those confined by strong magnetic fields (magnetic confinement fusion). Over the past decades the international magnetic confinement fusion research programme has been mainly focusing on to tokamak fusion devices. The world's largest magnetic fusion experiments, present and planned, are of this type. Therefore, this review shall be concerned only with tokamak fusion plasmas.

1.1. Neutron diagnostics on tokamak fusion experiments

Measurements of the neutron emission were carried out at very early stages in thermonuclear fusion research as the number of produced neutrons is a direct measure of the progress towards the achievement of thermonuclear reactor conditions. Since other more conventional diagnostic systems are not capable to operate quasi-continuously under the high neutron and gamma-ray fluences of a thermonuclear reactor or require substantial radiological shielding, neutron diagnostics are of increasing importance for future fusion devices. For instance, at the planned international thermonuclear experimental reactor ITER (see e.g. Rebut *et al* 1995), neutron diagnostics will play a prominent role in the control and evaluation of thermonuclear plasmas (Johnson *et al* 1997). Thus, efforts are being made to improve the accuracy of underlying experimental and computational methods. Neutron measurement techniques suitable for nuclear fusion devices are based on sophisticated developments originally made for fission reactors and in experimental neutron physics (see Knoll 1989). However, on fusion experiments neutron detectors have to operate in somewhat unusual conditions for neutron physics and require the following additional specifications:

(a) insensitivity to the magnetic field,

(b) low sensitivity to gamma rays,
(c) ability to operate with high neutron fluences,
(d) tolerance of electromagnetic disturbances,
(e) ability to withstand mechanical vibrations,
(f) rapid processing of the measurement signals, and
(g) ability to operate within the wide energy range of the neutron field.

The variety of neutron measurements that can be made on fusion experiments is limited to measuring the total emission strength, the relative spatial emissivity in the plasma, and the energy spectra of neutrons emitted from small plasma volumes or from selected lines-of-sight through the plasma. Furthermore, for obtaining a time-resolution suitable for diagnostics on fusion experiments some relevant measurement techniques require neutron fluxes which are achievable only with the larger experimental devices.
Historically, the year 1981 can be regarded as a turning point or maybe even marks the birth of modern neutron diagnostics on tokamak experiments. In this year, the TRANSP code (Goldston *et al* 1981) became available, the first activation measurements were carried out at PLT (Zankl *et al* 1981), and a time-of-flight spectrometer suitable for diagnostics of extended fusion plasmas was presented (Elevant *et al* 1981). Then, the third version of the neutron transport code MCNP was released in 1983 which was the first version of this code that has been internationally distributed (cf. Briesmeister 1993). Furthermore, with the construction and operation of larger fusion experiments of type tokamak such as PLT, ASDEX and JET (see e.g. Wesson 1987) neutron measurements could be used efficiently for plasma diagnostic purposes. Most of the pioneering experimental work relevant for routinely using neutron diagnostics on tokamaks has been carried out at JET (Jarvis 1994).

1.2. General overview

In the plasma physics literature results of neutron diagnostics are normally organized by experimental technique or by predictive numerical calculations of fusion neutron production, which to some extent obscures the view on the general progress. Therefore, the main motivation of this article is to try to provide a logical link between the basic physics of a tokamak plasma as a neutron source and the diagnosticians who are mainly interested in the deduction of characteristic plasma parameters from neutron measurements. Since experimental results for 14 MeV neutrons from D-T operation are, as yet, only available from TFTR (Strachan *et al* 1994) and JET (JET team 1992), this article is devoted to reviewing the numerical modelling and analysis techniques of 2.5 MeV D-D neutron measurements for inference of relevant plasma data on tokamaks. Therefore, it is not appropriate to include other areas of nuclear fusion research, such as e.g. inertial

confinement fusion, in which neutron measurements and simulation analysis are carried out (see e.g. Moran and Hall 1997, Nakai *et al* 1996).

In plasma experiments neutrons are being produced by nuclear reactions of the fuel ions. The absolute number and the energy spectrum of these neutrons is, in a somewhat complicated manner, related to the plasma conditions where the neutrons are being born. Being uncharged the neutrons instantly leave the plasma in their original direction of emission. Then, they hit structural components of the experimental device and its measuring systems. The neutrons will be scattered and to some extent absorbed. As a result, the initial direction of emission, the initial energy spectrum, and the number of neutrons is altered.
Finally, some neutrons reach a neutron detector system and, with a certain probability, produce a signal. The properties of this signal depends on the properties of the incident neutrons as well as on the detector properties. It is the objective of neutron diagnostics to obtain as much information as possible on the properties of the plasma fuel ions by analysing these measured neutron signals.

Optimal performance and use the different neutron diagnostic systems involves various aspects and requires three different layers of computational procedures. Firstly, there are the fast dedicated computer programs for the primary data evaluation and for processing the directly measured neutron signals of each detector system. Such computer programs are usually regarded to be part of the measurement systems and will, therefore, not be discussed in this article.
Secondly, computer codes for neutron transport calculations are needed in order to assess the influence of neutron scattering and absorption on the measured neutron signals. Neutron transport simulation plays an important role for the calibration of the different detector systems, in particular the neutron flux detectors. The normal procedure is to simulate the effects of neutron scattering and absorption on the detector signals once, and then simply correct the actual measurement. This implies that the corrections are sufficiently small and do not change from measurement to measurement. Therefore, and because of the errors in the simulations, much effort in experimental neutron diagnostics is devoted to minimize the influence of these effects on the actual measurement. Since neutron transport simulations provide more than enough material for a separate review, it is not appropriate to include a detailed overview on the field in the present article.
Thirdly, there have to be computer codes for interpretation of the measurements. Interpretation codes are needed to deduce plasma parameters such as deuteron densities and temperatures out of the measured neutron signals.

Routine interpretations of neutron signals aimed at obtaining information on basic

plasma parameters such as densities and temperatures requires fast dedicated computer codes. For routine analysis of neutron signals, there are mainly two different approaches. Firstly, one can build up a data base by calculating the expected measured neutron signals for various plasma properties and experimental conditions. By comparing the measured signal with the pre-calculated results, one can narrow down the physical parameter space and deduce relevant plasma parameters. However, the results are, in general, ambiguous because different input parameters can yield indistinguishable neutron signals. In the second approach, by employing relevant physical boundary conditions, the analysis is restricted to the most relevant of the possible physical parameter spaces. Further restriction is obtained by choosing a set of plasma data which are sufficient to describe the most important features of the plasma neutron source. Then, using this likely set of plasma data, the neutron signal is calculated. By comparing measured and calculated results in an iterative procedure, the values of the plasma parameters can be found for which consistency between the measurement and the physical assumptions can be achieved.

Clearly, in each of the two different approaches given above, the neutron production has to be calculated. Therefore, in chapter 2 the necessary underlying theoretical background for the plasma as a neutron source is provided. It starts with a brief overview on fusion reactions and cross sections, the calculation of fusion reactivities and neutron spectra. Only foundations are laid out and a few worked out examples are given. For more technical details the reader is, therefore, referred to the original papers.

Interpretation calculations using the measured neutron signals directly as input in order to extract plasma parameters of interest can be carried out by modelling of the ion velocity distribution. For thermal plasmas this is a straightforward procedure. In order to treat auxiliary heated plasmas, it is important to use models which describe non-Maxwellian velocity distributions with sufficient accuracy but, at the same time, are not too time-consuming. Such models are, at present, only available for neutral-beam heated plasmas. Therefore, the remainder of chapter 2 is mainly concerned with the numerical modelling of ion velocity distributions in the presence of neutral-beam heating by means of a Fokker-Planck formalism.

Chapter 3 is devoted to the simulation of the D-D neutron emission in tokamaks. Firstly, the basic physics input requirements for a sophisticated interpretation calculation are summarized. Accurately measured basic plasma data and neutron signals are needed as input data. As a direct link with the experimental practice, known sources of systematic errors for emission rate and interpretation calculations are discussed. Some other input data such as the neutral beam deposition profile have to be calculated by means of fast dedicated codes which also use measured plasma data as input. Therefore, an overview on the concepts and available computer codes for calculating neutral-beam deposition data is given. The remainder of chapter 3 is concerned with computer codes for cal-

culating D-D neutron rates, the numerical modelling of neutron spectra, and, briefly, neutron transport simulations.

The last part of the article is devoted to reviewing the plasma physics deductions that can be made by analysing measured neutron signals. Emphasis is placed on simulation analysis of neutron source strength measurements as the majority of inferred plasma data pertains to this area. Neutron diagnostics may be used to test the classical nature of the fast-particle slowing-down process and, thus, validate the simplified kinetic models used for simulation. Furthermore, results for deriving deuteron densities, ion temperatures and electron temperatures out of measured neutron signals for ohmically and neutral-beam-heated plasmas are summarized. In addition, the determination of the minority ion concentration and ion diffusivities out of neutron measurements are discussed. As an example of more general plasma physics results, the impact of neutron diagnostics on the study of MHD activities is outlined.

Finally, in chapter 5, the progress of the field towards the use of neutron diagnostics as the standard diagnostics for future fusion experiments and reactors is summarized and the likely directions of future research are indicated.

2. Basic theory

Many important measurable macroscopic plasma quantities can be written as moments of the velocity distribution function $f(\boldsymbol{v})$ as

$$\langle \boldsymbol{v}^k \rangle = \int f(\boldsymbol{v}) \boldsymbol{v}^k \mathrm{d}^3\boldsymbol{v}$$

where the quantity $\langle \boldsymbol{v}^k \rangle$ is the kth-order moment. If the moments for all $k = 0$ to ∞ are known, then the velocity distribution is completely determined. However, often knowledge of only the lower order moments is sufficient to provide information about the plasma. In particular if the plasma is close to local thermodynamic equilibrium, then the local distribution function is approximately Maxwellian and the measurable lower order moments, viz., density, average velocity, pressure, describe the plasma with sufficient detail. If the plasma is not close to thermal equilibrium, which is e.g. the case when high power auxiliary heating is employed, then the moments still provide valuable information, but the complete description of the plasma then requires knowledge about the non-Maxwellian distribution function explicitly. Such non-Maxwellian velocity distributions depend on many quantities such as the character of ion sinks and sources, different plasma parameters, and the magnetic field configuration. Furthermore, a knowledge of the non-Maxwellian velocity distributions of the plasma particles is required for studying problems connected with plasma heating and stability or for calculating important quantities such as the collisional power transfer to the background plasma, fusion reaction rates and fusion products spectra.

The fusion products of nuclear reactions occurring within the plasma can be used as a convenient diagnostic for the ions. For this purpose the neutron is the reaction product of most interest since, being uncharged, it is able to escape immediately from the plasma and, hence, can be detected. Neutron diagnostics involve the experimental neutron detection techniques and the (computational) techniques for extracting relevant information about the velocity functions of the fusing ions out of the measured neutron signals. In this chapter the necessary theoretical background for describing the plasma as a neutron source is provided.

In the first part of this chapter, a brief overview over the fusion reactions, the cross sections, the calculation of fusion reactivities and spectra is given. As illustrative examples, analytic results for Maxwellian deuterium plasmas have been included.

In the case of non-Maxwellian plasmas the neutron rates or neutron spectra are no longer simple analytic functions of the plasma temperature. Thus, analytic treatment is not suited for theoretical calculations or the analysis of actual measured neutron signals. Instead, the problem has to be tackled numerically involving the calculation of realistic velocity distributions taking into account the necessary physical properties of the plasma. Therefore, the remainder of this chapter is devoted to the kinetic descrip-

tion of a tokamak plasma by means of a Fokker-Planck formalism which is sufficiently accurate and allows fast numerical solution.

2.1. Theoretical background of the fusion neutron emission

The emitted neutron rate from a plasma is a weighted average of the velocity distribution with cross section and relative velocity and the neutron spectrum is simply the energy dependent probability of neutron emission per steradian. The present article focuses mainly on the simulation and interpretation of neutron signals from D-D reactions. Therefore, other fusion reactions are only briefly described for completeness.

2.1.1. Fusion reactions

The main fusion reactions in a tokamak plasma relevant for neutron diagnostics are the following:

$$\mathrm{D} + \mathrm{D} \rightarrow \mathrm{t}\ (1.01\ \mathrm{MeV}) + \mathrm{p}\ (3.02\ \mathrm{MeV}) \qquad Q = 4.03\ \mathrm{MeV} \tag{1}$$

$$\mathrm{D} + \mathrm{D} \rightarrow {}^{3}\mathrm{He}\ (0.82\ \mathrm{MeV}) + \mathrm{n}\ (2.45\ \mathrm{MeV}) \qquad Q = 3.27\ \mathrm{MeV} \tag{2}$$

$$\mathrm{D} + \mathrm{T} \rightarrow {}^{4}\mathrm{He}\ (3.56\ \mathrm{MeV}) + \mathrm{n}\ (14.03\ \mathrm{MeV}) \qquad Q = 17.59\ \mathrm{MeV} \tag{3}$$

$$\mathrm{D} + \mathrm{t} \rightarrow {}^{4}\mathrm{He} + \mathrm{n} \qquad Q = 17.59\ \mathrm{MeV} \tag{3a}$$

$$\mathrm{T} + \mathrm{T} \rightarrow {}^{4}\mathrm{He}\ (3.78\ \mathrm{MeV}) + 2\mathrm{n}\ (7.56\ \mathrm{MeV}) \qquad Q = 11.34\ \mathrm{MeV}. \tag{4}$$

Here, the hydrogenic species are represented by upper case letters for reacting ions and by lower letters for fusion products. In the above given equations, the reaction Q-values and, in addition, the particle energies for zero-energy reactants are given where appropriate. In present-day fusion devices with magnetically confined plasmas experiments are usually carried out with deuterium fuel for simulation of reactor plasmas and the employment of neutron diagnostics. At the JET tokamak experiments with deuterium plasmas and a small amount of tritium have been performed (JET team, 1992) and, recently, longer experimental campaigns using a reactor relevant deuterium and tritium fuel mixture have been carried out at TFTR (Strachan *et al* 1994). The two branches of the D-D reaction occur with nearly equal probability. Equation (3a) relates to fusion reactions undergone by the fusion product tritons from the first branch of the D-D reaction and is commonly referred to as triton burn-up reaction. The study of triton burn-up is of particular interest since the emission of 2.5 MeV neutrons is indicating the birth of the 1.0 MeV tritons and the signal of the 14 MeV neutrons provides information on the confinement, slowing-down and radial migration of these particles (see, e.g., Strachan *et al* 1996). The 1.0 MeV tritons have Larmor radii close to those of 3.5 MeV alpha particles from the D-T reaction and exhibit similar slowing-down and confinement properties. Therefore, in plasmas with large D-D reaction rates,

triton burn-up measurements provide a frequently used method to investigate the single particle behaviour of alpha particles in tokamaks without having to introduce tritium into the experimental devices. It should be mentioned that under these experimental conditions the neutron production due to the T-T reaction can be neglected since the triton population is by several orders of magnitude smaller than that of the deuterons in a deuterium plasma.

2.1.2. Fusion cross sections

The interpretation of neutron source strength measurements in present fusion devices or the prediction of the fusion power gain of future experiments requires accurate knowledge of the relevant fusion cross sections. In particular, since measured fusion rates are of increasing importance for plasma diagnostics on large fusion experiments, the uncertainties in the cross sections are required to be of the order or less than the errors in neutron source strength measurements.
Since about 1945 many measurements of the fusion cross sections have been carried

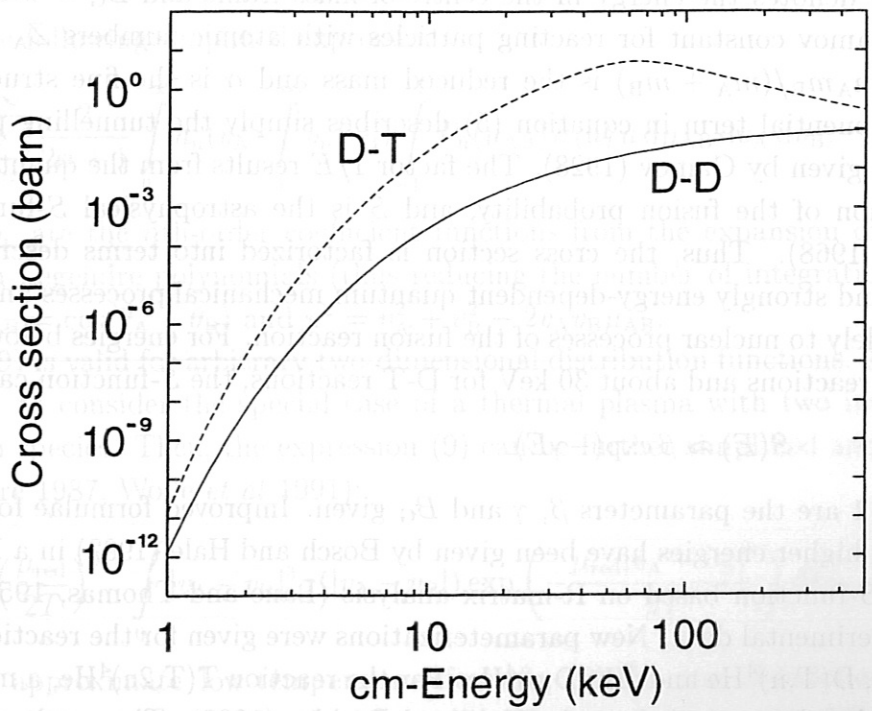

Figure 1. Fusion cross sections for the fusion reactions $D(D,n)^3He$ (——) and $D(T,n)^4He$ (- - - -) as a function of energy in the centre-of-mass frame.

Table 1. Low energy parametrization of the cross section in the centre-of-mass system.

Reaction	β (barn keV)	γ (keV^{-1})	B_G ($\mathrm{keV}^{1/2}$)
D-D	52.6	-5.8×10^{-3}	31.3970
D-T	9821	-2.9×10^{-2}	34.3827

out. However, reliable experimental data are not available for energies below about 10 keV and even for the limited experimental energy range available the measurements are not always in agreement. Therefore, it is necessary to extrapolate downwards using theoretical formulae. Furthermore, analytical representations of the fusion cross sections are desirable for calculations of fusion reaction rates. As shown in figure 1, the cross section varies over more than 10 orders of magnitude over the energy range 1–500 keV. Due to the strong dependence on the particle energy it has been found most convenient to represent the cross section as

$$\sigma(E) = S(E)\frac{1}{E}\exp(-B_\mathrm{G}/\sqrt{E}) \tag{5}$$

where E denotes the energy in the centre-of-mass frame and $B_\mathrm{G} = \pi\alpha Z_\mathrm{A} Z_\mathrm{B}\sqrt{2\mu_\mathrm{red}c^2}$ is the Gamov constant for reacting particles with atomic numbers Z_A and Z_B. Here, $\mu_\mathrm{red} = m_\mathrm{A} m_\mathrm{B}/(m_\mathrm{A} + m_\mathrm{B})$ is the reduced mass and α is the fine structure constant. The exponential term in equation (5) describes simply the tunnelling probability and was first given by Gamov (1928). The factor $1/E$ results from the quantum mechanical description of the fusion probability, and S is the astrophysical S-function (see e.g. Clayton 1968). Thus, the cross section is factorized into terms describing the well-known and strongly energy-dependent quantum mechanical processes and a term which refers solely to nuclear processes of the fusion reaction. For energies below about 90 keV for D-D reactions and about 30 keV for D-T reactions, the S-function can be written as

$$S(E) \approx \beta\exp(-\gamma E). \tag{6}$$

In table 1 are the parameters β, γ and B_G given. Improved formulae for the cross sections for higher energies have been given by Bosch and Hale (1992) in a Padé expansion for the S-function based on R-matrix analysis (Lane and Thomas, 1958) of the available experimental data. New parameterizations were given for the reactions D(D,n)^{3}He, D(D,p)t, D(T,n)^{4}He and ^{3}He(D,p)^{4}He. For the reaction T(T,2n)^{4}He, a mass-6 R-matrix analysis has been carried out by Hale and Dodder (1980). The result agrees well with new accurate measurements by Jarmie (1986).

2.1.3. Fusion reactivities

The local fusion reaction rate R for a plasma containing ion species of type A and B is given by

$$R = \frac{n_A n_B}{1+\delta_{AB}} \langle \sigma v \rangle_{AB} \tag{7}$$

where n_A and n_B are the particle densities and δ_{AB} is the Kronecker symbol. The reactivity $\langle \sigma v \rangle_{AB}$ is in general given by the six-dimensional integral

$$\langle \sigma v \rangle_{AB} = \iint f_A(\boldsymbol{v}_A) f_B(\boldsymbol{v}_B) \sigma \left(|\boldsymbol{v}_A - \boldsymbol{v}_B| \right) |\boldsymbol{v}_A - \boldsymbol{v}_B| \, \mathrm{d}\boldsymbol{v}_A \mathrm{d}\boldsymbol{v}_B \tag{8}$$

where f_A,f_B are the normalized velocity distributions of the reacting particles, σ is the cross section and $|\boldsymbol{v}_A - \boldsymbol{v}_B|$ is the velocity of impact. Cordey *et al* (1978) showed that for this integration considerable analytic simplification can be achieved by choosing a spherical coordinate system for velocity space and assuming azimuthal symmetry. With the assumption of azimuthal symmetry, the distribution functions are of the form $f_K(v, \mu)$, where $v = |\boldsymbol{v}|$ and $\mu = v_\parallel / v = \cos\theta$ is the cosine of the pitch angle, and can be expanded in Legendre polynomials P_n as:

$$f_K(v, \mu) = \sum_{n=0}^{\infty} k_n(v) P_n(\mu).$$

One obtains the following simplified expression:

$$\langle \sigma v \rangle_{AB} = 4\pi^2 \sum_{n=0}^{\infty} \frac{2}{2n+1} \int_0^{\infty} a_n(v_A) \int_0^{\infty} b_n(v_B) \int_{-1}^{1} P_n(\mu_{AB}) \, \sigma(u) \, u \, \mathrm{d}\mu_{AB} \, \mathrm{d}v_A \, \mathrm{d}v_B. \tag{9}$$

Here, a_n and b_n are the nth-order coefficient functions from the expansion of the ion distributions in Legendre polynomials (thus reducing the number of integrations to be performed), $\mu_{AB} = \cos(\theta_A - \theta_B)$ and $u^2 = v_A^2 + v_B^2 - 2 v_A v_B \mu_{AB}$.

Equation (9) is valid for arbitrary two-dimensional distribution functions. However, it is of interest to consider the special case of a thermal plasma with two interacting Maxwellian ion species. Then, the expression (9) can be further simplified and reduces to (see e.g. Core 1987, Wolle *et al* 1991):

$$\langle \sigma v \rangle_{AB} = \frac{2}{\sqrt{\pi}} \left(\frac{\mu_{red}}{2T} \right)^{3/2} \int_0^{\infty} |v_A - v_B|^3 \sigma(|v_A - v_B|) \exp\left(- \frac{\mu_{red} |v_A - v_B|^2}{2T} \right) \mathrm{d}|v_A - v_B|. \tag{10}$$

On using the approximate low-temperature formula (6) for the S-function in the expression (5) of the cross section, the Maxwellian fusion reactivity simplifies to (see e.g. Jarvis 1994):

$$\langle \sigma v \rangle_{AB} = k_{AB} T^{-2/3} \exp(-\lambda T^{-1/3}) \approx k_{AB} T^{\kappa}$$

Table 2. Parameters for the thermal reactivity fit given by Bosch and Hale for the D(D,n)^{3}He and the D(T,n)^{4}He fusion reactions.

Coefficient	Reaction	
	D(D,n)^{3}He	D(T,n)^{4}He
$\mu_{\rm red}c^2$ (keV)	937 814	1 124 656
c_1	5.43360×10^{-12}	1.17302×10^{-9}
c_2	5.85778×10^{-3}	1.51361×10^{-2}
c_3	7.68222×10^{-3}	7.51886×10^{-2}
c_4	0.0	4.60643×10^{-3}
c_5	-2.96400×10^{-6}	1.35000×10^{-2}
c_6	0.0	-1.06750×10^{-4}
c_7	0.0	1.36600×10^{-5}
T range (keV)	0.2–100	0.2–100

where the temperature is in keV and $k_{\rm AB}$ is 7.525×10^{-25}cm^{3}s^{-1} for the D-D reaction and 1.085×10^{-22}cm^{3}s^{-1} for the D-T reaction. This formula is accurate to about 20% in the temperature range from 1.4 to 8.5 keV for the D-D reaction, and from 1.2 to 5.5 keV for the D-T reaction. Therefore, it has often been used for analytical calculations. However, it should be noted that κ is temperature dependent as $\kappa = \eta T^{-1/3} - \frac{2}{3}$ with $\eta = 6.27$ for the D-D reaction and 6.66 for the D-T reaction. Bosch and Hale have given the following suitable and rather accurate parameterized forms for the thermal reactivities:

$$\langle \sigma v \rangle = \frac{c_1 \theta \xi}{\mu_{\rm red} c^2 T^3} \exp(-3\xi), \tag{11}$$

$$\theta = T \left(1 - \frac{T(c_2 + T(c_4 + Tc_6))}{1 + T(c_3 + T(c_5 + Tc_7))} \right)^{-1},$$

$$\xi = \left(\frac{B_G^2}{4\theta} \right)^{1/3}.$$

Here, the reactivity is again in cm^{3}s^{-1} and the parameters resulting from this fit are shown in table 2 for the temperature range from 0.2–100 keV.

2.1.4. Neutron energy spectra

The starting point for calculating fusion neutron energy spectra is the kinematics of the binary neutron producing reactions (2-3a). Using classical kinematics the energy of the

fusion neutron from the reaction A(B,n)a can in the laboratory frame be written (see e.g. Brysk 1973) as

$$E_{\mathrm{n}} = \tfrac{1}{2} m_{\mathrm{n}} v_{\mathrm{n}}^2 = \tfrac{1}{2} m_{\mathrm{n}} V^2 + \frac{m_a}{m_a + m_{\mathrm{n}}} (Q + K) + \cos\varphi\, V \sqrt{\frac{2 m_{\mathrm{n}} m_a}{m_{\mathrm{n}} + m_a} (Q + K)} \tag{12}$$

where m_{n} is the neutron mass, v_{n} is its velocity in the laboratory frame, V is the centre-of-mass velocity of the colliding particles, m_a is the mass of the second reaction product, φ is the angle between the centre-of-mass velocity and the neutron velocity in the centre-of-mass frame and K is the relative energy given by:

$$K = \frac{1}{2} \frac{m_{\mathrm{A}} m_{\mathrm{B}}}{m_{\mathrm{A}} + m_{\mathrm{B}}} (\boldsymbol{v}_{\mathrm{A}} - \boldsymbol{v}_{\mathrm{B}})^2$$

where $m_{\mathrm{A}}, m_{\mathrm{B}}$ and $\boldsymbol{v}_{\mathrm{A}}$, $\boldsymbol{v}_{\mathrm{B}}$ are the masses and velocities of the reacting particles, respectively. The local neutron energy spectrum for a given direction of emission is:

$$\frac{\mathrm{d}^2 N}{\mathrm{d}\Omega_{\mathrm{lab}}\, \mathrm{d}E} = \frac{n_{\mathrm{A}} n_{\mathrm{B}}}{1 + \delta_{\mathrm{AB}}} \iint f_{\mathrm{A}}(\boldsymbol{v}_{\mathrm{A}}) f_{\mathrm{B}}(\boldsymbol{v}_{\mathrm{B}}) \frac{\mathrm{d}^2\sigma}{\mathrm{d}\Omega_{\mathrm{lab}} \mathrm{d}E} \delta(E - E_{\mathrm{n}})\, |\boldsymbol{v}_{\mathrm{A}} - \boldsymbol{v}_{\mathrm{B}}|\, \mathrm{d}\boldsymbol{v}_{\mathrm{A}} \mathrm{d}\boldsymbol{v}_{\mathrm{B}}. \tag{13}$$

The differential cross section, $\mathrm{d}\sigma/\mathrm{d}\Omega$, can be expanded in Legendre polynomials, P_n, as

$$\frac{\mathrm{d}\sigma}{\mathrm{d}\Omega} = \sigma_0 \left(A_0 + A_2 P_2(\cos\vartheta) + A_4 P_4(\cos\vartheta) + \cdots\right) \tag{14}$$

where ϑ is the emission angle in the centre-of-mass frame and σ_0 is the differential cross section for $\vartheta = 0$. The expansion coefficients are tabulated for energies above 10 keV in Drosg and Schwerer (1987). Agreement of the total cross section

$$\sigma_{\mathrm{tot}} = 2\pi\sigma_0 \int \left(A_0 + A_2 P_2(\cos\vartheta) + A_4 P_4(\cos\vartheta) + \cdots\right) \mathrm{d}(\cos\vartheta)$$

with the rather accurate total cross section given by Bosch and Hale (1992) is obtained by linearly interpolating and renormalizing the tabulated expansion coefficients. If the particle velocities $\boldsymbol{v}_{\mathrm{A}}$, $\boldsymbol{v}_{\mathrm{B}}$ and the emission direction are given, the neutron energy, E_{n}, is determined according to equation (12). For calculating the neutron energy spectra, equation (13) has to be evaluated for the given velocity distributions f_{A} and f_{B}.

The energy spectrum of neutrons produced in fusion plasmas provides information on the production mechanisms of the emitted neutrons and the energy distributions of the reacting ions. For thermonuclear plasmas various authors (e.g. Lehner and Pohl 1967, Brysk 1973, Heinrichs *et al* 1989) have shown analytically that the energy distribution of the emitted neutrons is approximately given by a Gaussian as

$$\frac{\mathrm{d}^2 N}{\mathrm{d}\Omega_{\mathrm{lab}}\, \mathrm{d}E} = \frac{1}{W\sqrt{\pi}} \exp\left(-\frac{(E - \langle E_{\mathrm{n}}\rangle)^2}{W^2}\right) \tag{15}$$

where $\langle E_{\mathrm{n}}\rangle$ denotes averaging of equation (12) over the angle φ and

$$W^2 = \frac{4 m_{\mathrm{n}} \langle E_{\mathrm{n}}\rangle T}{(m_{\mathrm{n}} + m_{\mathrm{a}})}.$$

Table 3. Calculated widths, ΔE_{DD}, of Maxwellian D-D neutron spectra for various plasma temperatures T as given by Lehner and Pohl 1967 (Analytic), van Belle and Sadler 1986 (FSPEC), Scheffel 1984 (NSPEC), Wolle *et al* 1995 (NSOURCE), and Ballabio *et al* 1997 (BALLABIO), respectively.

T	ΔE_{DD} (keV)				
(keV)	Analytic	FSPEC	NSPEC	NSOURCE	BALLABIO
2	116.7	115.3	117.1	116.7	116.8
4	165.0	163.6	166.1	163.5	165.2
10	260.9	261.4	264.6	261.9	261.3
20	369.0	376.0	378.1	371.2	370.0

Thus, the width, $\Delta E = 2W\sqrt{\ln 2}$, of the spectra is a direct measure of the plasma temperature T. The analytical results are $\Delta E_{\mathrm{DD}}(keV) = 82.5\sqrt{T}$ and $\Delta E_{\mathrm{DT}}(keV) = 177\sqrt{T}$, respectively. Maxwellian neutron spectra serve as an important test case for the numerical spectra simulation. Therefore, detailed numerical analysis has also been carried out (Scheffel 1984, Slaughter 1986, van Belle and Sadler 1987, Wolle *et al* 1995, Ballabio *et al* 1997). Results for the Maxwellian neutron spectra are summarized in table 3 for various plasma temperatures. The different results agree well for temperatures of 10 keV and below. However, differences occur for the higher temperatures at 20 keV and above. In this temperature range the more recent numerical results are comparable and agree well with the analytic analysis while the previous numerical analyses deviate by about 2%.

2.2. Velocity distributions of ions in magnetically confined plasmas

The exact description of a magnetically confined plasma containing N particles with N equations of motion coupled through electro-magnetic fields is not practicable. The transition from the $6N$-dimensional phase space to the 6-dimensional phase space $(\boldsymbol{r}, \boldsymbol{v})$ is leading to the kinetic equations which describe the evolution for the distribution function $f_A(t, \boldsymbol{r}, \boldsymbol{v})$ for each particle species A in the presence of particle sinks L_A and sources S_A (see, e.g., Wu 1966):

$$\left(\frac{\partial}{\partial t} + \boldsymbol{v} \cdot \frac{\partial}{\partial \boldsymbol{r}} + \frac{\boldsymbol{F}_A}{m_A} \cdot \frac{\partial}{\partial \boldsymbol{v}}\right) f_A = C(f_A) + S_A - L_A. \tag{16}$$

Here, m_A is the mass of the species and $\boldsymbol{F}_A = eZ_A(\boldsymbol{E} + c^{-1}[\boldsymbol{v} \times \boldsymbol{B}])$ is the external force acting on them. The collision operator $C(f_A)$ represents the rate of change of $f_A(t, \boldsymbol{r}, \boldsymbol{v})$

due to the collisions between the plasma particles. For instance, if the collision operator is calculated on the basis of binary collisions, then equation (16) is called the Boltzmann equation. The kinetic equation (16) is called the Fokker-Planck equation if the collision term is calculated on the assumption that there are simultaneous random, small changes in the momentum of a particle due to its interaction with the other particles in the plasma. The Fokker-Planck equation is the appropriate equation for simulation and analysis of neutron signals from fusion experiments. Rosenbluth, MacDonald and Judd (1957) first derived an expression of the second-order Taylor expansion of the Fokker-Planck collision operator for Coulomb interaction. However, the Fokker-Planck equation in the general form given by Rosenbluth *et al* is extremely difficult to solve since it is an integro-differential equation in six phase space variables and time. The only practicable method for solving this equation directly would be by using discrete particle simulation methods (see e.g. Arter 1995). However, a discrete particle method for proper treatment of magnetically confined fusion plasmas would inevitably be extremely expensive in computer time. Therefore, the Fokker-Planck equation has to be simplified sufficiently in order to make numerical solution practicable.

Since for tokamaks the toroidal field is much stronger than the poloidal field and toroidal symmetry can be assumed, it is sufficient to discuss the particle dynamics only in two directions, i.e. parallel and perpendicular to the toroidal magnetic field. Thus, the velocity can be written as $\boldsymbol{v} = \boldsymbol{v}_{\parallel} + \boldsymbol{v}_{\perp}$, where $\boldsymbol{v}_{\perp}$ contains drift velocities and the gyro-velocity. In the direction parallel to the field the particle dynamics is influenced by the electric field component $E_{\parallel}$, while perpendicular to the field the particle dynamics is determined by the fast gyro-motion and the slower drift motions. The normal procedure for obtaining the distribution function of ions in magnetically confined plasmas is based on the existence of different characteristic time scales and spatial scales. Assuming that $\Omega \gg \omega_{\mathrm{b}} \gg \nu_{\mathrm{c}}$ where Ω is the gyro-frequency, ω_{b} is the bounce frequency and ν_{c} is the particle-particle interaction frequency (collision frequency), the distribution function f_A is expanded in powers of the small ratio of the relevant time scales. For practical purposes it is sufficient to know only one or two of the leading terms of this expansion. Next, averaging over the frequency recurrent motions has to be carried out, starting with the highest frequency (gyro-frequency), then proceed to lower frequencies. Furthermore, the macroscopic velocity may be approximated by

$$\boldsymbol{v} = \boldsymbol{v}_{\parallel} + \boldsymbol{v}_{\mathrm{drift}} = v_{\parallel}\boldsymbol{B}/|B| + \boldsymbol{v}_{\mathrm{curv}} + \boldsymbol{v}_{E\times B} + \boldsymbol{v}_{\nabla B} + \ldots$$

where $\boldsymbol{v}_{\mathrm{curv}}$, $\boldsymbol{v}_{E\times B}$ and $\boldsymbol{v}_{\nabla B}$ are the drift velocities due to curvature, magnetic field gradient, and $E \times B$ drift, respectively. With this, the guiding-centre kinetic equation can be writen as:

$$\left(\frac{\partial}{\partial t} + v_{\parallel}\frac{\boldsymbol{B}}{|B|}\cdot\frac{\partial}{\partial \boldsymbol{r}} + \boldsymbol{v}_{\mathrm{drift}}\cdot\frac{\partial}{\partial \boldsymbol{r}} + \frac{eZ_A}{m_A}E_{\parallel}\frac{\partial}{\partial v_{\parallel}}\right) f_A = C(f_A) + S_A - L_A. \tag{17}$$

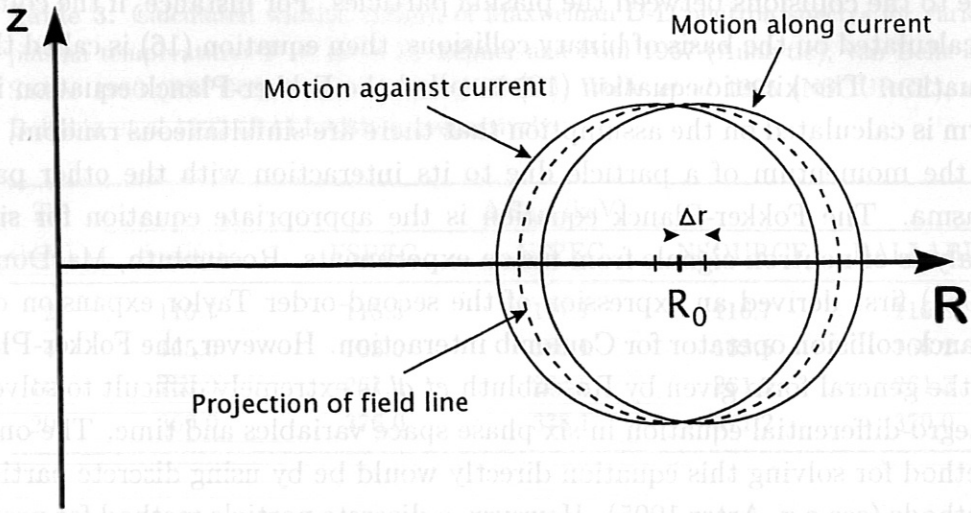

Figure 2. Projection of the drift trajectories of passing particles onto the (R, z) plane for circular magnetic surfaces.

However, in most situations even the calculation of this leading term meets difficulties due to the spatial gradients. For tokamak plasmas, e.g., it is therefore assumed that the radial excursion Δr of the ions from their magnetic flux surface is small as compared to the density and temperature scale lengths, L (figure 2). The lowest-order distribution can then again be expanded in powers of the small parameter $\Delta r/L$. For applications in tokamak plasmas usually only the leading zeroth-order term is considered. (However, it should be noted that this expansion fails when treating high-energetic particles, such as fusion α-particles or tritons born in fusion experiments.)

The Fokker-Planck equation for calculating the zero-order ion velocity distributions is valid for treating non-thermal plasmas, provided that appropriate terms for describing the physical origin of the non-thermal distributions are being included. As an important limiting case, the solutions for the velocity distributions of a plasma in thermodynamic equilibrium without external forces, sinks or sources are simply Maxwellians. In case of the auxiliary heating methods being applied on present-day fusion experiments, the velocity distributions of the plasma particles consist of a thermal background population (corresponding to the solution without sinks and sources), and a smaller fast non-thermal population. Therefore, collisions between fast ions (self-collisions) occur infrequently as compared to collisions between fast ions and thermal ions and it is sufficient to use isotropic Maxwellian distributions in the collision operator.
In the following two subsections two special cases of the kinetic equation for tokamak

plasmas are considered which are important for numerical simulation. The first one is the linearized guiding-centre equation for a plasma in uniform magnetic fields where spatial gradients can be neglected. This kinetic equation describes the so-called 'passing' particles and is an important limiting case of the second kinetic equation. The latter includes next-order effects due to the non-uniform tokamak magnetic fields and, thus, takes into account effects of so-called 'trapped' particles.
Finally, the last section summarises additional terms used in kinetic equations, i.e. particle source and loss terms, and operators for wave-particle interactions.

2.2.1. Kinetic equation for plasmas in uniform magnetic fields

By choosing a spherical coordinate system (v, θ, ϕ) for velocity space with $\theta = 0$ corresponding to the direction along a magnetic field line, the distribution of particles will depend on the variables $v = |\boldsymbol{v}|$ and $\mu = \cos\theta$ and the collision operator becomes two-dimensional. It should also be noted that due to the uniform magnetic field, the Lorentz force in the term $m_A^{-1}\boldsymbol{F}_A\nabla_v f_A$ in the kinetic equation vanishes. If the electric field can also be neglected, the complete term $m_A^{-1}\boldsymbol{F}_A\nabla_v f_A$ vanishes. Furthermore, it is assumed that the Larmor radius is small as compared to the plasma radius or the density scale length. Thus, to lowest order radial gradients can be neglected. Neglecting self-collisions, the kinetic equation can be linearized. It has been shown (e.g. Goldston *et al* 1981; Wolle *et al* 1991), that the errors due to linearization of the collision coefficients are small – typically in the order of 1-2%. Thus, the collision operator simplifies further and the kinetic equation can be written as

$$\frac{\partial f_A}{\partial t} = \frac{1}{v^2}\frac{\partial}{\partial v}\left[-\alpha v^2 f_A + \frac{1}{2}\frac{\partial}{\partial v}\left(\beta v^2 f_A\right)\right] + \frac{\gamma}{4v^2}\frac{\partial}{\partial \mu}\left[\left(1-\mu^2\right)\frac{\partial f_A}{\partial \mu}\right] + S_A - L_A \tag{18}$$

where the collision coefficients are given by (see for instance Stix, 1975):

$$\alpha = \langle \Delta v_\parallel \rangle + \frac{1}{2v}\langle (\Delta v_\perp)^2 \rangle, \quad \beta = \langle (\Delta v_\parallel)^2 \rangle, \quad \gamma = \langle (\Delta v_\perp)^2 \rangle. \tag{19}$$

The diffusion coefficients are given by:

$$\langle \Delta v_\parallel \rangle = \frac{C_b}{2n_b}\frac{\partial h}{\partial v}, \quad \langle (\Delta v_\parallel)^2 \rangle = \frac{C_b}{2n_b}\frac{\partial^2 g}{\partial v^2}, \quad \langle (\Delta v_\perp)^2 \rangle = \frac{C_b}{n_b v}\frac{\partial g}{\partial v}. \tag{20}$$

Here, b denotes background field particles, ions (i) and electrons (e). Furthermore, $g(v)$ and $h(v)$ are the Rosenbluth potentials for isotropic background velocity distributions $f_b(v)$ given by

$$g(v) = \frac{n_b}{l_b\sqrt{\pi}}\int_0^\infty \frac{v_b^2}{v}\left[f_b(v - v_b) - f_b(v + v_b)\right] dv_b \tag{21}$$

$$h(v) = \frac{1}{2}\left(1 + \frac{m_a}{m_b}\right)\frac{1}{v}\frac{\partial^2}{\partial v^2}\left[vg(v)\right] \tag{22}$$

and

$$C_b = 8\pi n_b Z_A^2 Z_b^2 e^4 \frac{\ln\Lambda_{Ab}}{m_A^2} \tag{23}$$

where $\ln\Lambda_{Ab}$ is the Coulomb logarithm. For Maxwellian background velocity distributions in the Rosenbluth potentials the diffusion coefficients are simply:

$$\begin{aligned}
\langle \Delta v_\parallel \rangle &= -\sum_b C_b l_b^2 \left(1 + \frac{m_a}{m_b}\right) G(l_b v) \\
\langle (\Delta v_\parallel)^2 \rangle &= \sum_b \frac{C_b}{v} G(l_b v) \\
\langle (\Delta v_\perp)^2 \rangle &= \sum_b \frac{C_b}{v} G(l_b v)\left[\Phi(l_b v) - G(l_b v)\right].
\end{aligned} \tag{24}$$

Here, Φ is the error function, $G = (\Phi - x\Phi')/2x^2$ is the Chandrasekhar function and $l_b^2 = m_A/2kT_b$.

For the ion and electron Coulomb logarithms, $\ln\Lambda_{Ai}$ and $\ln\Lambda_{Ae}$, that appear in the collision coefficients expressions for a multispecies plasma allowing for different temperatures for the different plasma particle species should be used. (The formalism for deriving appropriate expressions for the Coulomb logarithms has been outlined by Sivukhin 1966).

Equation (18) is separable in μ and v and the solution can be written in a series of the eigenfunctions of the pitch angle scattering operator which are simply Legendre polynomials in this case. This is particularly useful since the numerical evaluation of the fusion reactivity is significantly simplified if the distribution function is expanded in Legendre polynomials (see equation 9). Furthermore, in most cases, only the first few orders need to be calculated to obtain a reasonable accuracy. The computation time is therefore fairly short.

It should be noted that the Rosenbluth potentials, equations (21-22), and thus the linearized collision operator may be simplified by the use of the inequality $v_i < v \ll v_e$, where $v_{i,e}$ are the background ion and electron thermal velocities as outlined below:

(i) *The particle energies are much greater than the ion temperature:*
Firstly, this allows the terms $\Phi'(v/v_i) \sim \exp(-v^2/v_i^2)$ that appear in the Chandrasekhar function in the expressions of the diffusion coefficient for the ions to be ignored and in the remaining expression the error function can be approximated by $\Phi(v/v_i) \approx 2v/v_i\sqrt{\pi}$. However, these approximations prevent the non-Maxwellian velocity distributions from tending to the proper Maxwellian form at low velocities. The usual method of dealing with this is to follow the

fast ions until they slow down to $\approx 1.5 v_{\rm th}$ and then transfer them from the fast, non-Maxwellian distribution to a separately treated thermal velocity distribution. Secondly, this assumption allows the diffusion in energy to be ignored, and thereby the collision operator no longer contains second-order derivatives in velocity.

(ii) *The particle velocities are much smaller than the thermal velocity of the electrons:* This allows the ion velocity distribution to be treated as a δ-function when calculating the electron collision terms. For current plasma experiments with injection of energetic particles this assumption is well justified. However, it is insufficient for treating e.g. ICRF heated plasmas with particles being accelerated into the MeV region.

The resulting expression for the linearized, approximated collision operator is (Cordey and Houghton, 1973):

$$C(f_A) = \frac{1}{\tau_{\rm s}} \frac{1}{v^2} \frac{\partial}{\partial v} \left[(v^3 + v_\alpha^3) f_A \right] + \frac{1}{\tau_{\rm s}} \frac{v_\gamma^3}{4v^3} \frac{\partial}{\partial \mu} \left[(1-\mu^2) \frac{\partial f_A}{\partial \mu} \right] \tag{25}$$

where the slowing-down time of ions on electrons, $\tau_{\rm s}$, is

$$\tau_{\rm s} = \frac{3}{2} \sqrt{\pi} \frac{m_{\rm e}}{m_A C_{\rm e}} \left(\frac{2kT_{\rm e}}{m_{\rm e}} \right)^{3/2} . \tag{26}$$

The characteristic velocities v_α and v_γ are defined by

$$v_\alpha^3 = \frac{3}{4} \sqrt{\pi} \left(\frac{2kT_{\rm e}}{m_{\rm e}} \right)^{3/2} \sum_i \frac{n_i}{n_{\rm e}} Z_i^2 \frac{m_{\rm e}}{m_i} \tag{27}$$

$$v_\gamma^3 = \frac{3}{2} \sqrt{\pi} \frac{m_{\rm e}}{m_A} \left(\frac{2kT_{\rm e}}{m_{\rm e}} \right)^{3/2} \sum_i \frac{n_i}{n_{\rm e}} Z_i^2 \tag{28}$$

and denote the velocities below which collisions on ions are more important for slowing-down and pitch angle scattering, respectively, than collisions on electrons. The above given approximation (25) is frequently used for numerical or analytical calculations for NBI- or ICRF heated plasmas (see, e.g. Goldston *et al* 1981, Pekkari *et al* 1983, Core 1993, Wolle 1997a).

As an illustrative example for the time evolution of an ion velocity distribution in an uniform magnetic field, the numerical solution of the Fokker-Planck equation with the linearized collision operator (18) is plotted in figure 3 for a plasma with $T_{\rm e} = T_{\rm i} = 5$ keV, $n_{\rm e} = n_{\rm i} = 2 \times 10^{13}$ cm^{-3} and an ion source with a source rate of 2×10^{13} cm^{-3}s^{-1}. In order to keep the ion density constant in time the source term has been balanced by a thermal loss term (i.e. $\int L v^2 {\rm d}v = \int S v^2 {\rm d}v$). The initial fast ion energy was $E_0 = 80$ keV. In this example, the slowing-down time for the ions on electrons is $\tau_{\rm s} \approx 1.27$ s. The critical energy E_α, below which collisions on ions are more important for the slowing-down than collisions on electrons follows from equation (27) and is about 103 keV for

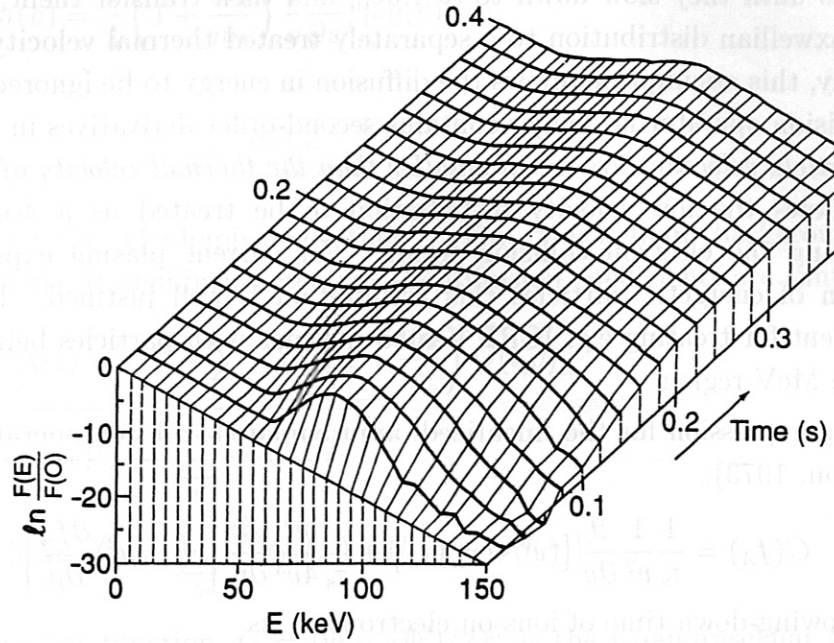

Figure 3. Evolution of the ion velocity distribution in time for a test case plasma with $T_e = T_i = 5$ keV, $n_e = n_i = 2 \times 10^{13}$ cm^{-3}, an ion source with a source rate of 2×10^{13} cm^{-3}s^{-1}. Source term and loss term have been balanced and the initial fast ion energy was $E_0 = 80$ keV (after Wolle *et al* 1994).

the plasma data given above. The time t_{st} it takes to establish the velocity distribution below the injection velocity, i.e. the time it takes for a particle to slow down from the injection velocity to the thermal region, can be estimated from the time-dependent Fokker-Planck equation. Using the high energy approximation (25) and integrating over the pitch angle μ, one obtains

$$t_{st} = \frac{\tau_s}{3} \ln \left(1 + \left(\frac{E_0}{E_\alpha} \right)^{3/2} \right) . \tag{29}$$

With the values given above, $t_{st} \approx 0.22$ s which agrees well with the numerical solution.

2.2.2. Kinetic equation for plasmas in non-uniform magnetic fields

It is generally the case in magnetic fusion devices that the magnetic field is non-uniform. On the scale of the gyro-motion, which is the fastest recurrent motion of charged particles in a magnetically confined plasma, the magnetic field varies only weakly. However, as

shown schematically in figure 4, during its motion along the direction of the field the charged particle is being carried through finite variations of the magnetic field. These field variations can affect the properties of the plasma. Therefore, it may often be necessary to take the non-uniformity into account in the kinetic equations in order to describe the velocity distributions with sufficient accuracy.

An example of a feature caused by the non-uniform tokamak field is the presence of trapped particles (cf. figure 5). Trapped particles affect e.g. the electrical conductivity (Hinton and Hazeltine 1976, Hinton and Oberman 1969), radial transport (Galeev and Sagdeev 1968), toroidal momentum transfer (Hinton and Robertson 1984, Hinton and Rosenbluth 1996) or the neutron production (Wolle *et al* 1997b).

For simulation of the basic plasma quantities such as densities, temperatures or fusion reactivities only the long-term behaviour of the distribution functions is of interest, i.e. rapid fluctuations on the fast time scales of the gyro- or bounce-periods are viewed as subordinate in this respect. The general procedure to simplify kinetic equations for non-uniform toroidal magnetic fields is to average first over the highest frequency nearly recurrent motion and proceed to lower frequencies until the relevant collisional time scale is reached. The starting point to derive an appropriate bounce-averaged kinetic equation for ions is the guiding-centre kinetic equation (17) in a toroidal plasma, see

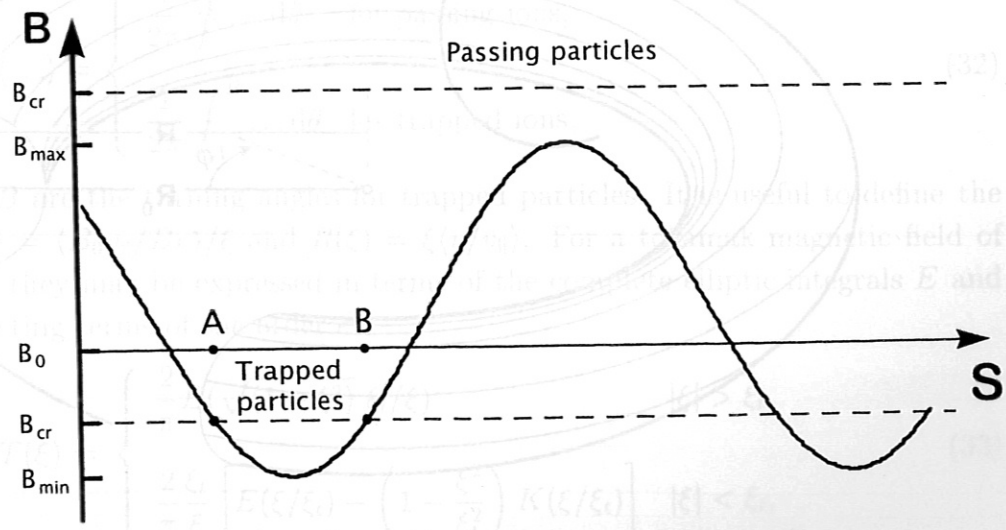

Figure 4. Schematic sketch of the magnetic field variation in a tokamak along a field line S and possible values of the critical field B_{cr} for passing and trapped particles. A and B refer to the turning points of the trapped particles.

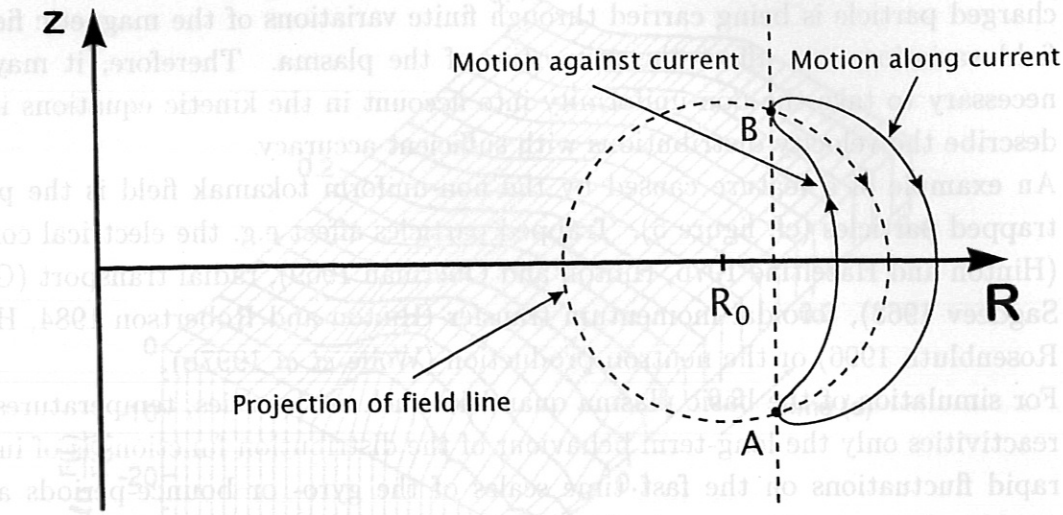

Figure 5. Projection of the trajectory of a trapped particle onto the (R, z) plane for circular magnetic surfaces. A and B denote the turning points of the orbit.

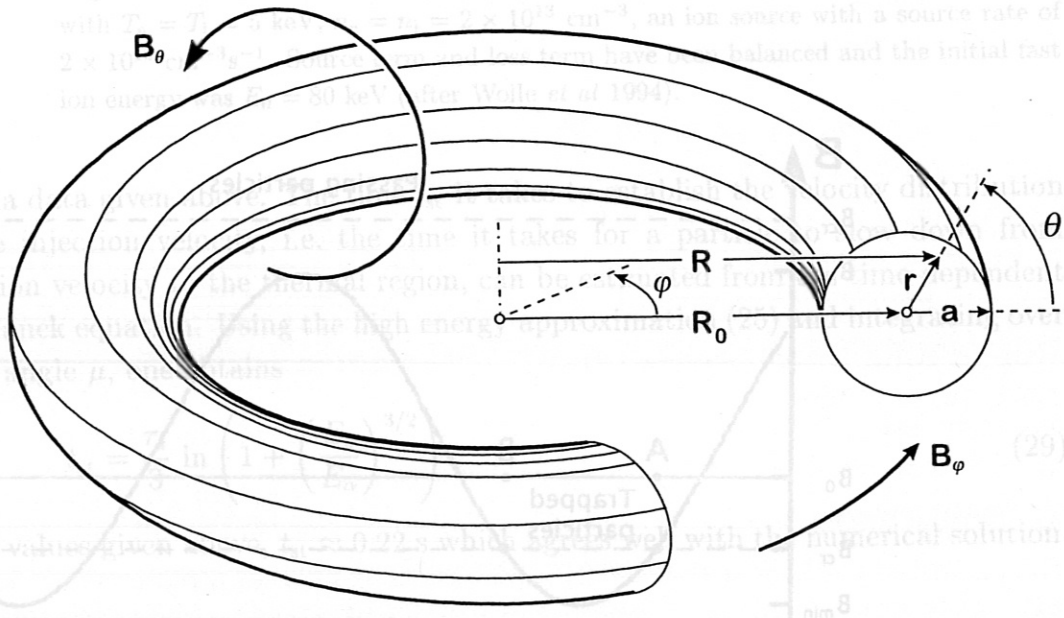

Figure 6. Topology of the toroidal configuration.

e.g. Stringer (1974) or Galeev and Sagdeev (1968). With the realistic, but sufficiently simple assumption of a circular axisymmetric torus in which the longitudinal field is

much stronger than the azimuthal field B_θ, such as e.g. in systems like the tokamak, the magnetic field strength B on a magnetic surface can be represented as ($\epsilon \ll 1$)

$$B = \frac{B_0(1 - \epsilon\cos\theta)}{1 - \epsilon} \tag{30}$$

where θ is the azimuthal angle on the magnetic surface, $\epsilon = r/R_0$ is the inverse aspect ratio, R_0 is the large radius of the tokamak and r is its small one (see figure 6). It should be mentioned that under the conditions of $B_\theta \ll B_0$ and $\epsilon \ll 1$ the magnetic field along a line of force is simply corrugated. Since the quantity ϵ is assumed to be small, the kinetic equation can be expanded in terms of ϵ. Keeping only the low-order terms and expanding the distribution function as a series in τ_b/τ_s where τ_b is the bounce period of the fast ions the resulting first-order bounce-averaged kinetic equation was first derived by Connor and Cordey (1974). On tokamaks effects of an externally applied electric field can normally be neglected and the bounce-averaged kinetic equation with Fokker-Planck collision operator is given by:

$$\frac{\partial f_A}{\partial t} = \frac{1}{v^2}\frac{\partial}{\partial v}\left[-\alpha v^2 f_A + \frac{1}{2}\frac{\partial}{\partial v}\left(\beta v^2 f_A\right)\right] + \frac{\gamma}{4v^2}\frac{1}{\langle v/v_\parallel\rangle \xi}\frac{\partial}{\partial \xi}\left[\left(1-\xi^2\right)\frac{\langle B_0 v_\parallel/Bv\rangle}{\xi}\frac{\partial f_A}{\partial \xi}\right]$$
$$+ \left\langle \frac{v}{v_\parallel}\right\rangle^{-1}\left\langle \frac{v}{v_\parallel} S_A\right\rangle - \left\langle \frac{v}{v_\parallel}\right\rangle^{-1}\left\langle \frac{v}{v_\parallel} L_A\right\rangle. \tag{31}$$

Here, ξ is the pitch angle given by $\xi^2 = 1 - (1-\mu^2)B_0/B$. The usual bounce-integrals over the poloidal angle θ are

$$\langle \ldots \rangle = \begin{cases} \dfrac{1}{2\pi}\oint \ldots \mathrm{d}\theta & \text{for passing ions,} \\ \dfrac{1}{2\pi}\displaystyle\int_A^B \ldots \mathrm{d}\theta & \text{for trapped ions,} \end{cases} \tag{32}$$

where A and B are the turning angles for trapped particles. It is useful to define the functions $T(\xi) = \langle B_0 v_\parallel/Bv\rangle/\xi$ and $R(\xi) = \xi\langle v/v_\parallel\rangle$. For a tokamak magnetic field of the form (30), they may be expressed in terms of the complete elliptic integrals E and K when neglecting terms of the order ϵ^2:

$$T(\xi) = \begin{cases} \dfrac{2}{\pi}E\left(\sqrt{(1-\xi^2)}\,\xi_t/\xi\right) & |\xi| > \xi_t, \\ \dfrac{2}{\pi}\dfrac{\xi_t}{\xi}\left[E(\xi/\xi_t) - \left(1 - \dfrac{\xi^2}{\xi_t^2}\right)K(\xi/\xi_t)\right] & |\xi| < \xi_t, \end{cases} \tag{33}$$

$$R(\xi) = \begin{cases} \dfrac{2}{\pi}K\left(\sqrt{(1-\xi^2)}\,\xi_t/\xi\right) & |\xi| > \xi_t, \\ \dfrac{2}{\pi}\dfrac{\xi}{\xi_t}K(\xi/\xi_t) & |\xi| < \xi_t, \end{cases} \tag{34}$$

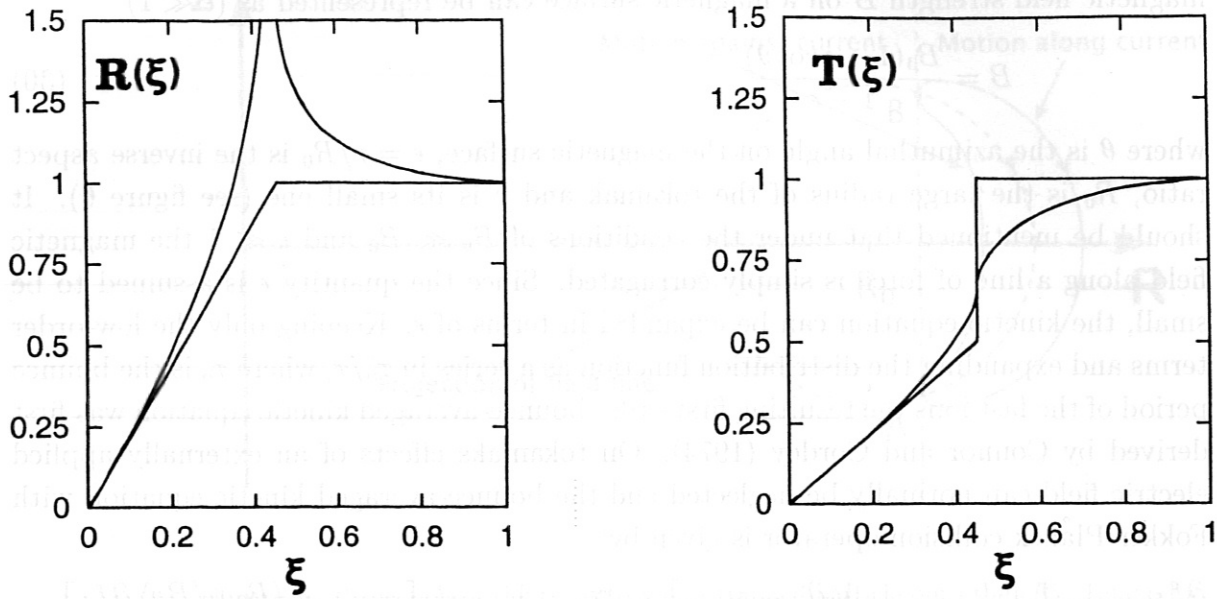

Figure 7. The functions R and T together with their asymptotic approximations for $\xi \to 0$ and $\xi \to 1$.

where $\xi_t = \sqrt{2\epsilon}$ is the pitch angle for the trapping boundary. (It should be noted that in the limit of $\xi_t \to 0$ equation (31) becomes the kinetic equation for uniform magnetic fields, equation (18)). Equation (31) is separable in ξ and v and the solution can be written in a series of eigenfunctions as $f_a = \sum a_n(v,t)\, C_n(\xi)$ where the C_n are the eigenfunctions of the equation

$$\frac{1}{R}\frac{\mathrm{d}}{\mathrm{d}\xi}\left[\left(1-\xi^2\right)\frac{T\,\mathrm{d}C_n}{\mathrm{d}\xi}\right] + \lambda_n C_n = 0 \tag{35}$$

with eigenvalue $\lambda_n = \nu_n(\nu_n+1)$ and the boundary conditions:

$$\left.\frac{T\,\partial C_n}{\partial \xi}\right|_{\xi>\xi_t} - \left.\frac{T\,\partial C_n}{\partial \xi}\right|_{-\xi<-\xi_t} = \left.\frac{2T\,\partial C_n}{\partial \xi}\right|_{\xi<\xi_t}, \tag{36}$$

$$C_n(-\xi) = C_n(\xi) \quad \text{for} \quad |\xi| < \xi_t. \tag{37}$$

Furthermore, the C_n have to be finite at $\xi = \pm 1, 0$. It has been shown by Cordey (1976) that the functions R and T can be approximated in the trapped and passing regions by their limiting values near $\xi = 0$ and $\xi = 1$, viz., $R = 2T = \xi/\xi_t$ and $R = T = 1$. Figure 7 shows the functions R and T together with their approximations. In the vicinity of the transition point between trapped and passing particles bounce-averaging fails since the

bounce-time goes to infinity as $\xi \to \xi_t$. This leads to a logarithmic singularity in $\langle v/v_\parallel \rangle$ and a singularity in the derivative of $\langle B_0 v_\parallel / Bv \rangle$. The width of the transition region is very small and orbits in this region will be scattered out on the pitch angle scattering time scale. Thus, it is justified to use the approximations which do not contain this singularity.

For small ξ_t and assuming that $\nu_n = n + \alpha_n$ with $\alpha_n \ll 1$, approximate analytic solutions for the eigenvalues and eigenfunctions are available (Cordey 1976). However, it was shown by Wolle *et al* (1997b) that these approximations are only appropriate for very small values of ϵ. For realistic values of ϵ the analytic expressions for the eigenvalues are no longer valid and with the approximate eigenfunctions the boundary condition (36) is not being satisfied. The equation (35) for the eigenfunctions has, thus, to be solved numerically. When solving equation (35) numerically, the eigenvalue and the eigenfunction have to be determined simultaneously by a shooting-method. As an example, the calculated first four eigenfunctions for $\epsilon = 0.1$ are plotted in figure 8.

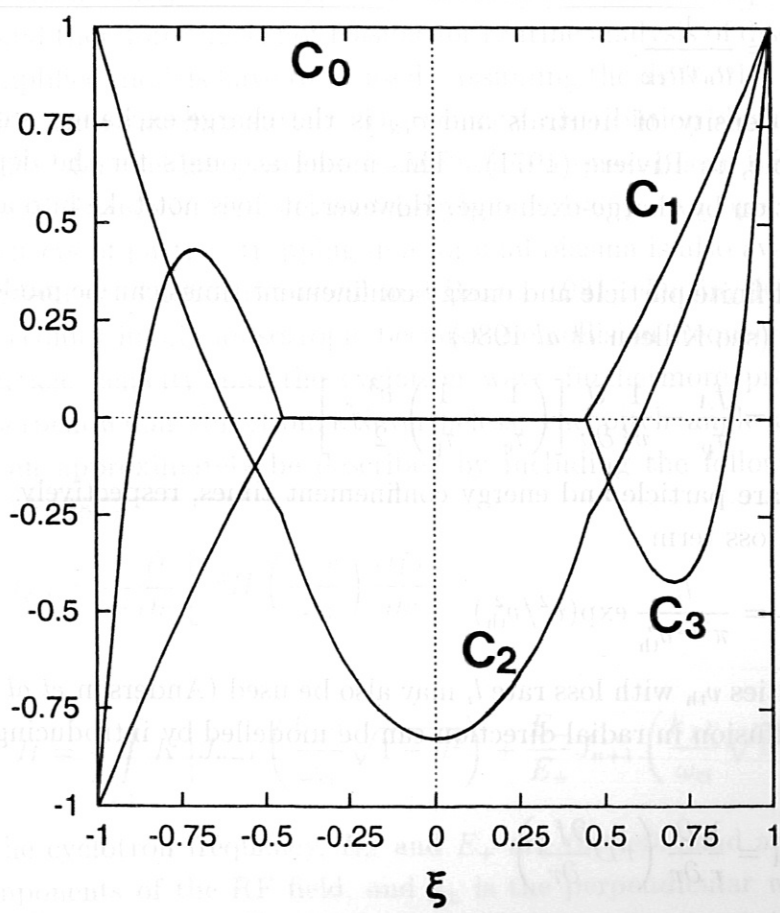

Figure 8. Calculated eigenfunctions $C_0(\xi), \ldots, C_3(\xi)$ for the case $\epsilon = 0.1$.

2.2.3. Additional terms entering the kinetic equation

The particle source term S_A in the kinetic equation is of the form

$$S_A(v,\theta,t) = \sum s_i A_i(v,v_i) K_i(\cos\theta,\cos\theta_i) \tag{38}$$

where s_i, v_i and θ_i denote the source rate, initial velocity and initial angular direction of the ith particle source, respectively. Furthermore, the functions K_i and A_i describe the initial angular and velocity spread. Usually, the function A_i is assumed to be either monoenergetic (i.e. $A_i = \delta(v - v_i)/2\pi v_i^2$) or a narrow Gaussian with width $a_i v_{\rm th}$ (i.e. $A_i = \pi^{-3/2} a_i^{-3} v_{\rm th}^{-3} \exp(-v^2/a_i^2 v_{\rm th}^2)$).

Different models or a combination of several loss models may be used for the loss term. Losses due to charge-exchange are expressed as (see e.g. Cordey *et al* 1975, Goldston *et al* 1981, Scheffel 1985):

$$L_A = \frac{f_A}{\tau_{\rm cx}}, \tag{39}$$

where the charge-exchange time is given by

$$\tau_{\rm cx} = \frac{1}{n_{\rm n} v \sigma_{\rm cx}}. \tag{40}$$

Here, $n_{\rm n}$ is the density of neutrals and $\sigma_{\rm cx}$ is the charge-exchange cross section as given, for example, in Riviere (1971). This model accounts for the depletion of the velocity distribution by charge-exchange. However, it does not take into account effects of reionization.

The effects of finite particle and energy confinement times can be modelled by a loss term of the form (see Killeen *et al* 1986)

$$L_A = \frac{f_A}{\tau_{\rm p}} - \frac{1}{v^2}\frac{\partial}{\partial v}\left[\left(\frac{1}{\tau_{\rm e}} - \frac{1}{\tau_{\rm p}}\right)\frac{v^3}{2} f_A\right], \tag{41}$$

where $\tau_{\rm p}$ and $\tau_{\rm e}$ are particle and energy confinement times, respectively. Sometimes, a simple Gaussian loss term

$$L_A = \frac{l_i}{\pi^{3/2} v_{\rm th}^3} \exp(v^2/v_{\rm th}^2) \tag{42}$$

at thermal velocities $v_{\rm th}$ with loss rate l_i may also be used (Anderson *et al* 1988). Losses due to spatial diffusion in radial direction can be modelled by introducing the diffusion operator

$$D_A = \frac{1}{r}\frac{\partial}{\partial r}\left(r D \frac{\partial f_A}{\partial r}\right) \tag{43}$$

into the kinetic equation. Here, D is the diffusion coefficient and r is the distance from the magnetic axis in circular geometry. For diffusion coefficients such that $\partial D/\partial r = 0$,

the kinetic equation is separable and the eigenfunctions of the diffusion operator are Bessel functions of zeroth order, J_0. It should be noted that for radially independent diffusion coefficients, one obtains a characteristic particle confinement time as

$$\tau_D = \frac{a^2}{5.7831\, D} \tag{44}$$

where a is the minor plasma radius. Thus, introducing radially independent diffusion into the Fokker-Planck equation is equivalent to using a loss model with a velocity independent particle confinement time τ_p (first term in equation (41)). However, when assuming that $\partial D/\partial r = 0$, the velocity distributions along the radial coordinate differ somewhat from those obtained when using the f/τ_p loss model (Yamagiwa 1992).

The modelling of the effects of ICRF heating in a plasma is difficult. It can be broken down into three main objectives: coupling of the wave into the plasma, propagation and absorption of the wave in the plasma, and the evolution of the velocity distribution of the resonating species. As the three parts depend on each other, they should be calculated self-consistently. However, such combined calculations require large amounts of CPU time and therefore this is not feasible for routine analysis of discharges. Instead, sufficiently simplified models have to be used. Assuming the drift orbit of the resonating ions to coincide with the flux surface, the velocity distribution during ICRF heating can be calculated for passing particles by including a quasi-linear RF operator in the kinetic equation (Stix 1975, Kennel and Engelmann 1966). An operator which takes into account effects of particle trapping in a toroidal plasma is also available (Anderson *et al* 1985, Killeen *et al* 1986, Bernstein and Baxter 1981). During ICRH, the velocity distribution becomes highly anisotropic because the collision frequency decreases with increasing particle velocity and the cyclotron wave furthermore preferentially heats the ions in perpendicular direction. Nevertheless, the pitch angle averaged velocity distribution can approximately be described by including the following RF operator (Anderson *et al* 1987):

$$Q_A = \frac{1}{v^2}\frac{\partial}{\partial v}\left[v^2 H\left(\frac{k_\perp v}{\omega_\mathrm{ci}}\right)\frac{\partial f_A}{\partial v}\right] \tag{45}$$

where

$$H = \frac{1}{2}\int_{-1}^{1} K\left|J_{n-1}\left(\frac{k_\perp v}{\omega_\mathrm{ci}}\sqrt{1-\mu^2}\right) + \frac{E_-}{E_+}J_{n+1}\left(\frac{k_\perp v}{\omega_\mathrm{ci}}\sqrt{1-\mu^2}\right)\right|^2 \mathrm{d}\mu. \tag{46}$$

Here, ω_ci is the cyclotron frequency, E_- and E_+ are the left-hand and the right-hand polarized components of the RF field, and $k_\perp$ is the perpendicular wavenumber. The constant K relates the RF diffusion coefficient to the amplitude of the electric field at the resonance layer.

3. Simulation of D-D neutron emission

As already mentioned in section 2.2, in the case of neutral-beam-heated plasmas, the distribution $f_{\rm D}(\boldsymbol{v})$ can be split into a thermal part and a non-thermal (so-called 'beam') part $f_{\rm b}(\boldsymbol{v})$. There are different schemes for splitting the particle distribution. In many codes a scheme is used where usually all slowing-down particles above $1.5v_{\rm th}$ are classified as 'beam' and those below are classified as 'thermal' (see e.g. Goldston *et al* 1981). However, the most natural way of splitting the velocity distribution is by defining an isotropic Maxwellian $f_{\rm th}(\boldsymbol{v})$ which coincides with the distribution $f_{\rm D}(\boldsymbol{v})$ as $v \to 0$:

$$f_{\rm D}(\boldsymbol{v}) = f_{\rm th}(\boldsymbol{v}) + f_{\rm b}(\boldsymbol{v}). \tag{47}$$

The corresponding densities are $n_{\rm D}$, $n_{\rm th}$ and $n_{\rm b}$. The fusion reactivity may thus be written as the sum of three different reactivities:

$$\langle\sigma v\rangle_{\rm DD} = \langle\sigma v\rangle_{\rm th} + \langle\sigma v\rangle_{\rm bt} + \langle\sigma v\rangle_{\rm bb}. \tag{48}$$

The first term describes the reactivity of the thermal part of the plasma, the second one describes the reactivity between the fast particles and the thermal plasma and the last one the reactivity of the fast particles among themselves. This leads to the decomposition of the neutron rate $Q_{\rm n}$ into three different neutron rates, viz., $Q_{\rm th}$ (thermal), $Q_{\rm bt}$ (beam-thermal) and $Q_{\rm bb}$ (beam-beam).

The neutron rate emitted from the whole fusion plasma, which in literature is often referred to as neutron source strength, is simply

$$S_{\rm n} = \int Q_{\rm n}{\rm d}V \tag{49}$$

where V is the plasma volume. Furthermore, the neutron yield Y_n is just the time-integrated neutron source strength

$$Y_{\rm n} = \int S_{\rm n}{\rm d}t. \tag{50}$$

Finally, it should be mentioned here that for parameter studies it is often convenient to characterize the radial dependence of a given plasma parameter, i.e. its profile, by the so-called profile peakedness or peaking factor which is defined as

$$\widehat{Z} = \frac{Z(0)V}{\int Z(\rho){\rm d}V} = \frac{Z(0)}{\langle Z(\rho)\rangle}. \tag{51}$$

For the particular case of profiles of type $Z(\rho) = Z(0)(1-\rho^2)^\alpha$ where ρ labels the flux surface, the peaking factor is simply $\widehat{Z} = \alpha + 1 - \epsilon(\alpha)$, where $\epsilon(\alpha)$ is a small correction term. For circular plasmas, $\epsilon(\alpha) = 0$, and for example for the JET D-shaped plasma geometry $\epsilon(3)$ turns out to be 0.025. Thus, the peaking factor refers to parabolic shapes of type $(1-\rho^2)^\alpha$ and should not be used for profiles that strongly deviate from this

shape, such as e.g. hollow profiles.

In the remainder of this chapter different aspects relevant for the simulation of the neutron source strength in tokamaks are discussed. Firstly, some more general remarks about the neutron production mechanisms in neutral-beam-heated tokamak plasmas are given, which are based on the simplified kinetic equations discussed in subsection 2.2.1. Then, the necessary physics input (e.g. plasma geometry, measured plasma data, and Fokker-Planck models) for obtaining realistic simulation results are described. Many of the measured input data have to be obtained from other independent diagnostics. As a direct link with the experimental practice, known sources of systematic errors and their influence on the neutron source strength calculations are discussed. Other input data, e.g. the neutral beam deposition profiles, have to be calculated using the measured plasma data as well. Different computer codes for simulating the neutral-beam deposition are available. Therefore, a section is devoted to neutral-beam deposition codes and the underlying physical models. Next, different available computer codes for calculating the neutron source strength and neutron spectra are summarized. Finally, purely for completeness a brief description of the basic ideas and concepts of neutron transport simulation is given.

3.1. General remarks

The analytical pitch angle averaged steady-state solution of the kinetic equation with the approximate expression (25) of the collision operator is for the fast particles:

$$f_b(v) = \frac{p_{\mathrm{nbi}}}{4\pi E_{\mathrm{inj}}} \frac{\tau_{\mathrm{s}}}{v^3 + v_\alpha^3} \sigma(v_{\mathrm{inj}} - v) \tag{52}$$

where p_{nbi} is the power density and σ is the step function. On using this expression, the following approximate scaling laws for the neutron rates can be found (see e.g. Strachan *et al* 1993):

$$Q_{\mathrm{th}} \sim n_{\mathrm{th}}^2 T_{\mathrm{i}}^{\kappa}, \qquad \kappa \approx 6.27 T_{\mathrm{i}}^{-1/3} - \tfrac{2}{3} \tag{53}$$

$$Q_{\mathrm{bt}} \sim n_{\mathrm{th}} \tau_{\mathrm{s}} E_{\mathrm{inj}} \tag{54}$$

$$Q_{\mathrm{bb}} \sim P_{\mathrm{nbi}}^2 \tau_{\mathrm{s}}^2 E_{\mathrm{inj}}^{-2} \tag{55}$$

where E_{inj} is the injection energy, P_{nbi} is the neutral-beam power, n_{D} is the deuteron density, and $\tau_{\mathrm{s}} \sim T_{\mathrm{e}}^{3/2}/n_{\mathrm{e}}$ is the slowing-down time of ions on electrons.

As can be seen in the above equations, the thermal neutron rate is determined by the ion temperature and the thermal density, the beam-thermal neutron rate is determined by the injection and slowing-down properties, and the beam-beam neutron rate is solely dependent on the injection and slowing-down properties. These neutron rates

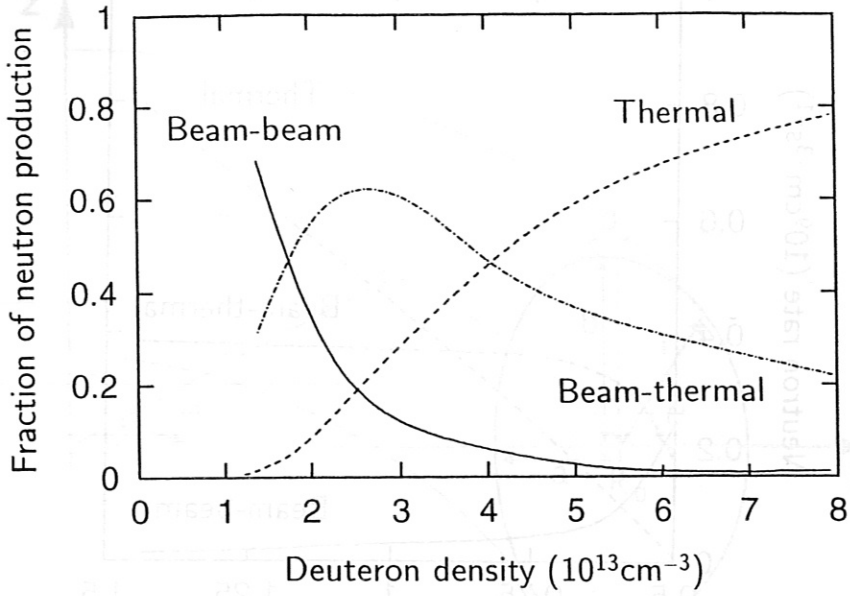

Figure 9. The fractions of the neutron production due to thermal, beam-thermal, and beam-beam reactions as a function of the deuteron density for a pure deuterium test case plasma with $T_\mathrm{i} = T_\mathrm{e} = 10$ keV, $E_\mathrm{inj} = 80$ keV and injection power density of $p_\mathrm{nbi} = 0.32$ Wcm^{-3}.

are, therefore, not independent from each other, but are related through the different plasma parameters. (For example, if the non-thermal density n_b is of the order of the total density, then the thermal density n_th is very small and therefore Q_th and Q_bt are small, and the neutron production is given by beam-beam reactions: $Q_\mathrm{n} \sim Q_\mathrm{bb}$.) In figure 9 the relative fractions of the neutron rates are plotted as a function of the density. In figure 10 the absolute values of the neutron rates are plotted as a function of the total neutron rate. With increasing density and keeping the injection power and the temperatures constant, Q_bb is decreasing, while Q_bt is reaching a constant level, and Q_th is increasing with n_D^2. Therefore, for a given operational regime of a tokamak and its neutral beams, there are mainly three approaches to achieve high neutron emission rates:

(i) In high density plasmas with good central confinement properties such as the pellet enhanced performance discharges (PEP) in JET (Smeulders *et al* 1995), the thermonuclear reactions between the Maxwellian background ions dominate or are of similar order as the beam-thermal fusion reactions. The contributions due to beam-beam reactions are small or negligible.

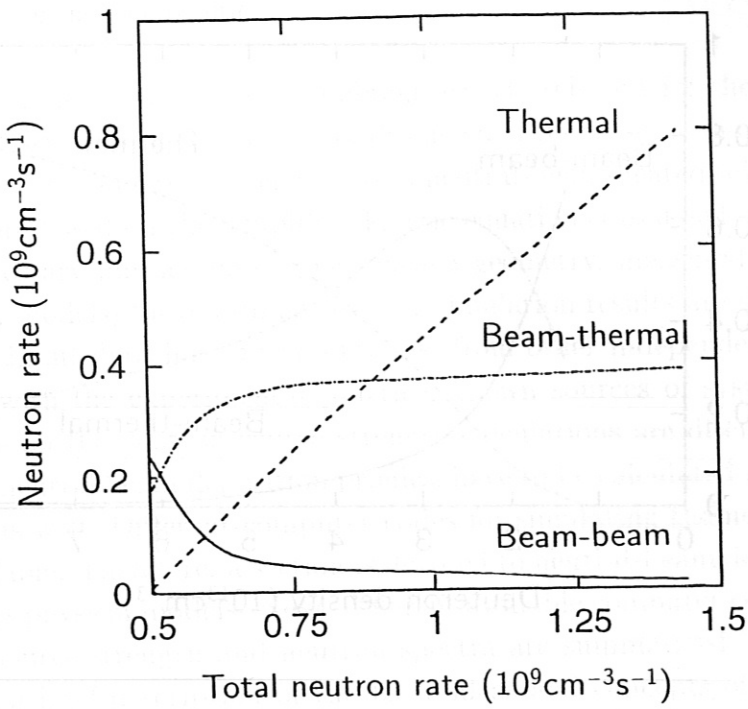

Figure 10. Absolute values of the different contributions to the neutron rate due to thermal, beam-thermal and beam-beam neutron production as shown in figure 9.

(ii) In plasmas with moderately high electron densities and moderately high temperatures the slowing-down time is relatively short and most of the fusion neutron production is due to beam-thermal reactions. This is often the case in the smaller tokamaks.

(iii) For low-density plasmas with reasonable confinement properties the slowing-down time is comparatively large and the non-thermal ion fraction can exceed 0.2, so that a considerable fraction or even the majority of the fusion reactions are due to beam-beam reactions. This is the case e.g. in JET hot-ion H-mode plasmas (Adams *et al* 1991) or the TFTR supershot regime (Strachan *et al* 1993).

3.2. Physics input

For accurate simulation calculations different input data are required. Firstly, the plasma and torus geometry have to be described by representations suitable for efficient numerical calculations. Secondly, a consistent and accurately measured set of different plasma parameters and their profiles is needed.

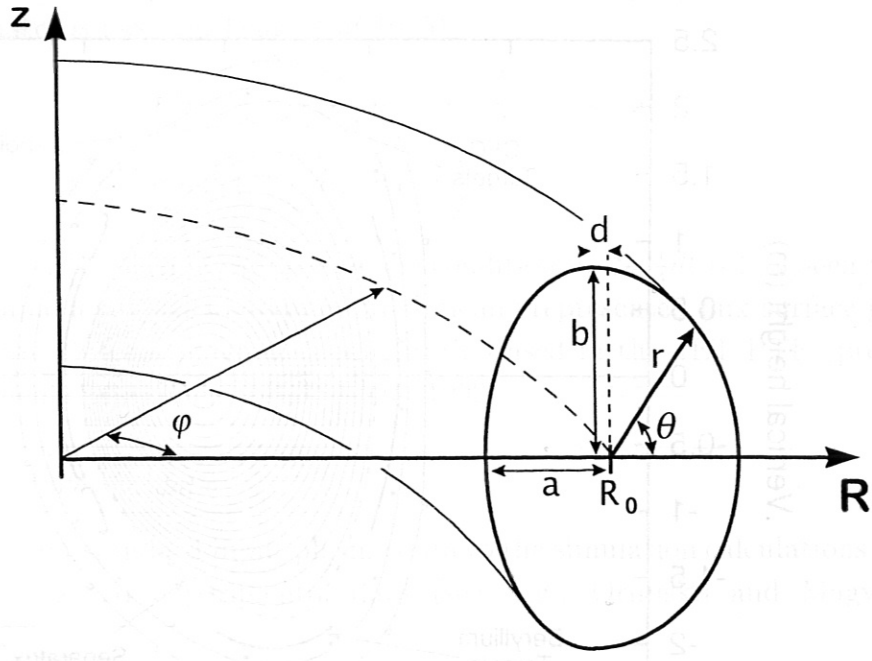

Figure 11. Parameters and coordinate system for a D-shaped plasma. R_0 is the major radius, a is the halfwidth, b is the halfheight, d is the metric triangularity, and $E = b/a$ is the elongation.

3.2.1. Plasma geometry

In tokamaks, equilibrium configurations exist where the constant poloidal magnetic flux $\psi(R, z)$ forms nested magnetic surfaces which define the natural spatial coordinates of these systems. Such a magnetic field topology is naturally produced in poloidal divertor configurations. Inside the x-point or separatrix the magnetic surfaces are closed. Beyond the separatrix the magnetic surfaces are open and the magnetic field lines are diverted to the walls. The minor radius of the plasma torus is then defined by the radius of the last closed flux surface. The major plasma radius corresponds to the distance of the centre of the last closed flux surface to the centre of the plasma torus. The most advanced tokamaks have non-circular cross sections. This non-circular cross sections can be further characterized by the following parameters: $\epsilon = a/R_0$, inverse aspect ratio; $E = b/a$, elongation; and d, metric triangularity, as shown in figure 11.

In many computer codes, the plasma and torus geometry of the tokamak are described by using a cylindrical coordinate system with respect to the centre of the plasma torus. Usually, analytical representations of the flux surface geometry are being used in the codes. Such representations, which are often expanded in Fourier series of the poloidal angle θ, are approximate solutions to the Grad-Shafranov equation (see,

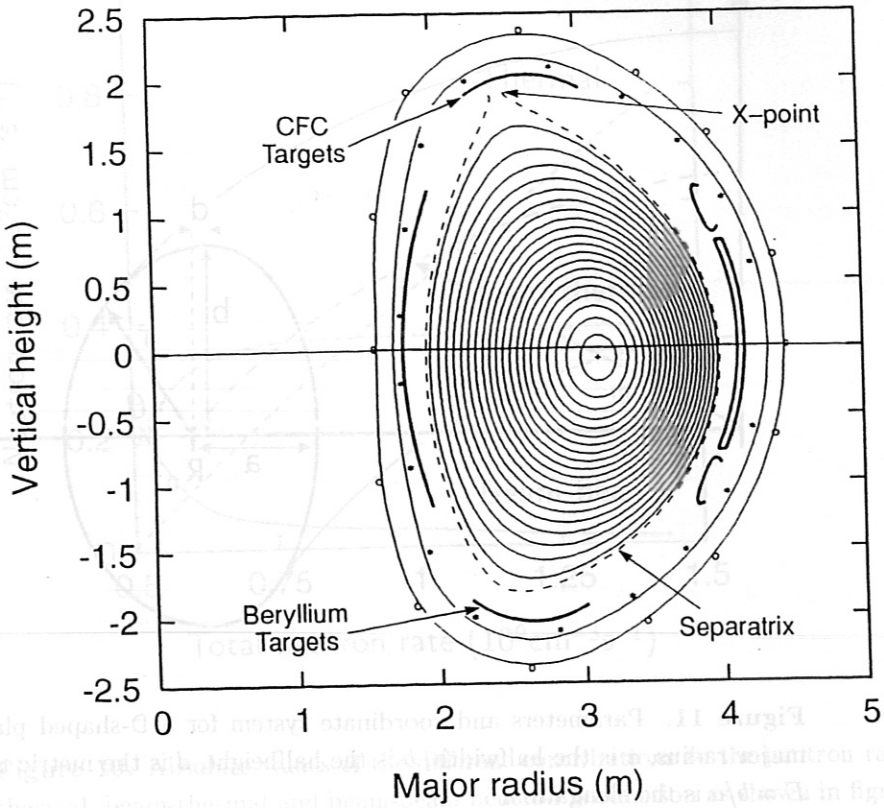

Figure 12. Magnetic configuration for the JET PTE discharge 26148 in which the magnetic axis was at 3.15 m, and the horizontal minor radius was 1.05 m. At the $\rho = 0.95$ flux surface, the elongation was 1.6. Shown are the separatrix, the X-point, the carbon fibre composite (CFC), and the beryllium targets (from JET Team, 1992).

e.g. Mukhovatov and Shafranov, 1971) obtained by using a variation method (Lao *et al* 1981). In most cases, a few terms of the Fourier series are sufficient to get reasonable accuracy for describing the flux surfaces. By using the first two terms in the Fourier expansion and assuming that the flux surfaces possess up-down symmetry, the flux surface coordinates (R, z) of a flux surface with label $\rho(\psi)$ can be represented as

$$R = R_1(\rho) - a\rho\cos\theta + \frac{1}{4}d(\rho)\cos 2\theta \tag{56}$$

$$z = E(\rho)\left(a\rho\sin\theta + \frac{1}{4}d(\rho)\sin 2\theta\right) \tag{57}$$

where the amplitude $R_1(\rho)$ describes the shift of the flux surfaces and the flux surface label ρ is normalized to the minor radius. Using the more convenient parameters $S(\rho)$ and $d(\rho)$, i.e. the Shafranov shift and the metric triangularity of the flux surfaces, rather

than $R_1(\rho)$, one can rewrite the expression (56). The resulting representation of the flux surface coordinates is (see e.g. Feng *et al* 1995)

$$R = R_0 + S(\rho) - \frac{1}{4}d(\rho) - a\rho\cos\theta + \frac{1}{4}d(\rho)\cos 2\theta \tag{58}$$

$$z = E(\rho)\left(a\rho\sin\theta + \frac{1}{4}d(\rho)\sin 2\theta\right), \tag{59}$$

where R_0 is the major plasma radius and the condition $a\rho \gg \frac{1}{4}d(\rho)$ has been used. An example of a numerically calculated and analytically represented flux surface geometry is shown in figure 12 for a magnetic configuration used in the JET PTE (preliminary tritium experiment) experiment (JET Team, 1992).

3.2.2. Measured plasma data

The most important standard input plasma data to the simulation calculations comprise the following measured experimental data (see, e.g., Orlinskij and Magyar 1988, Hutchinson 1987):

T_e: Electron temperature profiles can be measured by various methods. On tokamaks, the main methods for measuring electron temperatures are the emission intensity at harmonics of the electron cyclotron frequency (ECE), and Thomson scattering of laser radiation.

A simple relation linking the intensity of plasma radiation at the electron cyclotron frequency and its harmonics with the electron temperature makes ECE measurements on tokamaks very attractive. Profile information is obtained by the unambiguous dependence of the electron cyclotron frequency and the local magnetic field in the plasma. With this diagnostics, spatial resolutions of 1–5 cm and time resolutions of 1–20 μs with an overall accuracy of less than 10% can routinely be achieved.

The ability of measuring either localized electron temperatures and densities or electron temperatures from relative measurements alone is the main advantage of the Thomson scattering method. However, the need of a repetitively pulsed laser with pulse energies above about 5 J makes the determination of the time evolution of the temperature or density profiles difficult. The spatial resolution is typically less than 10 cm and the accuracy is less than 10%.

n_e: Electron density profiles are mainly measured by means of plasma interferometry. Since the phase shift in the probing beam with respect to a reference beam is measured directly, the interferometric method does not require absolute calibration. Although interferometric measurements are sensitive to vibrations and suffer from the large size of the measuring system, the time and spatial resolutions are relatively good. The spatial resolution depends on the number of probing beams, typically

5–10 on present tokamak experiments. The time resolution is in the order of 10^{-3} s and the accuracy is in the order of 10%.

T_i: Ion temperature profiles are difficult to measure. None of the various techniques currently used for determining the temperature (and density) of the basic ion components can be used without many cross-checks. The main methods used for measuring ion temperature profiles are charge-exchange recombination spectroscopy (CXRS), active neutral-particle analysis (NPA), and Doppler broadening measurements of spectral lines.

In recent years, charge-exchange recombination spectroscopy has become the standard diagnostic for measuring ion temperature profiles on large tokamaks. The method is based on recording the radiation produced when injected atoms interact with the plasma. For this purpose either a dedicated diagnostic injector or the neutral-beam injectors for auxiliary plasma heating can be used. Time resolutions of a few milliseconds and spatial resolutions of a few centimetres with an accuracy of about 10% can be achieved.

The conceptual basis of ion temperature profile measurements using active charge-exchange neutral-particle measurements relies on the local enhancement of the neutral atom density by an injected beam and, hence, on an increased probability of charge-exchange among plasma ions in the region occupied by the beam. The accuracy of the temperature measurement is determined mainly by the ratio of the neutral-atom flux from the beam region to the background flux from the rest of the plasma. Spectrum analysers record flux and energy spectrum of the escaping neutral-atoms which allows to determine the ion temperature. Furthermore, active charge-exchange neutral-particle analysis is the standard method for measuring ion velocity distributions directly.

Measurements of Doppler broadening can be made from the visible region to the X-ray region. In tokamaks the electron density is low and the Stark broadening is negligibly small, so that the line broadening is governed by the thermal motion of the plasma ions. Therefore deviations from Maxwellian velocity distributions have little effect on the measurement results.

Z_{eff}: Z_{eff}-profiles are routinely obtained by means of passive plasma spectroscopy. Due to the wide utilization of optical fibres, visible or near ultraviolet radiation is mainly being used for measuring Z_{eff}. Using continuum radiation, Z_{eff} is simply the factor by which the bremsstrahlung exceeds that of a pure deuterium plasma. Combining Z_{eff}-measurements together with impurity ion concentration measurements based on the emission intensity of spectral lines in the far ultraviolet (VUV) or X-ray regions (XUV), information about the dilution ratio $n_{\mathrm{D}}/n_{\mathrm{e}}$ with accuracies of typically 10-30% can be obtained.

Furthermore, for diagnostic purpose in the numerical calculations and for consistency checks it is useful to compare the calculated energy content of the plasma to the diamagnetic measurements. Since the poloidal field is much smaller than the toroidal field, an accurate measurement of the diamagnetic effect is on tokamaks difficult to achieve. Nevertheless, reliable measurements of the plasma energy with an accuracy of better than 20% have been achieved on many tokamaks.

3.2.3. Fokker-Planck models

In section 2.2, two important simplified Fokker-Planck equations for tokamak plasmas have been discussed, namely (i) the linearized 2D equation for well-passing particles and its high-energy approximation (subsection 2.2.1), and (ii) the linearized 2D equation including particle trapping (subsection 2.2.2). In subsection 2.2.3, various additional terms describing particle sources and losses and a simplified ICRH operator have been described. As already mentioned, for the simulation and analysis of neutron signals of auxiliary heated plasmas it is important to use models which describe the non-Maxwellian velocity distributions with sufficient accuracy. Furthermore, the computation time has to be kept reasonably short for routine analysis. Therefore, from the numerical point of view it is important to assess the applicability of the different simplified Fokker-Planck models for the simulation of neutron signals. In this context it is also important to obtain information on the errors introduced if a too simple model has been used.
It should be noted that the following main Fokker-Planck models: (a) the time-dependent 2D model for well-passing particles, (b) the steady-state 2D model for well-passing particles, (c) the time-dependent 1D model for well-passing particles, (d) the steady-state 2D model including effects of particle trapping, and the high-energy approximation of each model are simply limiting cases the more general time-dependent 2D Fokker-Planck model which includes effects of particle trapping. Therefore, in this subsection emphasis is placed on the latter model. Finally, for completeness, the various loss models and the RF modelling are briefly discussed.

- *Influence of particle trapping and anisotropic velocity distributions*
  In the most simple models, the magnetic field inhomogeneity along a field line is not taken into account, i.e. trapped particle effects are being neglected. However, the number of trapped particles can be quite large, depending on injection and tokamak geometries.
  Based on the solution of the 2D bounce-averaged Fokker-Planck equation, calculated neutron rates are plotted in figure 13 as functions of time for a test case plasma wit $T_e = T_i = 5$ keV, $n_e = n_D = 2 \times 10^{19} m^{-3}$ and 80 keV deuterium

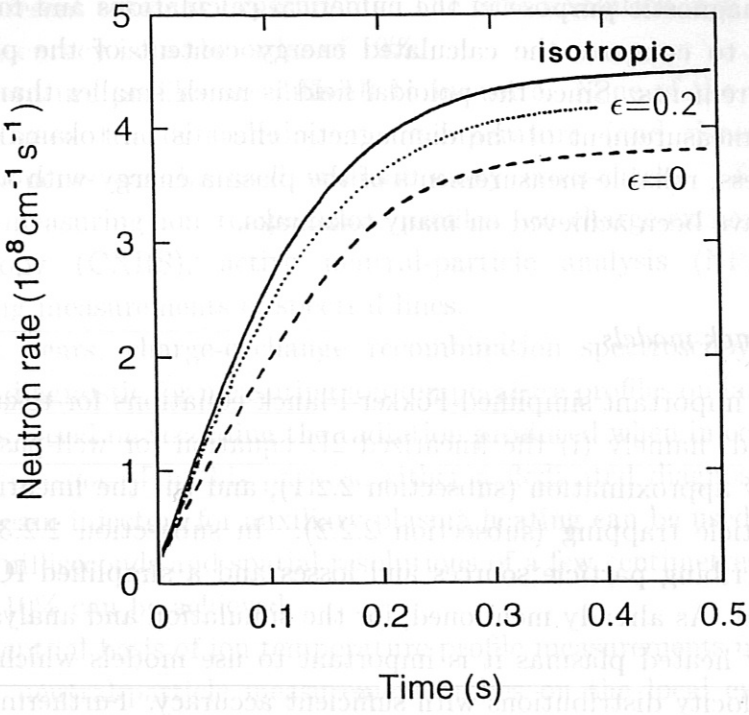

Figure 13. Time evolution of the D-D neutron rate for the test-case data with an injection source rate of $S_0 = 4 \times 10^{19}\mathrm{m}^{-3}\mathrm{s}^{-1}$ using different kinetic models. The neutron rate neglecting the anisotropy in the distribution is given by (——). The neutron rate taking the anisotropy fully into account but neglecting the effects of particle trapping (inverse aspect ratio $\epsilon = 0$) is indicated by the broken curve (– – –), (·····) is the anisotropic neutron rate for $\epsilon = 0.2$, respectively (after Wolle *et al* 1997b).

injection with a source rate of $4 \times 10^{19}\mathrm{m}^{-3}\mathrm{s}^{-1}$. The injection has been assumed to be tangential to the magnetic field. Shown are the calculated neutron rate neglecting the anisotropy in the distribution, the neutron rate taking the anisotropy fully into account but neglecting the effects of particle trapping (inverse aspect ratio $\epsilon = 0$), and the anisotropic neutron rate for $\epsilon = 0.2$, respectively (after Wolle *et al* 1997b). Immediately after switching on the neutral beam, fast particles exist mainly in the passing region. As these particles slow down they will be scattered in pitch angle space and the strong anisotropy around the injection angle due to the beam will be more and more averaged out. Finally, in the thermal region the velocity distribution is completely isotropic. It should be noted that trapped particles only affect anisotropic velocity distributions and, hence, only the 'beam-beam' component of the fusion reactivity is affected by trapped particles. With decreasing source rate and increasing background density the fast particle density

decreases and the ion velocity distribution becomes less anisotropic. Therefore, for realistic plasma simulation the final error on the volume-integrated neutron rate (neutron source strength) is, owing to the peakedness of the particle deposition, density and temperature profiles, only in the order of a few percent which is less than the normal 10%-level of accuracy of the neutron counters. Thus, the neglect of particle trapping in volume-integrated neutron simulation and interpretation calculations is for most NBI-heated plasma regimes well justified. The effect of particle trapping in mixed ICRF and NBI heated plasmas has also been examined (Hellsten *et al* 1985). Here too, it was concluded that trapped particle effects are not very important in the calculation of the fusion reactivities. On the other hand, for some cases when trapping effects should be included in the calculation of the velocity distributions, the simplified approach of an expansion in eigenfunctions of the pitch angle scattering operator is satisfactory.
In addition, it can be seen that in the simulation and interpretation of neutron rates (but not for the neutron spectra) the 2D character, i.e. anisotropy, of the velocity distribution can also often be neglected.

- *Time-dependence*
  The results shown in figure 13 demonstrate that it is important to include the time-dependence, especially when the background parameters or the injection power vary on a time scale shorter than, or comparable to the ion-electron slowing-down time. This is often the case in large fusion plasma devices.

- *Influence of the various loss models on the calculated neutron signals*
  To some extent the calculated distribution function and, hence, the neutron rate, depend on the type of loss model being used in the Fokker-Planck equation. As mentioned in subsection 2.2.3, usually simple models such as the charge-exchange model, equation (39) or the Gaussian loss term, equation (42), are being used. The charge-exchange time often is assumed to be constant, which is a reasonable assumption in the energy range below about 40 keV. Both, the charge-exchange model and the Gaussian loss term give essentially the same results in the low energy range. However, the charge-exchange model is suppressing the tail of the velocity distribution more strongly than the Gaussian loss term which removes only thermalized particles (c.f. Anderson *et al* 1988). This can also be ssen from the analytical pitch angle averaged steady-state solution of the kinetic equation. With the approximate expression (25) of the collision operator and the f/τ_{cx} loss term, the solution for the fast particles is given by (see e.g. Heidbrink and Sadler 1994):

$$f_b(v) = \frac{P_{nbi}}{4\pi E_{inj}} \frac{\tau_s \sigma (v_{inj} - v)}{(v^3 + v_\alpha^3)^{1-\tau_s/3\tau_{cx}}} \left(1 + \frac{v_\alpha^3}{v_{inj}^3}\right)^{-\tau_s/3\tau_{cx}} \qquad (60)$$

from which the expression (52) can be obtained for $\tau_{cx} \to \infty$. A comparative study of the influence of different loss models on the evolution of the velocity distributions of 1 MeV tritons and 0.8 MeV ^{3}He ions has been carried out by Yamagiwa (1992). It was concluded that losses due to radial diffusion and losses due to a charge-exchange model can give almost the same time evolution in the velocity distribution and the 14 MeV neutron emission, but small differences occur in the neutron emission profiles. However, it should be noted that in the Fokker-Planck models given in section 2.2, the collisional time scale is the relevant one. When using a simple f/τ_{cx}-model, this implies that $\tau_{cx} \gg \tau_b$ in order not to violate the underlying time scale expansion of the kinetic equation.

From the above it can be concluded that for simulation and analysis of neutron source strength measurements for NBI heated plasmas a linearized, time-dependent 1D Fokker-Planck equation including simple loss and source terms neglecting effects of particle trapping is sufficiently accurate. However, it should be noted that the anisotropy has to be taken into account in the calculation of the neutron spectra.

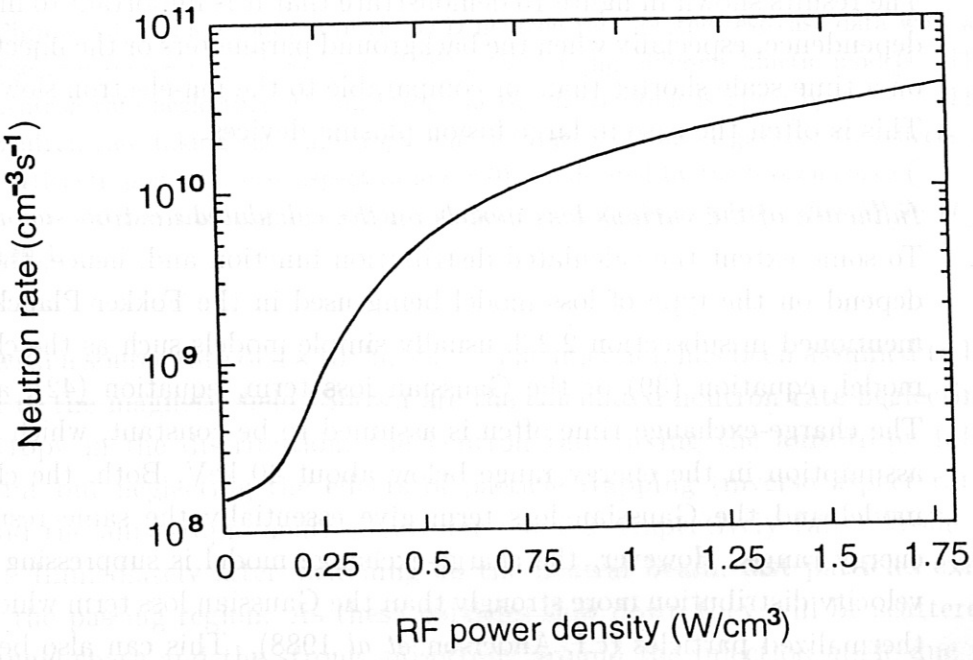

Figure 14. Calculated D-D neutron rate for second harmonic ICRF heating of a Maxwellian plasma as a function of the absorbed RF power. The calculation has been carried out for $|E_-|/|E_+ = 3$ with $k_\perp = 0.5$ cm^{-1} and a plasma temperature of 7 keV. The fusion reaction rate among the non-thermal particles themselves has been neglected (from Anderson *et al* 1987).

- *Effect of ICRF heating on the neutron rate*
  In the case of ICRF heating, the neutron rate is a strong function of the absorbed RF power. Therefore, by measuring the energy spectrum of the fusion products and the fusion yield, information on the RF power absorption can be obtained (see e.g. Chrien *et al* 1981, Heidbrink 1984). For second harmonic heating of an initially Maxwellian plasma, the ions in the high energy part of the distribution functions will be heated predominantly, leading to the formation of a strong high energy tail. On using a simplified model according to subsection 2.2.3, the effects due to second harmonic RF heating on the neutron production can be estimated. As an example, the calculated D-D neutron rate neglecting reactions among the non-thermal particles themselves is shown in figure 14 as a function of the absorbed RF power (Anderson *et al* 1987). It was also found by Anderson *et al* (1987) that the neutron rate depends sensitively on the background temperature, and that the results of the semi-analytical isotropic model used are in good agreement the results of more sophisticated numerical 2D calculations.

3.2.4. Error analysis for neutron rate calculations

For neutral-beam-heated plasmas the neutron rate depends in a complicated manner on different plasma parameters such as ion and electron temperatures, densities and neutral-beam power. Furthermore, comparatively small changes in these input data can sometimes lead to rather strong changes in the neutron rates. With a fast numerical scheme for calculating neutron rates in the presence of neutral-beam heating it is possible to carry out a sensitivity analysis. This has been proposed and carried out for the first time by Wolle *et al* 1991 for JET based on 1,200 calculated data points. Recently, calculations for TEXTOR are also available (Wolle *et al* 1997). Based on such a sensitivity study the error bars on a neutron rate calculation can be related to the errors in the input plasma data. This also fixes the ranges of application for an interpretative plasma parameter determination. For a local sensitivity analysis the relative change in the neutron rate Q_n due to variations of the five most important input parameters, viz., ion and electron temperatures T_i and T_e, deuteron and electron densities n_D and n_e and injection source rate s_0 is calculated. Then the relative change in Q_n is simply:

$$\frac{\mathrm{d}Q_n}{Q_n} = \frac{T_i \partial Q_n}{Q_n \partial T_i}\frac{\mathrm{d}T_i}{T_i} + \frac{T_e \partial Q_n}{Q_n \partial T_e}\frac{\mathrm{d}T_e}{T_e} + \frac{n_D \partial Q_n}{Q_n \partial n_D}\frac{\mathrm{d}n_D}{n_D} + \frac{n_e \partial Q_n}{Q_n \partial n_e}\frac{\mathrm{d}n_e}{n_e} + \frac{s_0 \partial Q_n}{Q_n \partial s_0}\frac{\mathrm{d}s_0}{s_0}. \tag{61}$$

The sensitivity factors λ_{T_i}, λ_{T_e}, λ_{n_D}, λ_{n_e} and λ_{s_0} which describe the influence of ion and electron temperature, deuteron and electron density and source rate are:

$$\lambda_{T_i} = \frac{T_i \partial Q_n}{Q_n \partial T_i}, \quad \lambda_{T_e} = \frac{T_e \partial Q_n}{Q_n \partial T_e}, \quad \lambda_{n_D} = \frac{n_D \partial Q_n}{Q_n \partial n_D}, \quad \lambda_{n_e} = \frac{n_e \partial Q_n}{Q_n \partial n_e}, \quad \lambda_{s_0} = \frac{s_0 \partial Q_n}{Q_n \partial s_0}. \tag{62}$$

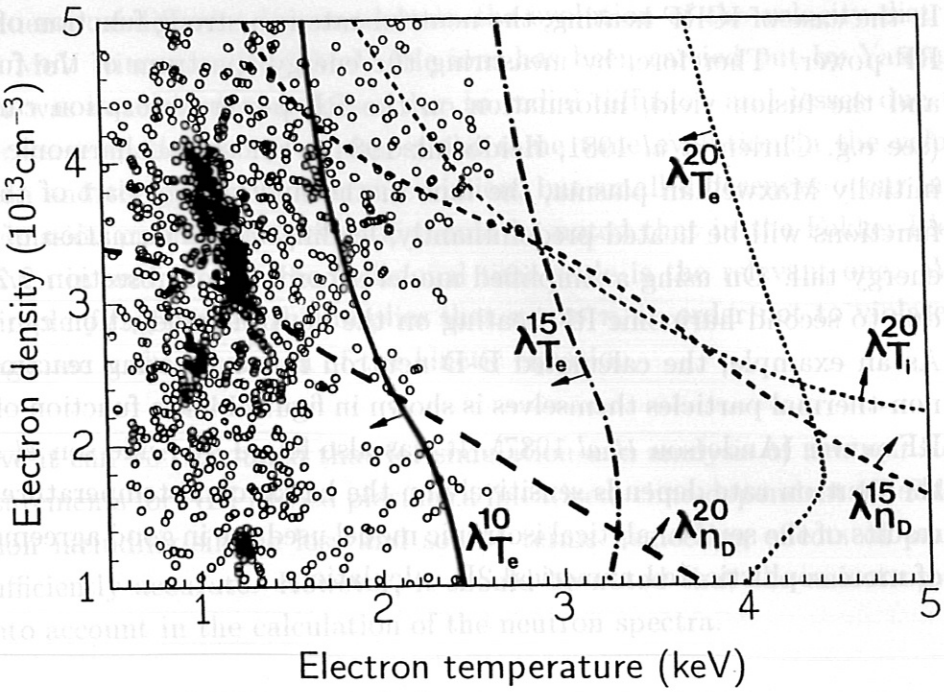

Figure 15. Sensitivity functions for neutral-beam-heated TEXTOR discharges represented in a n_e vs T_e diagram. Plotted are the functions $\lambda^{20}_{T_i}$, $\lambda^{10}_{T_e}$, $\lambda^{15}_{T_e}$, $\lambda^{20}_{T_e}$, $\lambda^{15}_{n_D}$ and $\lambda^{20}_{n_D}$ for a source rate of $s_0 = 10^{14}\mathrm{m}^{-3}$ and $T_i = T_e$ together with some measured data points from the TEXTOR data base. The arrows point in the direction of increasing sensitivity of the plasma parameter. The exponents indicate the relative change required for a 10% change in the neutron rate (from Wolle *et al* 1997).

These factors are again functions of all the other plasma parameters. It should be pointed out that the higher the value of one of these factors, the stronger is the neutron rate dependence on the corresponding plasma parameter. All possible physically reasonable combinations with a sufficient number of data points (reasonable are 5-10) for each parameter in the five dimensional parameter space $Q_n(T_i, T_e, n_D, n_e, s_0)$ relevant to the experimental regimes have to be calculated. The physical restrictions were as follows: $n_e \geq n_D$, $T_i \geq T_e$ and moderate fast-ion densities which implies $n_D \geq s_0\tau_E$ where τ_E is the energy relaxation time. Of course, in all these calculations quasi-neutrality has to be maintained. Then, empirical fit-functions for the sensitivity factors can be obtained which can be used for error estimations or to determine the range of applications for neutron interpretation calculations. For convenience, it is sufficient to limit the discussion on the class of sensitivity factors where a 10, 15 or 20% change in the relevant input parameter leads to a 10% change in the neutron rate, i.e. the sensitivity factors $\lambda^{10}_{..}$, $\lambda^{15}_{..}$ and $\lambda^{20}_{..}$, respectively.

As an illustrative example, figure 15 shows the sensitivity factors $\lambda^{20}_{T_i}$, $\lambda^{10}_{T_e}$, $\lambda^{15}_{T_e}$, $\lambda^{20}_{T_e}$, $\lambda^{15}_{n_D}$ and $\lambda^{20}_{n_D}$ plotted for a typical source rate of $s_0 = 10^{14}\mathrm{m}^{-3}$ with $T_i = T_e$ in a n_e vs T_e diagram, together with measured data points from the TEXTOR-94 data base. It turns out that, in general, an ion temperature determination with sufficient accuracy would be possible for plasmas with electron temperatures above ≈ 4 keV and medium-to-high densities ($> 3 \times 10^{19}$ m^{-3}). For small tokamaks such as TEXTOR this is not feasible. However, for example at JET, a small number of discharges could be identified where an ion temperature determination is possible. The determination of the deuterium density offers a much wider range of application, covering many more experimentally-accessible plasma conditions at different tokamak experiments. However, there is still a rather strong influence of the electron temperature. Therefore, accurately measured electron temperatures are mandatory for determining the deuteron density with sufficient accuracy.

3.3. Computation

The simulation of the D-D neutron emission in tokamaks requires different dedicated computer codes. Some of these code are needed to calculate necessary input data, such as the power deposition profiles of the auxiliary heating. Therefore, the first subsection contains a brief overview on the concepts and available computer codes for calculating the power deposition profiles in the case of neutral-beam heating. Other auxiliary heating systems, such as for example ICRH, have not been included because in this review emphasis is placed on the simulation and interpretation of neutron signals emitted from NBI heated plasmas. Then, computer codes for calculating D-D neutron rates and neutron spectra are summarized. Finally, a brief subsection is concerned with the computational requirements and available codes for neutron transport simulations.

3.3.1. Neutral-beam deposition codes

Neutral beam injection (NBI) has become a widely used method for auxiliary heating of tokamak plasmas (Speth 1989). In large tokamaks such as JET, TFTR and JT-60U it is one of the main auxiliary heating methods, having an injection potential of more than 20 MW of fast neutral atoms into the plasma (Duesing *et al* 1987, Grisham *et al* 1985, Matsuda *et al* 1987). Direct measurements of particle, momentum and energy absorption from the injected beam are very difficult and are thus being routinely replaced by computations. The main input data for such calculations comprise accurate descriptions of the beam and the plasma geometries, and measured density and temperature profiles of ions and electrons.

When the neutral particles pass through the plasma, they will be removed from

the incident beam through interactions with the background plasma, i.e. ionization and charge-exchange. As a consequence, the intensity $I_{\mathrm{S},j}$ of the jth energy constituent of the incident beam is reduced on its way through plasma. (For hydrogenic ion sources the magnitude of the neutral particle velocities has three discrete values corresponding to the applied voltage, i.e. full energy, half-energy and one-third energy components.) The transmitted intensity $I_j(\boldsymbol{x}_0)$ at the observation point $\boldsymbol{x}_0$ with the distance ℓ_0 from the source follows is given by

$$I_j(\boldsymbol{x}_0) = I_{\mathrm{S},j} \exp\left(-\int_{\ell_\mathrm{e}}^{\ell_0} \frac{\mathrm{d}\ell}{\lambda_j}\right) \mathrm{d}\boldsymbol{v}_j \tag{63}$$

where the integration is performed along the trajectory from the entry point into the plasma at a distance ℓ_e from the source to the observation point. The effective mean free path length λ_j the for beam particles with velocity v_j can be written as

$$\frac{1}{\lambda_j} = \frac{\langle \sigma_{\mathrm{e}i} v_\mathrm{e} \rangle}{v_j} n_\mathrm{e} + \frac{\langle (\sigma_{\mathrm{cx}} + \sigma_{ii})\, v_\mathrm{rel} \rangle}{v_j} n_i + \sum_k \sigma_k n_k. \tag{64}$$

Here, $\langle \sigma_{\mathrm{e}i} v_\mathrm{e} \rangle$ is the product of the electron impact ionization cross section and the electron velocity averaged over a Maxwellian with the local electron temperature. Furthermore, n_e, n_i are the local electron density and the local density of the isotopes of the injected ion species, and σ_{cx}, σ_{ii} are the charge-exchange and ion impact ionization cross sections as given, for example, in Riviere (1971), Sweetman (1973), Freeman and Jones (1974) and Janev *et al* (1989). Usually, it is assumed that the beam velocity is small as compared with the electron mean thermal velocity, i.e. $v_\mathrm{rel} \approx v_\mathrm{e}$. The product of the total cross section and the relative velocity, v_rel, is averaged over an appropriate velocity distribution for the dominant ions in the plasma. Furthermore, the total capture cross section for the k impurity ion species with the local densities n_k is σ_k. The mean thermal velocity of the impurity ions has been neglected in equation (64) because it is usually much smaller than the beam velocity and thus $v_\mathrm{rel} \approx v_j$.

The differentiation of equation (63) with respect to the path length ℓ gives the number of neutral particles trapped per second in $\mathrm{d}\ell$ at the observation point. With the relations $\mathrm{d}\boldsymbol{v}_j = v_j^2 \mathrm{d}\Omega$ and the volume $\mathrm{d}V = \ell_0^2 \mathrm{d}\Omega \mathrm{d}\ell$, the local beam deposition rate is:

$$n_{j,\mathrm{dep}}(\boldsymbol{x}_0) = \frac{1}{\lambda_j(\boldsymbol{x}_0)} \frac{v_j^2}{\ell_0^2} I_{\mathrm{S},j} \exp\left(-\int_{\ell_e}^{\ell_0} \frac{\mathrm{d}\ell}{\lambda_j}\right). \tag{65}$$

From this, a spatial deposition distribution can be obtained by varying the observation point through the total plasma volume and accounting for first orbit losses. Finally, a deposition profile as a function of the flux surface radius can be derived through summation of the particles born on the same flux surface and subsequent averaging over their drift orbits.

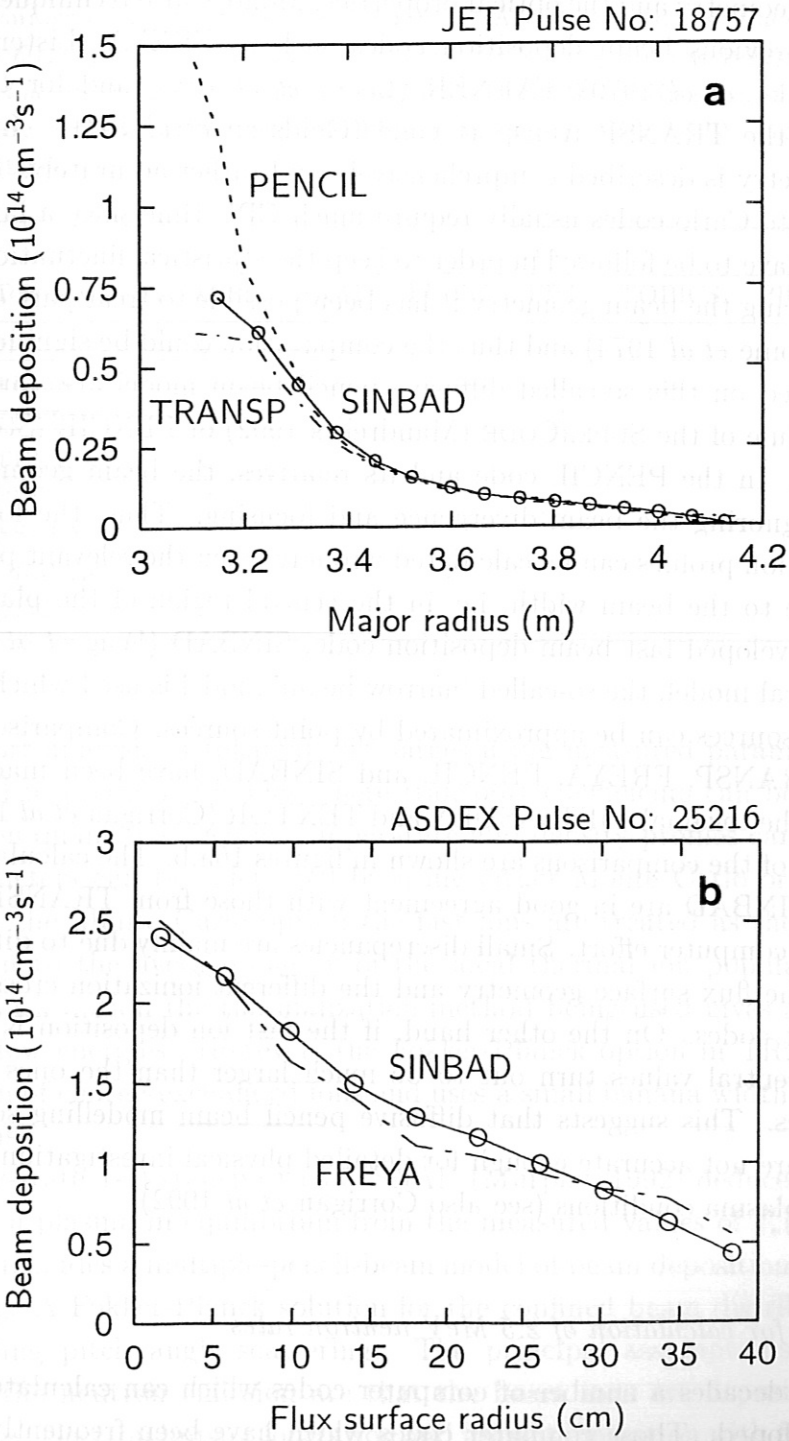

Figure 16. Examples of deposition profiles calculated with different codes for JET (a) and ASDEX (b) plasma discharges (after Feng *et al* 1995).

Due to the multiple dimensionality of the source distribution function associated with the beam geometry and the optical properties, Monte Carlo techniques have usually been used in previous beam deposition codes such as FREYA (Lister *et al* 1976), NFREYA (Fowler *et al* 1979), FAFNER (Lister *et al* 1985) and for the deposition calculations in the TRANSP transport code (Goldston *et al* 1981). In these codes, the beam geometry is described comprehensively and rather accurately. Although very successful, Monte Carlo codes usually require much CPU time since a large number of neutral atoms have to be followed in order to keep the statistical fluctuations sufficiently small. By reducing the beam geometry it has been possible to treat part of the problem analytically (Rome *et al* 1974) and thus the computation could be significantly speeded up. Codes based on this so-called diffusive pencil beam model are, for example, the deposition module of the SUPERCODE (Mandrekas 1992) or PENCIL (Stubberfield and Watkins 1987). In the PENCIL code and its relatives, the beam geometry is mainly simplified by ignoring the beam divergence and focusing. Thus, the local deposition and the deposition profiles can be calculated wrongly when the relevant plasma sections are comparable to the beam width, i.e. in the central region of the plasma torus. In the recently developed fast beam deposition code, SINBAD (Feng *et al* 1995), a more refined analytical model, the so-called 'narrow beam' model is used which assumes that the actual ion sources can be approximated by point sources. Comparisons of different codes, viz., TRANSP, FREYA, PENCIL and SINBAD, have been made for selected discharges for the tokamaks JET, ASDEX and TEXTOR (Corrigan *et al* 1992, Feng *et al* 1995). Results of the comparisons are shown in figures 16a,b. The calculated deposition profiles from SINBAD are in good agreement with those from TRANSP and FREYA but save much computer effort. Small discrepancies are mainly due to differences in the treatment of the flux surface geometry and the different ionization cross sections used in the different codes. On the other hand, if the fast ion deposition is obtained with PENCIL, its central values turn out to be much larger than the ones obtained with the other codes. This suggests that diffusive pencil beam modelling sometimes gives results which are not accurate enough for detailed physical investigation of present-day experimental plasma conditions (see also Corrigan *et al* 1992).

3.3.2. Codes for calculation of 2.5 MeV neutron rates

Over the past decades a number of computer codes which can calculate neutron rates has been developed. Those computer codes which have been frequently used for D-D neutron production calculations on various tokamaks are summarized in table 4 and are described briefly below.

The Monte Carlo transport code TRANSP (Goldston *et al* 1981, Hawryluk *et al* 1980, Strachan *et al* 1981) has several modes of operation. Although its main use is

Table 4. Computer codes used in literature for D-D neutron rate calculations on various tokamaks. Selected references: TRANSP (e.g. Adams *et al* 1991, Jassby *et al* 1991, Ongena 1994, Strachan *et al* 1981), SNAP (e.g. Murphy 1992), FIFPC (England *et al* 1977), FPT (e.g. Killeen *et al* 1986), TOPICS (e.g. Nishitani *et al* 1994), PION-T (e.g. Eriksson *et al* 1993), NRFPS (e.g. Wolle *et al* 1994, Wolle *et al* 1997, Wolle *et al* 1990).

	Code						
Tokamak	TRANSP	SNAP	FIFPC	FPT	TOPICS	PION-T	NRFPS
JET	✓					✓	✓
JT-60U					✓		
TFTR	✓	✓		✓			
TEXTOR	✓						✓
PLT	✓			✓			
ASDEX							✓
ORMAK			✓				
DITE				✓			

for the transport analysis of tokamak discharges using measured parameters, it is also frequently used in predictive modes where transport coefficients can be assumed, and consequences on quantities such as temperature and density profiles can be calculated. Fast ion parameters can be calculated by using either Monte Carlo or Fokker-Planck techniques. In the Monte Carlo option the fast ions are treated as thermalized when they slow down to the average energy of the local thermal ion population ($\frac{3}{2}T_\mathrm{i}$). In the Fokker-Planck option the thermalization method being used gives a more realistic simulation at low energies. However, the Fokker-Planck option in TRANSP provides no reabsorption of charge-exchanged ions and uses a small banana width approximation for the fast ions.

The steady-state 1-D transport code SNAP (Murphy, 1992) deduces the transport coefficients for a plasma in equilibrium from the measured values of $T_\mathrm{e}(r)$, $T_\mathrm{i}(r)$, $n_\mathrm{e}(r)$ and $Z_\mathrm{eff}(r)$. It includes a multiple-pencil-beam model of beam deposition including first-orbit averaging. A Fokker-Planck solution for the confined beam distribution function is used including pitch angle scattering. The principal assumptions in the SNAP calculation of the neutron emission are that the beam ions are deposited radially by charge-exchange, electron impact ionization and impact ionization with fast and thermal ions, and they do not experience radial transport during their collisional slowing-down. It was pointed out by Strachan *et al* 1993 that the SNAP calculated neutron emission is systematically underestimating the neutron rate by about 10%. It was concluded that the main reason for this is probably due to the neglect of the time-dependence in the

SNAP calculations.

The FIFPC code (Fowler *et al* 1976, England *et al* 1977) is a time-dependent Fokker-Plank code which takes effects of pitch angle scattering, energy diffusion into account. Effects due to the toroidal electric field are also included. Loss region losses due to trapped fast ions hitting the wall are included in an approximate manner. The radial transport of the fast ions during slowing-down is not considered.

The Fokker-Planck transport code FPT (Killeen *et al* 1986) solves time-dependent non-linear Fokker-Planck equations in two-dimensional velocity space for the energetic ion distributions as a function of the minor radius in the tokamak. In addition, this code solves one-dimensional radial transport equations for the bulk plasma densities and temperatures.

At JT-60 the tokamak transport code system TOPICS (tokamak performance prediction and interpretation system) has been developed (see, e.g., Nishitani *et al* 1994). This code can be used for steady-state and time-dependent analysis. It treats the MHD equilibrium in two dimensions and the transport in one dimension.

The time-dependent PION-T code (Eriksson *et al* 1993) has been developed for routine analysis of ICRF heated plasmas. Two main versions of the code exist, one with zero banana with approximations and one in which a simplified model for taking the finite width of the drift orbits into account. However, the zero banana width version should only be used for calculations with relatively low power levels. Using the second version of the code, good agreement can be obtained for higher power levels. In PION-T, simplified but sufficiently accurate models for calculating the ICRH power deposition and velocity distributions are being used in order to make the code suitable for routine analysis. The code calculates many important quantities such as fusion neutron rates and fast ion energy content for comparison with experimental measurements.

The neutron rate interpretation code NRFPS (Wolle *et al* 1994, Wolle *et al* 1995) is based on the time-dependent Fokker-Planck equation including relevant source and loss terms. From the above described codes it is the only code dedicated for time-dependent interpretation of neutron emission rate measurements. It uses measured neutron data directly as input and also includes a package for calculating line-integrated time-dependent neutron spectra. Although it was originally developed for interpretation of neutron measurements, with additional packages the code has also been used for interpretation of charge-exchange recombination spectra (von Hellermann *et al* 1993, Gerstel *et al* 1997) and active neutral particle analysis spectra (Rust *et al* 1995). The approach used in the solution of the Fokker-Planck equation in the code, is to expand the distribution function in the eigenfunctions of the pitch angle scattering operator. Trapping effects can be included by using an appropriate set of pre-calculated eigenfunctions (Wolle *et al* 1997b).

3.3.3. Codes for calculation of 2.5 MeV neutron spectra

The energy spectrum of neutrons produced in plasmas with deuterium injection has been measured on various tokamaks such as e.g. JET (Jarvis *et al* 1986, Elevant *et al* 1992, Olsson *et al* 1993), TFTR (Strachan *et al* 1988) PLT (Strachan *et al* 1979), ORMAK (Morgan and England, 1975) or ASDEX (Wolle *et al* 1996) demonstrating the utility of neutron spectra measurements for routine diagnostic of fusion plasmas. Neutron spectrometry is used to identify the production mechanisms of the emitted neutrons and to obtain information on the energy distributions of the reacting ions e.g. the temperature.
For thermonuclear plasmas this is a fairly straightforward procedure. As already shown in subsection 2.1.4, in this case the energy distribution of the emitted neutrons is approximately Gaussian. In contrast to Maxwellian plasmas, the neutron energy spectra for plasmas with deuterium injection are not only temperature dependent.
Instead, they also depend on the various injection data such as injection energy, injection angle, species mix and on plasma data, such as deuterium and electron densities and temperatures. Furthermore, the toroidal plasma rotation has an important impact on the shifts of the spectra (Scheffel, 1984). Due to the anisotropy of the velocity distribution, shape and energy location of the spectra are strongly influenced by the observation angle: if spectra are observed under small pitch angles, they are shifted up to higher energies and vise versa (see figure 17). It can also be seen in figure 17 that the low-energy wings of the 0° spectra, the high-energy wings of the 180° spectra, and the wings of the 90° spectra show no dependence on the ion temperature. In this example it is also interesting to note that with increasing temperature the shape of the 90° spectra becomes more Gaussian. The reason is that with increasing ion temperature the isotropic part of the velocity extends to higher energies. This, together with the increasing temperature of the background plasma, leads to an increasing neutron production around 2.45 MeV. The wings away from 2.45 MeV are mainly due to reactions of high-energetic deuterons with bulk ions and, hence, they are only little affected by changes in the ion temperature.

Thus, in conclusion, analytic treatment is not suited for interpretation and analysis of measured neutron spectra in these cases. Instead, the problem has to be tackled numerically involving the calculation of the velocity distributions of the reacting ions (e.g. by means of an appropriate Fokker-Planck formalism) and the calculation of the energy dependent probability of neutron emission per steradian. Against this background, a number of computer codes for calculating neutron spectra has been developed, such as, for example, NSPEC (Scheffel 1984), LINE (Slaughter 1985), FSPEC (Sadler *et al* 1996) and NSOURCE (Wolle *et al* 1995). All these codes are based on Monte Carlo techniques. The small differences in the results of the codes can be

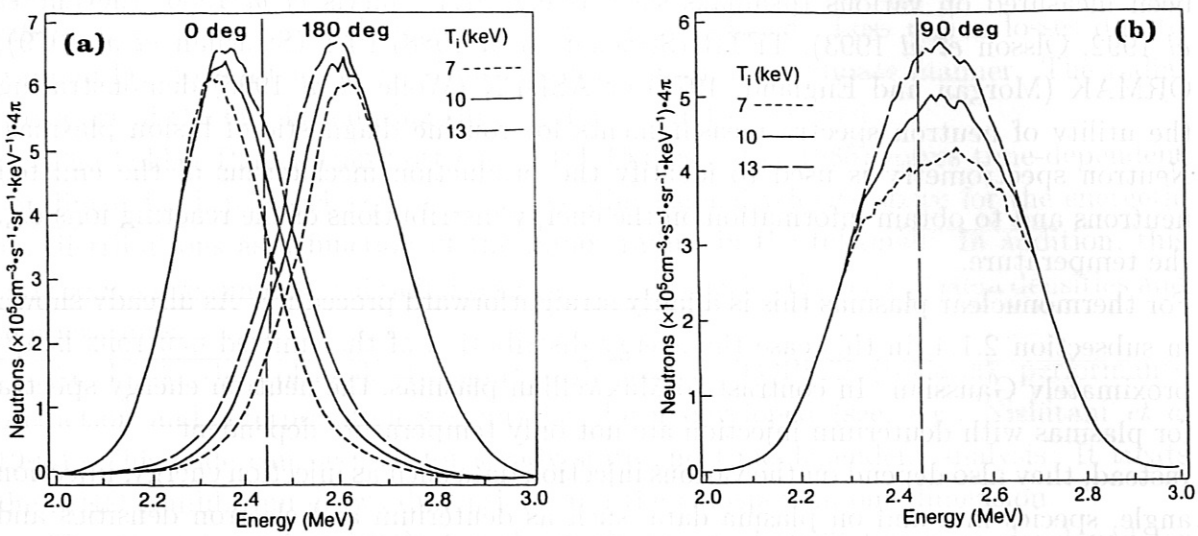

Figure 17. Calculated D-D neutron spectra from the NSOURCE Monte Carlo code using a 2D velocity distribution from the NRFPS code. The plasma data were as follows: $n_e = 2.5 \times 10^{19}\mathrm{m}^{-3}$, $n_D = 1.5 \times 10^{19}\mathrm{m}^{-3}$, $Z_{\mathrm{eff}} = 3.0$, $T_e = 6\,\mathrm{keV}$ and 80 keV D^0-injection with a source rate of $S_0 = 4 \times 10^{19}\mathrm{m}^{-3}\mathrm{s}^{-1}$ and an injection angle of 60^0. For the simulations 800,000 Monte Carlo samples and ion temperatures of $T_i = 7, 10, 13\,\mathrm{keV}$ have been used. The emission direction was set to 0°, 180° (a) and 90° (b) to the direction of the magnetic field (after Wolle *et al* 1995).

explained by the different cross section data used and differences in the Monte Carlo importance sampling techniques.

As input each of the above mentioned codes requires the velocity distributions of the reacting particles. Since the routine analysis of spectra requires fast calculation of the distribution functions, analytical approximations are often used. However, despite being useful for quick approximate calculations, their use for high temperature plasmas can be severely restricted for the following reasons:

(i) Analytic modelling of the pitch angle scattering operator in the Fokker-Planck equation is difficult and the approximate solutions are rather crude in the velocity region where pitch angle scattering becomes important. Thus, the anisotropy of the distribution function is not always approximated accurately enough.

(ii) The collision coefficients and the injection source terms in the Fokker-Planck equation have been simplified in order to derive approximate analytical expressions

for the distribution functions.

(iii) Analytical expressions are being derived from the stationary Fokker-Planck equation. Thus, their application for dynamic non-stationary plasmas is quite questionable.

Therefore, a numerical solution of the 2D time-dependent Fokker-Planck equation including relevant source and loss terms and collision coefficients without high-energy approximations or the neglect of diffusive terms should be used for calculating the neutron energy spectra.

Results of sophisticated time-dependent simulations of line-integrated 2.45 MeV neutron spectra for plasma discharges covering a wide range of experimental conditions with deuterium neutral beam injection have only been reported for JET (Wolle *et al* 1995, Wolle *et al* 1994). It could be shown that the simulated neutron energy spectra agreed well with measurements of the JET time-of-flight spectrometer and independent nuclear emulsion measurements where available.

3.3.4. Neutron transport simulation

The neutrons emitted from the plasma hit structural components of the tokamak and its diagnostic systems where they can be scattered and to some extent absorbed. Therefore, the initial direction of emission, the initial energy spectrum, and the number of neutrons will be altered. Finally, some neutrons will reach a neutron detector system and, with a certain probability, produce a signal which depends on the detector properties as well as on the properties of the incident neutrons. Unfortunately, in the energy range where the initial virgin neutron spectra are located, it is not possible to discriminate between scattered and non-scattered neutrons. Thus, the effects due to scattering and absorption can severely restrict the optimal use of a neutron measuring system for plasma diagnostic purposes. In experimental neutron diagnostics, therefore, much effort is devoted to reduce the neutron scattering background. This can to some extent be achieved by appropriate positioning of the neutron detectors (e.g. for the counters and activation samples), or by using dedicated narrow collimator systems (e.g. for the spectrometers). Furthermore, by carrying out *in situ* calibrations with conveniently small and strong neutron sources it is sometimes possible to directly account for the scattering background.

However, it is also possible to assess the effects due to neutron scattering and attenuation in the material structure on the measured detector signal entirely by computational means. From the numerical point of view, a decision between numeric-deterministic method and Monte Carlo methods has to be made. The convergence rate of Monte Carlo calculations is independent from the dimensionality of the problem, whereas for numeric-

deterministic methods it deteriorates with increasing dimensionality. In addition, the treatment of complex geometrical and scattering properties is for numeric-deterministic codes much more difficult than for codes based on Monte Carlo methods. Therefore, the Monte Carlo method is commonly preferred. The requirements for neutron transport calculations comprise modelling requirements and numerical aspects as follows:

(i) In Monte Carlo neutron transport calculations with complex geometry, most time is spent for tracking the simulated neutrons through the geometry model. Therefore, a good algorithm for neutron tracking may significantly reduce the computational cost of Monte Carlo calculations.

(ii) The variance and, thus, the number of Monte Carlo particles required to achieve a certain degree of accuracy can be reduced by applying non-analogue Monte Carlo techniques like importance sampling or particle splitting (Lux and Koblinger 1990).

(iii) A realistic neutron source model which includes the spatial dependence of neutron production as well as the anisotropy of neutron production and the neutron birth spectra is needed. Its ingredients are the distribution functions of the fusing ions, the fusion reaction cross sections and adequate numerical methods.

(iv) A geometry model of the fusion device including material compositions is required. The relevance of the various components for neutron transport calculations and, thus, the accuracy required for their modelling may depend on the specific calculation to be performed. Various components have to be considered: major structural components (e.g. inner and outer vacuum vessel, coil system and support structure), components inside the inner vacuum vessel (e.g. divertor plates) and relevant structural components in the surroundings of the neutron detectors (e.g. diagnostic ports, collimators, detector support structures and the detectors themselves).

(v) The cross sections for the interaction of neutrons with matter are needed. In the relevant neutron energy range of 0.5–15 MeV, major concerns are high energy resolution, accurate angular distributions of secondary neutrons and coupled energy-angle distributions of secondary neutrons for inelastic reactions.

(vi) The detector response function has to be taken into account. It usually depends on neutron energy and may in addition depend on incident angle and on the positio inside the detector.

The approach of assessing the effects due to neutron scattering on the detector signals by means of Monte Carlo simulations has been followed at various tokamaks. Many of the reported results relate to cross-checks of the calibration factor of the neutron counters, such as for TFTR (e.g. Ku *et al* 1991), Alcator C-Mod (Fiore *et al* 1992), JT-60U (Nishitani *et al* 1992) or JET (e.g. Laundy and Jarvis 1993). However, the degree of reliability of the Monte Carlo simulations depends on the care with which the tokamak,

the detector and their environment have been modelled and, in addition, the accuracy of the transport simulations is very difficult to estimate. Partly, this problems can be overcome by selecting measurement positions inside the vacuum vessel as close as possible to the plasma and using neutron activation methods for determining the neutron fluence at the measuring point. Thus, activation measurements and in particular multi-foil analysis methods, i.e. the use of several activation samples with different activation thresholds, constitute a valuable test of the neutron transport methodology (Pillon *et al* 1990). Activation measurements and the corresponding transport simulations have therefore also been carried out at various tokamak experiments. More recent results are available for TFTR (e.g. Barnes *et al* 1996), JT-60U (Hoek *et al* 1995), TEXTOR (Hübner *et al* 1994), JET (e.g. Jarvis *et al* 1991), FTU (e.g. Angelone *et al* 1991) or ASDEX (Bätzner *et al* 1989).
The influence of scattered neutrons on the measured neutron spectra has, in contrast to the situation for the counters and activation measurements, as yet not been simulated for a larger number of measured spectra. This is mainly attributable to modelling difficulties of the plasma neutron source based on measured plasma data. Nevertheless, early results demonstrating the feasibility have been reported for ASDEX (Robouch *et al* 1987). Recently, more detailed theoretical studies are also available (Fieg 1992, Beikert *et al* 1995, Antozzi *et al* 1996 and Källne *et al* 1997).

Several Monte Carlo codes for neutron transport simulation are available such as FURNACE (Verschuur 1983), TRIPOLIS-2 (Brésard *et al* 1991), McBEND (see e.g. Laundy and Jarvis 1993), VINIA-3DAMC (Robouch *et al* 1987) or MORSE (Ragheb and Maynard 1975). However, at present neutron transport calculations are most frequently performed using the 3D Monte Carlo neutron-gamma transport code MCNP (Briesmeister 1993). Therefore, the modelling capabilities, the numerical techniques offered by MCNP and the modelling effort required for actual computations are briefly summarized below:

- *Neutron emission*
  The built-in MCNP neutron source is not versatile enough even to provide a rather simple fusion neutron source model. Therefore, most users have written their own subroutines modelling the neutron emission. In these models, realistic flux surface geometry and anisotropic ion distribution functions are usually not taken into account for simplicity.
- *Neutron cross sections*
  Knowledge on neutron cross sections is based on measurements and is summarized in data banks of evaluated nuclear data such as the ENDF/B–VI system (Rose and Danford 1992) or the FENDL library (see e.g. Cheng *et al* 1996). Typical uncertainties in neutron cross sections are 2-3% for total cross sections and 10-20%

for angular distributions. Recent integral benchmark comparison studies (Cheng *et al* 1994) indicate that the overall influence of the uncertainties of neutron cross section data on the uncertainty of the neutron transport calculation required for the yield determination from activation measurements is about 5%. MCNP is compatible with most evaluated nuclear data systems.

- *Geometry*
  The MCNP geometry modelling concept has been designed in the early 1960's and provides a subset of constructive solid geometry. Modelling is done by directly editing the input that which describes the geometry. Therefore, in most actual calculations, simplified models have been used. Typically, the uncertainty from geometry simplifications constitutes the main contribution in the overall uncertainty of the Monte Carlo result and ranges from 10-20%.
- *Detector response*
  Detector response functions that only depend on energy can directly be modelled with MCNP. For more complex ones, a user-supplied subprogram is required.
- *Neutron tracking*
  Neutron tracking refers to calculating the point of intersection of a ray with a geometry model and is essentially the same as ray tracing in computer graphics. From this point of view, the ray tracing algorithm used in MCNP is rather simple. The computational cost of ray tracing increases strongly when geometries become more complex and therefore it constitutes a limiting factor for geometry complexity.
- *Variance reduction*
  A variety of non-analogous Monte Carlo schemes are offered by MCNP, but few of them are appropriate for the specific problems associated with small detectors. Therefore, several millions of events are usually required to achieve a statistical accuracy of a few percent.

Finally, it should be noted that the typical modelling times for a rather strongly simplified problem presently are in the order of weeks. The typical computer time consumption for a production run is in the order of days on small workstations and the typical overall uncertainty of the Monte Carlo result is about 10-20%.

4. Plasma physics deductions from neutron measurements

There is a variety of plasma physics deductions that can be made using neutron diagnostics. The neutron source strength is an immediate and direct measure of the progress towards the achievement of thermonuclear reactor conditions. Therefore, scaling laws of the neutron emission have been used e.g. to project the fusion rate for D-T plasmas and to explore the machine operation space that optimises the fusion reaction rate. By studying the neutron source decay-time, neutron diagnostics may also be used to investigate the characteristics of fast-particle slowing-down times. Plasma conditions where the fast-particle slowing-down is classical, serve, together with the decomposition analysis of the measured neutron signals, as important test cases in order to validate the simplified kinetic models used in the computational schemes. Neutron diagnostics provide reliable information on basic quantities such as the deuteron density and temperature. For certain plasma conditions, somewhat paradoxically at first, information on the electron temperature can also be obtained. For present experiments, the densities and temperatures deduced from neutron diagnostics can be compared with the experimental results of more conventional diagnostics, thereby validating the analysis procedures. With some ingenuity, particle and thermal diffusivities or, in ICRF heated plasmas, the minority ion concentration can sometimes be deduced. Neutron diagnostics can also be used to detect and study important magnetohydrodynamic (MHD) effects.

4.1. Basic properties of the neutron source strength

4.1.1. Scaling and decomposition analysis

Similar to the scaling systematics of the energy confinement time (see e.g. ITER Confinement Database and Modelling Group, 1995), the D-D neutron emission has been described for several tokamaks by scaling its statistical dependence upon the machine settings. However, despite the usefulness of the different scalings for the various tokamak experiments, an uniform physics-based neutron emission scaling law valid for all tokamak experiments is presently not available. Existing neutron emission scaling laws are only valid for a limited range of experimental conditions at a particular tokamak. In addition, the different physical parameters used in the scalings are often not independent from each other. Empirical scalings of the neutron emission have been reported from PDX (Strachan *et al* 1985) and the larger tokamaks JET (Adams *et al* 1991, Karlsson and Elevant 1995), JT-60U (Nishitani *et al* 1994) and TFTR. At JT-60U a purely theoretical study has also been reported (Niikura *et al* 1988). At TFTR, several analyses have been carried out (Hendel and Jassby 1990, Strachan *et al* 1993, Park *et al* 1994). In Hendel and Jassby (1990), it was recognized that there was some

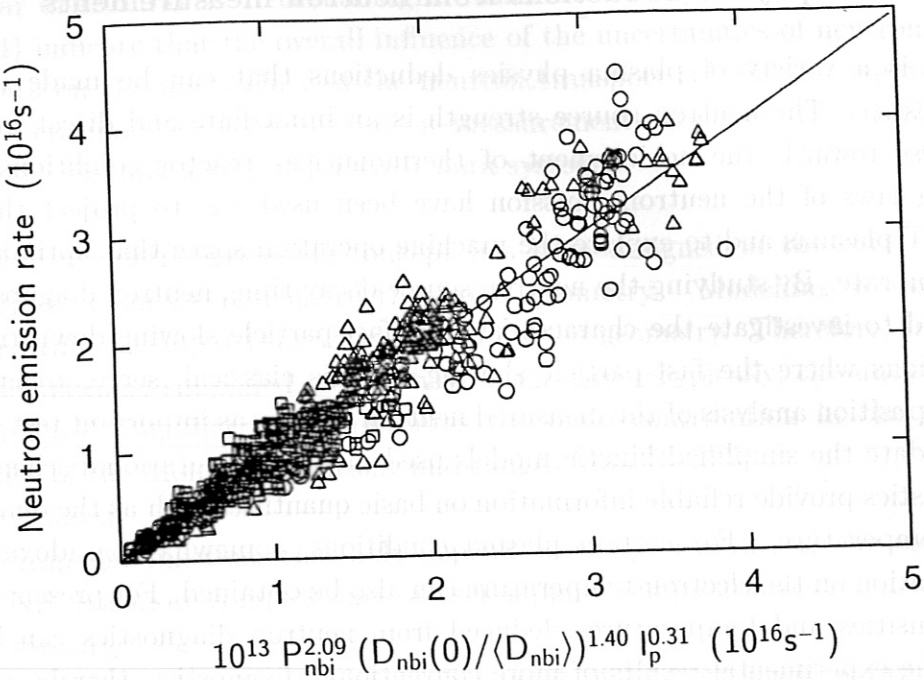

Figure 18. The experimental D-D neutron source strength plotted against the empirical neutron scaling (from TFTR, Park *et al* 1994).

improvement in neutron emission at low plasma current, which was included explicitly in the scaling systematics for the TFTR supershot regime by Strachan *et al* (1993). Then, Park *et al* (1994) investigated the role of the neutral-beam heating profile in scaling of the neutron emission and introduced the heat-deposition profile shaping factor into the scaling systematics for the whole range of experimental conditions on TFTR. The empirically obtained scaling laws had tight fits to the experimental data as shown in figures (18) and (19), where the experimental neutron source strength is plotted against the empirical scaling results for TFTR and JT-60U, respectively. The main scaling laws for PDX, TFTR, JT-60U and JET are:

Strachan *et al*, 1985 (PDX): $$S_n \sim T_e^{1.63} P_{nbi}^{0.99} n_e^{0.19} \tag{66}$$

Park *et al*, 1994 (TFTR): $$S_n = 1.0 \times 10^{13} P_{nbi}^{2.09} \widehat{D}_{nbi}^{1.40} I_p^{0.31} \tag{67}$$

Strachan *et al*, 1993 (TFTR): $$S_n = 0.39\ P_{nbi}^{1.79} \tau_E^{1.87} I_p^{-0.32} \tag{68}$$

Nishitani *et al*, 1994 (JT60U): $$S_n = 0.32\ W_{dia}^2 I_p^{-0.58}$$
$$S_n = 0.0526\ W_{dia}^{1.92} \widehat{n}_e^{0.7} \tag{69}$$
$$S_n = 9.4 \times 10^{-3} P_{abs}^{1.96}$$

Karlsson *et al*, 1995 (JET): $$S_n = 2.07 \times 10^{13} P_{nbi}^{1.47} I_p^{1.66}. \tag{70}$$

Here, S_n is the neutron source strength in $10^{16}s^{-1}$, I_p is the plasma current in MA, P_{nbi} is the injection power in MA, $\widehat{D}_{nbi}$ is the peaking factor of the deposition profile, W_{dia} is the diamagnetic energy content, and P_{abs} is the absorbed heating power defined by $P_{nbi} + P_{oh} - P_{shinethrough}$, respectively. Furthermore, the energy confinement time is $\tau_E = W/(P - \dot{W})$ given in s, where W is the total plasma energy content and P is the deposited input power.

Clearly, the empirical scaling laws given above are not compatible or give contradicting results. For instance, the empirical results at TFTR show that, on one hand, for certain discharges the neutron emission increased with plasma energy content and decreased with increased plasma current (scaling (68). On the other hand, the other scaling law for TFTR (67) predicts that the neutron source strength is increasing with increasing plasma current. For all of the above tokamaks the neutron emission was found to be independent of the injection energy. This can be explained by the reduced particle source rate due to the decreasing neutralization efficiency of the full energy component with increasing injection energy. There are also strong differences in the dependence of the beam power which indicates that the fraction of neutrons produced

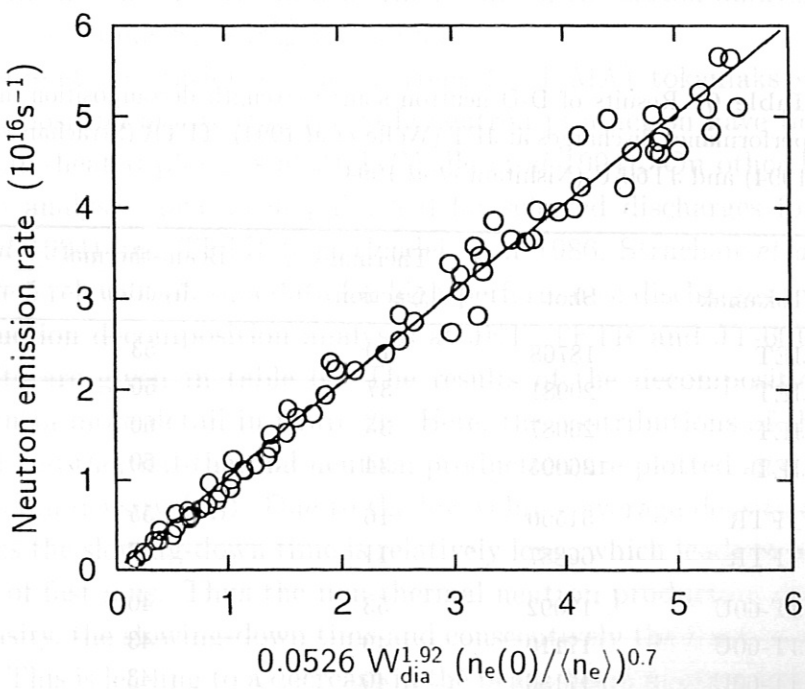

Figure 19. The experimental D-D neutron source strength plotted against the empirical neutron scaling for high-β H-mode discharges on JT-60U (after Nishitani *et al* 1994).

Table 5. Plasma data of discharges selected for recent neutron source strength decomposition analyses for high-performance discharges which have been carried out at JET (Wolle *et al* 1994), TFTR (Strachan *et al* 1993, Budny 1994) and JT-60U (Nishitani *et al* 1994).

Tokamak	Shot	Main beam energies (keV)	NBI power (MW)	S_n ($10^{16}s^{-1}$)	$n_e(0)$ ($10^{19}m^{-3}$)	$T_i(0)$ (keV)	$T_e(0)$ (keV)
JET	18768	80	21	1.2	1.3	17	7.4
JET	20981	80+140	18	3.3	3.6	24	8.6
JET	26087	80+140	15	4.2	3.4	16	8.8
JET	26095	80+140	13	4.1	3.0	22	10.0
TFTR	51550	101	27	3.3	6.8	27	9.5
TFTR	66887	105	24	2.4	6.7	20	9.0
JT-60U	17092	90	27	4.6	6.7	36	11.0
JT-60U	17110	90	27	5.1	5.7	38	12.0
JT-60U	17136	90	33	5.0	6.3	40	11.5
JT-60U	17226	90	33	5.6	6.5	37	10.9

Table 6. Results of D-D neutron source strength decomposition analyses for high-performance discharges at JET (Wolle *et al* 1994), TFTR (Strachan *et al* 1993, Budny 1994) and JT60-U (Nishitani *et al* 1994).

Tokamak	Shot	Thermal fraction	Beam-thermal fraction	Beam-beam fraction
JET	18768	10	53	37
JET	20981	37	56	7
JET	26087	35	60	5
JET	26095	34	60	6
TFTR	51550	16	55	29
TFTR	66887	11	57	32
JT-60U	17092	53	40	7
JT-60U	17110	49	43	8
JT-60U	17136	40	43	17
JT-60U	17226	32	48	20

Table 7. Break down of the time averaged neutron source strength for different JET discharges (after Wolle *et al* 1994, 1995). Shown are the results from NRFPS calculations, TRANSP simulations, and the results from the neutron spectrum analysis.

Shot	thermal fraction			beam-thermal fraction			beam-beam fraction		
	NRFPS	Spectra	TRANSP	NRFPS	Spectra	TRANSP	NRFPS	Spectra	TRANSP
19649	10	10	10	82	78	82	8	12	8
26087	35	42	44	60	58	51	5	0	5
26705	30	32	34	69	68	64	1	0	2
26712	54	52	61	46	48	38	<1	0	1

by beam-beam reactions in the discharges used for the scaling differed considerably. In Hendel *et al* (1990), the neutron emission has been plotted as a function of beam power and the best result occurred with a scaling $S_n \sim P_{nbi}^{1.8}$. This dependence was confirmed again by Strachan *et al* (1993). This scaling with the beam power is similar to the scaling laws for JT-60U as found by Nishitani *et al* and for JET. The JET result given by Karlsson and Elevant (1995) confirms the results of the earlier analysis by Adams *et al* (1991) where a scaling $S_n \sim P_{nbi}^{1.5}$ was found.

For the present generation of high-current (> 1 MA) tokamaks systematic and detailed decomposition analyses of the D-D neutron production have been carried out for neutral-beam-heated plasmas at JET (Wolle *et al* 1994). On other large tokamaks decomposition analyses have been published for selected discharges for JT-60U (e.g. Nishitani *et al* 1994) and TFTR (e.g. Hendel *et al* 1986, Strachan *et al* 1993, Budny 1994). In table 5 relevant plasma data for high-performance discharges recently used for neutron production decomposition analyses at JET, TFTR and JT-60U are compiled and the results are given in table 6. The results of the decomposition analysis for JET are shown in more detail in figure 20. Here, the contributions of the beam-beam, beam-thermal and thermal-thermal neutron production are plotted as a function of the averaged deuteron density $\langle n_D \rangle$. Due to the low volume average density in the analysed JET discharges the slowing-down time is relatively long, which leads to a comparatively large fraction of fast ions. Thus the non-thermal neutron production dominates. With increasing density, the slowing-down time and consecutively the fraction of fast particles is decreasing. This is leading to a decrease in the beam-beam neutron production and an increase in the beam-thermal and the thermal fractions. For the highest neutron source strengths obtained with mixed injection energies, the analysis at JET showed that the beam-beam neutron production can be neglected and each, beam-thermal and thermal neutron production, account for about 50%. With neutral-beam heating, such large

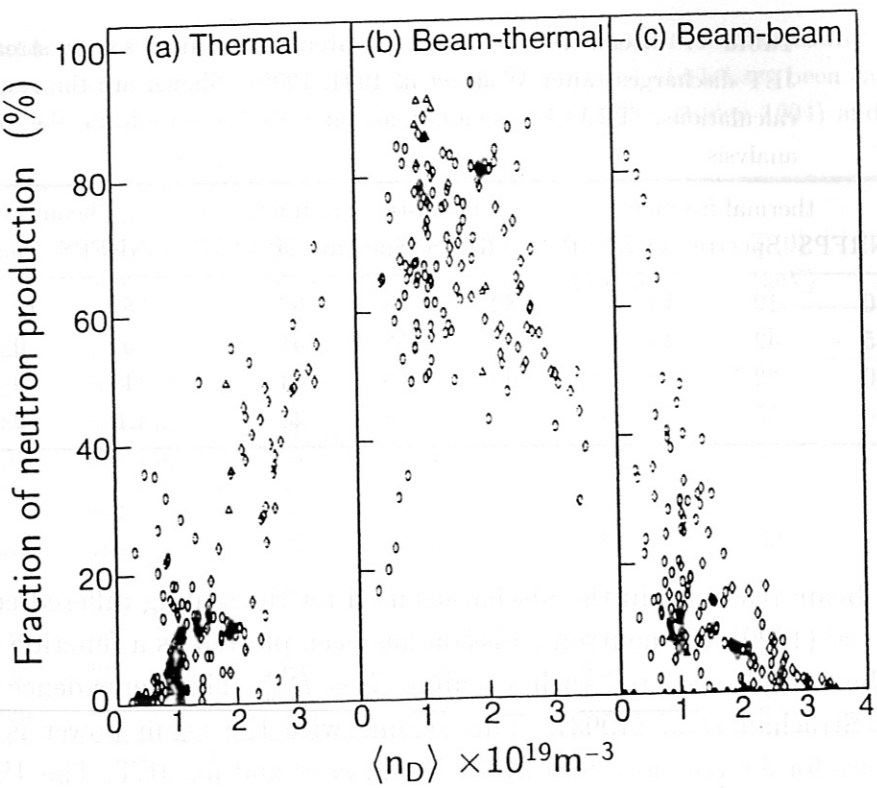

Figure 20. Calculated contributions of the thermal, beam-thermal and beam-beam neutron production from a decomposition analysis for JET (after Wolle *et al* 1994) as functions of the calculated averaged deuteron density. The circles, diamonds and triangles denote 80 keV, mixed 80 and 140 keV and pure 140 keV injection, respectively.

fractions of thermal neutron production can otherwise only be obtained and exceeded in PEP discharges. In the PEP discharges with their high density, the thermal fraction of the neutron production is 50-80%, the beam-thermal neutron production accounts for the rest, and the beam-beam neutron production is negligibly small.

It was demonstrated at JET, that the decomposition of the measured neutron source strength into its different components can under well defined circumstances be achieved by analysing measured neutron spectra (Loughlin *et al* 1989, Olsson *et al* 1993). As an illustrative example this is shown in table 7, where the time-averaged fractions obtained from the analysis of the spectra are compared to the results from the TRANSP simulation and the NRFPS calculation. Clearly, the agreement for the dominating fractions between the different methods is rather good.

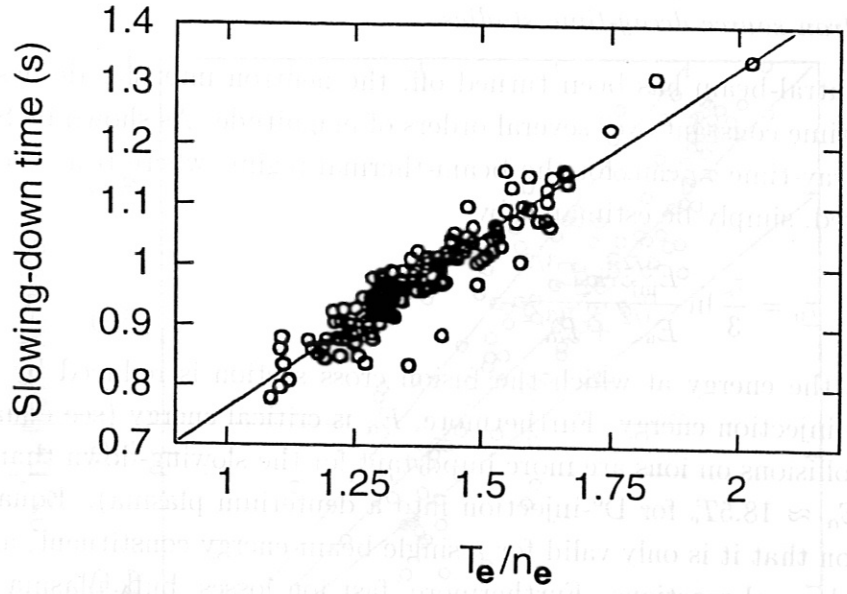

Figure 21. Slowing-down duration of the injected particles with full energy (from TFTR, Strachan *et al* 1993). The proportionality of τ_s to T_e/n_e is expected to be approximately valid when the injection energy is such that ion and electron drag are about equal.

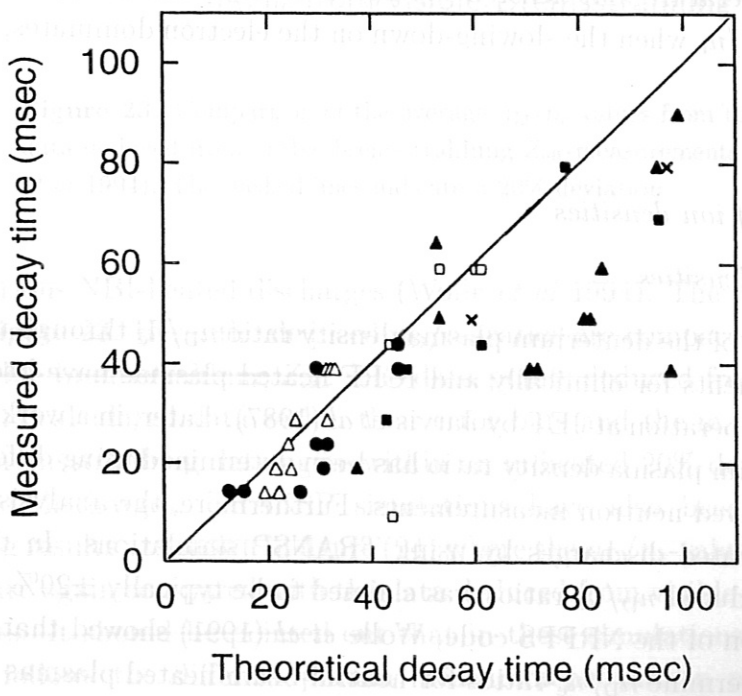

Figure 22. Comparison of the measured and the predicted decay-time of the neutron source strength after beam turn-off for various plasma currents (from TFTR, Hendel *et al* 1986). Crosses, full triangles, full squares, squares, full circles and triangles denote plasma currents of 0.7, 0.8, 1.0, 1.4, 1.8 and 2.2 MA, respectively.

4.1.2. Neutron source decay-time studies

After the neutral-beam has been turned off, the neutron intensity decays with nearly exponential time constant over several orders of magnitude. As shown by Strachan *et al* 1981, the decay-time τ_n can, for the beam-thermal regime where beam-beam reactions can be ignored, simply be estimated by

$$\tau_n = \frac{\tau_s}{3} \ln \frac{E_{inj}^{3/2} + E_\alpha^{3/2}}{E_n^{3/2} + E_\alpha^{3/2}} \tag{71}$$

where E_n is the energy at which the fusion cross section is reduced by $1/e$ from the value at the injection energy. Furthermore, E_α is critical energy (see equation 27), below which collisions on ions are more important for the slowing-down than collisions on electrons ($E_\alpha \approx 18.5 T_e$ for D^0-injection into a deuterium plasma). Equation (71) has the limitation that it is only valid for a single beam-energy constituent, and it includes only beam-thermal reactions. Furthermore, fast ion losses, bulk plasma rotation, and the depletion of the thermal bulk-ion population by the energetic ions are being neglected. Nevertheless, more sophisticated calculations show that the error of the simple analytical expression for the decay-time are only about 25% (Hendel *et al* 1986). This indicates that the fast-ion slowing-down process has essentially the classical variations with electron temperature and density, i.e. T_e/n_e for injection energies below E_α (see figure 21), and $T_e^{3/2}/n_e$ when the slowing-down on the electron dominates, i.e. $E_{inj} > E_\alpha$ (see figure 22).

4.2. Derivation of ion densities

4.2.1. Deuteron densities

The determination of the deuterium plasma density ratio n_D/n_e through neutron source strength measurements for ohmically and ICRF heated plasmas have been reported in the early phase of operation at JET by Jarvis *et al* (1987). Later, in a work by Jarvis *et al* (1990) the deuterium plasma density ratio has been determined using different methods, four of which involved neutron measurements. Furthermore, the analysis was extended to selected NBI-heated discharges by using TRANSP simulations. In these cases the accuracy of the deduced n_D/n_e-ratios was claimed to be typically $\pm 20\%$. Then, using a steady-state version of the NRFPS code, Wolle *et al* (1991) showed that interpretation calculations to determine n_D/n_e-ratios for neutral-beam-heated plasmas can be carried out with good accuracy for discharges with low electron or deuteron density because there the neutron production is very sensitive to small changes of the deuteron density. This has been used in a recent n_D/n_e-analysis at the JET tokamak where the deuterium density was deduced from neutron source strength measurements for a number of time

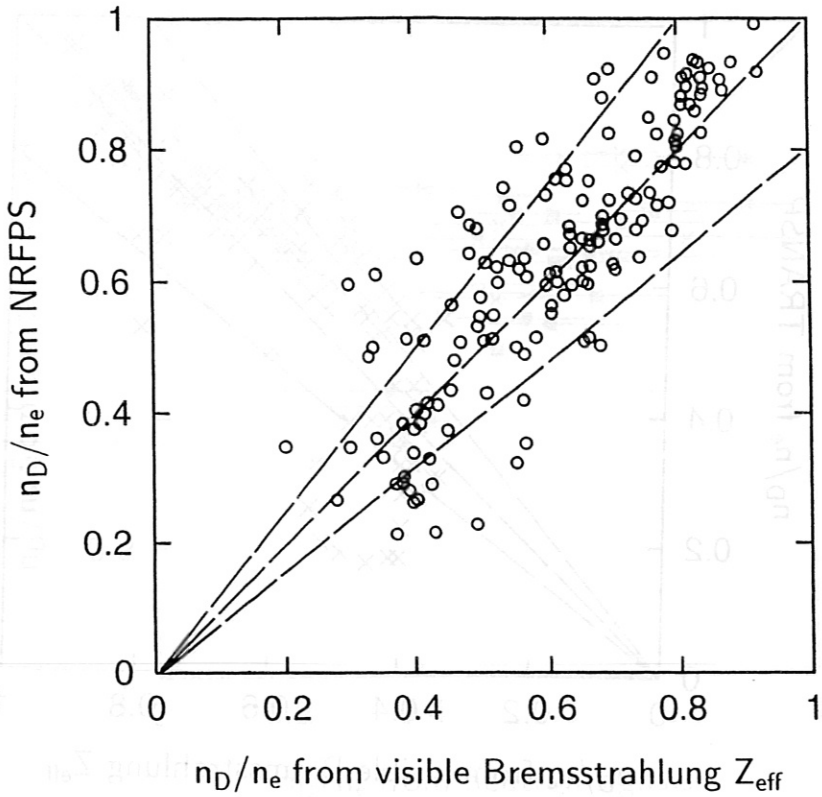

Figure 23. Comparison of the average n_D/n_e-values from the NRFPS analysis with data deduced from visible bremsstrahlung Z_{eff}-measurements (VB) (from JET, Wolle *et al* 1994). The dashed lines indicate a 20% deviation.

points for various NBI-heated discharges (Wolle *et al* 1994). The result of this analysis is shown in figure 23. Here, the deduced n_D/n_e-ratios are compared with data deduced from the visible bremsstrahlung Z_{eff}. The data points deduced from the measured Z_{eff} agree with the calculated data within their error bars and the majority of the NRFPS and visible bremsstrahlung data agree within an indicated 20% deviation.

For these discharges, TRANSP simulations have also been carried out. The corresponding results are shown in figure (24) where the n_D/n_e-values from the TRANSP simulations are again compared with the data deduced from visible bremsstrahlung Z_{eff}-measurements. It should be pointed out that in these simulations, TRANSP for most time points follows the different plasma measurements and in particular the visible bremsstrahlung Z_{eff}, temperature and density measurements closely within their error bars, while output data, such as neutron productions and energy contents, are calculated mainly for consistency validation of the TRANSP analysis. Hence, measured and calculated neutron source strengths can sometimes differ by more than the error bars

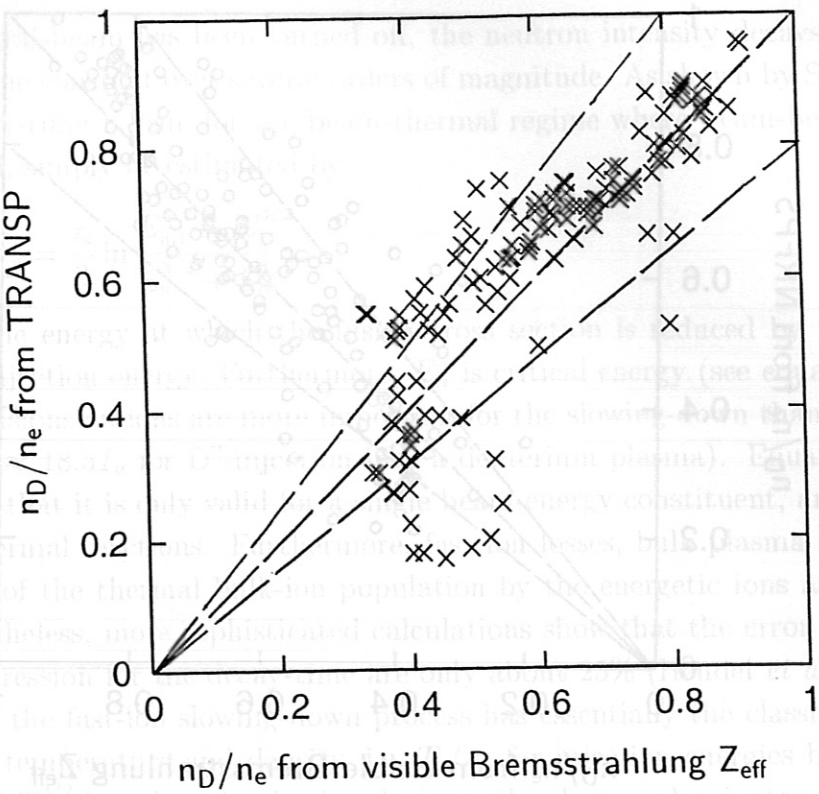

Figure 24. Comparison of the average n_D/n_e-values from the TRANSP simulation with data deduced from visible bremsstrahlung Z_{eff}-measurements (from JET).

of the measured neutron signals.

For selected neutral-beam-heated plasmas, the decomposition analysis of measured neutron energy spectra allows to determine the average thermal deuteron density if the ion and electron temperature profile shapes and the electron density profile shapes are known (Olsson *et al* 1993). However, the analysis has to be restricted to plasmas with comparatively large thermal fraction of neutron production, and plasmas where the spectral shape of the thermal component differs sufficiently from that of the beam-thermal and beam-beam components in order to allow the unambiguous decomposition of the spectra ($T_i < 12$ keV for 80 keV NBI at JET). Results from a spectral analysis carried out at JET are shown in figure 25. The comparison of the n_D/n_e-values from conventional optical diagnostics (visible bremsstrahlung and charge-exchange recombination spectroscopy) with the results of the spectral analysis shows good agreement for conditions which lie inside the normal operating range of these diagnostics.

It should be noted that the determination of deuterium densities out of measured

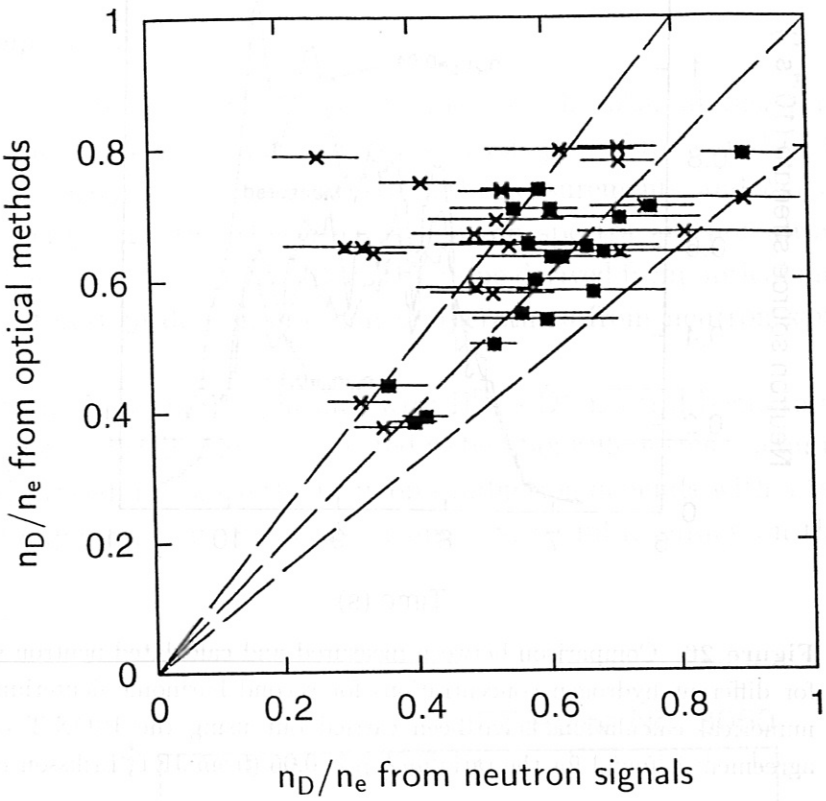

Figure 25. Comparison of n_D/n_e-values from CXRS and/or bremsstrahlung measurements with data deduced from neutron spectrum analysis, associated T_i and neutron source strength (from JET, Olsson *et al* 1993). The statistical errors in n_D/n_e from the spectrum analysis are indicated by $\pm\sigma$ error bars.

neutron signals, neutron source strength or neutron spectra, is the only reliable method available for plasmas with low values of n_D/n_e.

4.2.2. Minority ion concentration during ICRF heating

Interpretation calculations for ICRF heated plasmas are difficult to carry out owing to the complexity of the whole problem. A sophisticated calculation is, as yet, not available as it requires to couple a global wave code (Itoh *et al* 1984, Brambilla and Krücken 1988) for calculating wave propagation and power absorption with suitable Fokker-Planck (Kesner 1978, Succi *et al* 1986) or Monte Carlo (Hellsten *et al* 1995, Kovanen *et al* 1992) codes for calculating the velocity distributions, and to solve the problem by iterations. However, such a combined code is too time-consuming for routine analysis. Therefore, simplified models for calculating the power deposition and velocity

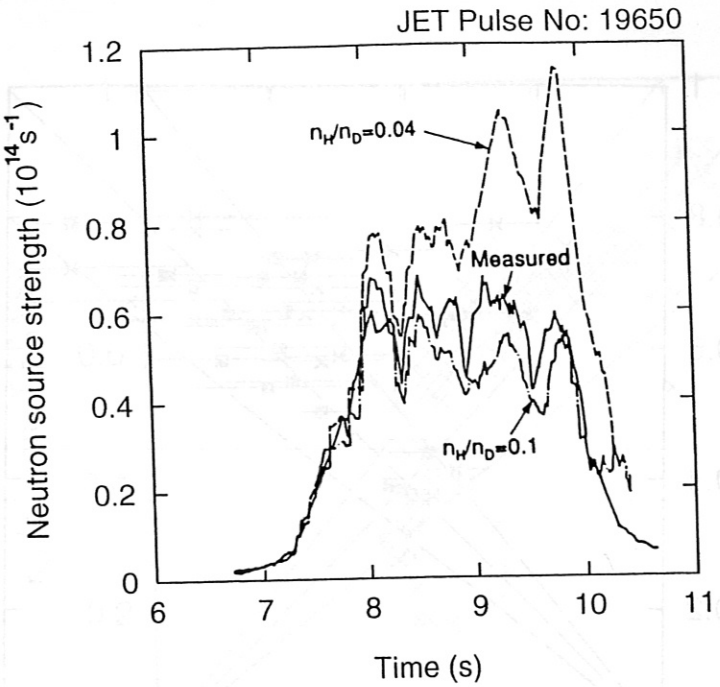

Figure 26. Comparison between measured and calculated neutron source strengths for different hydrogen concentrations for second harmonic deuterium heating. The numerical calculations have been carried out using the PION-T code. The best agreement is found for the ratio $n_H/n_D = 0.06$ (from JET, Eriksson *et al* 1993).

distributions have to be used (cf. subsection 2.2.3). A time-dependent code based on simplified models is, e.g., the recently developed PION-T code (Eriksson *et al* 1993). Simulation results of this code for hydrogen minority heating in deuterium plasmas where the enhancement of the neutron source strength above the thermal level has been used to assess the tail formation of the deuterium during second harmonic heating are available for selected JET discharges. Comparison of the calculated and measured D-D neutron source strengths show that in the presence of ICRH the source strength can be significantly enhanced, as compared to the Maxwellian case. It should be noted that the partition between the power going to second harmonic cyclotron heating of deuterium and fundamental cyclotron heating of hydrogen is very sensitive to the hydrogen concentration. As the experimentally available information on n_H/n_D-ratio is rather uncertain, there is much interest in determining the n_H/n_D-ratio by comparing simulated and measured neutron signals. As an example of such a comparison, a result is shown in figure 26. Here, it is found that the best consistency between measured and calculated neutron signals is obtained for the ratio $n_H/n_D = 0.06$. Lower hydrogen concentrations give a too large neutron source strength, and higher concentrations give a to low source strength.

4.3. Derivation of plasma temperatures

4.3.1. Ion temperature

It is of great interest to determine the ion temperature in tokamak fusion plasmas from measured neutron signals. The most natural analysis procedure would be to determine deuteron densities from neutron source strength measurements and ion temperatures from neutron energy spectra. However, as neutron spectra are not always available, while on the other hand the deuteron density can be derived from optical measurements, there is much interest in determining ion temperatures from neutron source strength measurements.

For ohmically heated plasmas or plasmas with $H^0 \rightarrow D^+$ neutral-beam injection, where the deuteron velocity distribution is expected to be Maxwellian this is a quite simple and straightforward procedure. Since the neutron production depends with a relatively high power on the temperature, it can be determined to useful accuracy on the reasonable

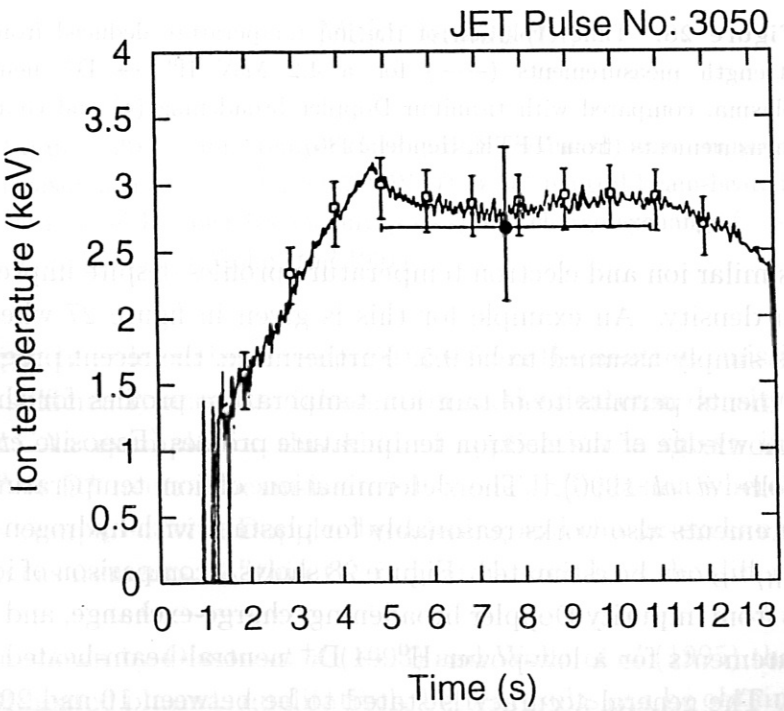

Figure 27. Time evolution of the central ion temperature determined from neutron source strength measurements (——) for an ohmically heated plasma assuming a dilution ratio of $n_D/n_e = 0.5$, compared with neutral particle analysis measurements (□) and the analysis of the neutron spectrum (•) (from JET, Orlinskij and Magyar 1988).

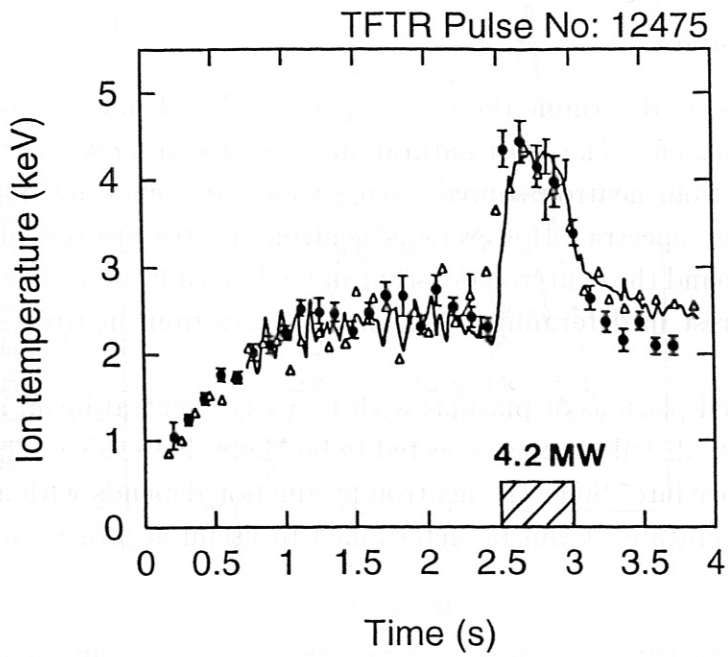

Figure 28. Time evolution of the ion temperature deduced from neutron source strength measurements (——) for a 4.2 MW $H^0 \rightarrow D^+$ neutral-beam-heated plasma, compared with titanium Doppler broadening (•) and charge-exchange (△) measurements (from TFTR, Hendel 1986).

assumption of similar ion and electron temperature profiles despite imprecise knowledge of the deuteron density. An example for this is given in figure 27 where the dilution ratio n_D/n_e was simply assumed to be 0.5. Furthermore, the recent progress in neutron profile measurements permits to obtain ion temperature profiles for thermal plasmas without prior knowledge of the electron temperature profiles (Esposito *et al* 1993, Sasao *et al* 1994, Wolle *et al* 1996). The determination of ion temperature from source strength measurements also works reasonably for plasmas with hydrogen injection if the dilution ratio n_H/n_D can be estimated. Figure 28 shows a comparison of ion temperature determinations from impurity Doppler broadening, charge-exchange, and neutron source strength measurements for a low-power $H^0 \rightarrow D^+$ neutral-beam-heated TFTR plasma (Hendel, 1986). The general accuracy is stated to be between 10 and 20%.

For some non-thermal, $D^0 \rightarrow D^+$ neutral-beam-heated plasmas for which most neutrons originate from thermal production it is, in principle, possible to determine also the ion temperature through computer analysis of measured neutron source strengths (Wolle *et al* 1991). However, even for those plasmas the neutron source strength and the neutron spectra only weakly depend on the ion temperature but quite strongly on the

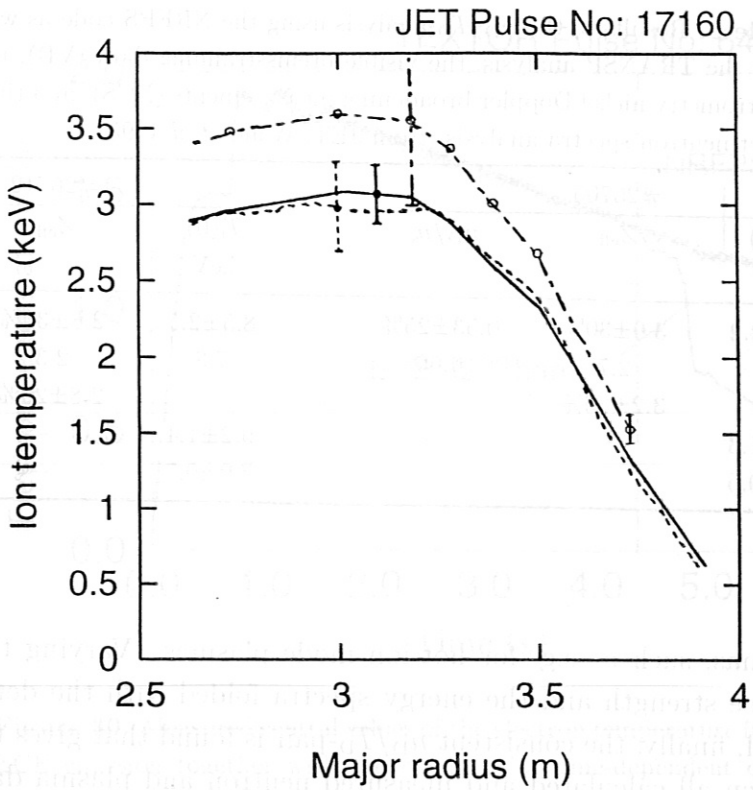

Figure 29. Ion temperature profile deduced from neutron source strength measurements (——) for a 6.7 MW $D^0 \rightarrow D^+$ neutral-beam-heated plasma, compared with nickel Doppler broadening (- - - -) and charge-exchange (— · —) measurements (from JET, after Wolle *et al* 1991).

deuteron density. In order to infer temperatures from the neutron emission one therefore has to rely on sufficiently accurate information on the deuteron density through optical measurements. An example for this kind of application is shown in figure 29 for a moderately $D^0 \rightarrow D^+$ neutral-beam-heated H-mode JET plasma where the deduced ion temperature is compared with Doppler broadening and charge-exchange recombination spectroscopy measurements. Within the indicated error bars the different results agree well.

It has been shown by Olsson *et al* (1993) and Wolle *et al* (1995) that for the case of deuterium NBI-heated plasmas qualitatively better results can be obtained by combining the information of the neutron spectrum and the neutron source strength. Then, the deuteron density can be determined from the measured neutron signals. However, it is necessary to assume similar profile shapes for the ion and electron temperature profiles. Therefore, the analysis is restricted to moderately heated high-density plasmas where ion and electron temperature profiles are similar and cannot be applied for high performance

Table 8. Results of the n_D/T_D-analysis using the NRFPS code as well as the results from the TRANSP analysis, the visible bremsstrahlung data (VB), the X-ray crystal spectrometry nickel Doppler broadening measurements (XCS), and the result from the direct neutron spectra analysis (from JET, Wolle *et al* 1995).

	#26705			#26712		
	$T_i(0)$ keV	Z_{eff}	n_D/n_e	$T_i(0)$ keV	Z_{eff}	n_D/n_e
NRFPS	7.3±2.2	3.0±30%	0.53±25%	8.5±2.5	2.8±30%	0.54±25%
TRANSP	5.5	2.7	0.66	7.8	2.3	0.72
VB	—	3.2±20%	—	—	2.8±20%	—
XCS	8.5±1.3	—	—	9.2±1.4	—	—
Spectra	6.0±0.6	—	—	7.0±0.7	—	—

low-density plasmas, such as e.g. for hot-ion mode plasmas. Varying the ratio T_i/T_e, the neutron source strength and the energy spectra folded with the detector response are simulated and, finally, the consistent n_D/T_D-pair is found that gives the best overall agreement between all calculated and measured neutron and plasma data. In table 8 the result of such an analysis for JET is compared with the results from nickel Doppler broadening measurements, visible bremsstrahlung data and a TRANSP analysis. An error analysis shows that, since the density is quite high, the error bars for the n_D/n_e-ratio, the temperature, and Z_{eff} derived from measured neutron signals, being about 30% are also quite high.

4.3.2. Electron temperature

Somewhat paradoxically at first, for plasmas with low temperatures the neutron production is strongly dependent on the electron temperature. The reason is that the velocity distribution of the fast injected particles directly depends on the slowing-down time for the ions on electrons $\tau_s \sim T_e^{3/2}$. For plasmas with sufficiently low temperatures and high densities, this offers the possibility to determine the electron temperature rather accurately out of the measured neutron source strength.

Usually, the electron temperature at toroidal magnetic fusion devices is accurately measured with high temporal resolution by electron cyclotron emission (ECE) diagnostics (see, e.g. Costley 1982). It is well-known that electron cyclotron emission from a hot magnetically confined plasma occurs at the harmonics $\ell = 1, 2, 3 \ldots$ of the electron gyration frequency. Under normal conditions the emission of the second harmonic is optically thick and is therefore directly proportional to the electron

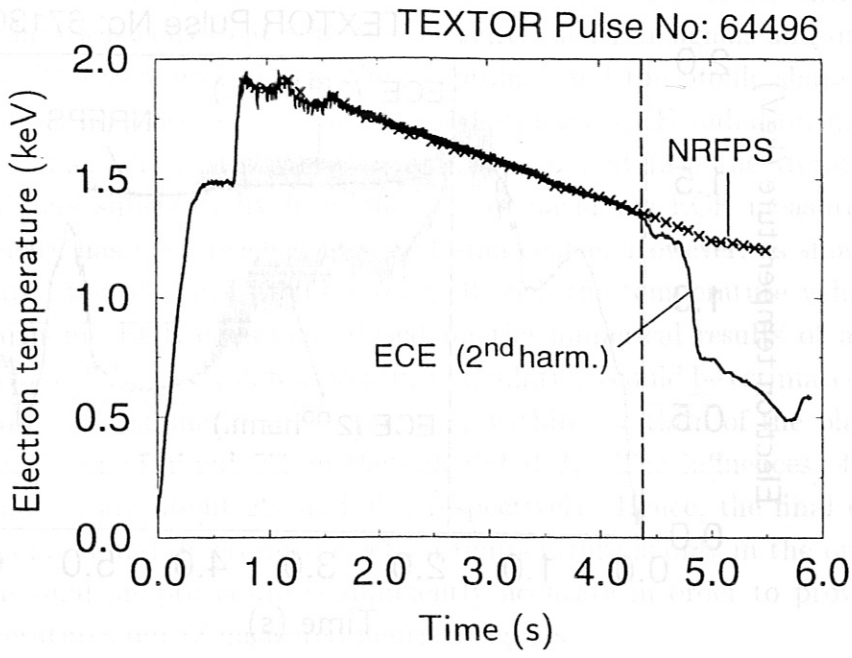

Figure 30. Measured central values of the electron temperature from second harmonic ECE emission together with the results of a time-dependent electron temperature interpretation calculation with the NRFPS code for the TEXTOR discharge #64496 (from Wolle *et al* 1997).

temperature:

$$I(\omega) = I_{\mathrm{BB}} = \frac{\omega^2 k T_{\mathrm{e}}(r)}{8\pi^3 c^2}.$$

The black body emission is prevented as soon as the cut-off frequency overcomes the emission frequency. In these cases, the electron temperature can be determined from the emission at higher harmonics. For the $\ell = 3$ harmonic, the plasma is optically thin ($\tau \leq 1$) and the emission is no longer a black body emission. In this case the emission intensity has to be corrected as (see Costley, 1982)

$$I(\omega) = I_{\mathrm{BB}} \frac{1 - \mathrm{e}^{-\tau}}{1 - R\mathrm{e}^{-\tau}} \tag{72}$$

with R being the reflection coefficient. If the reflection coefficient and the local electron density both are known, the local electron temperature can be calculated from the measured emission of the $\ell = 3$ harmonic.

In tokamaks there can be a small number of discharges where the central electron density exceeds the critical value and the central electron temperatures can no longer be measured directly by using second harmonic ECE emission. Instead, the central electron temperature can be determined out of the measured neutron source strength

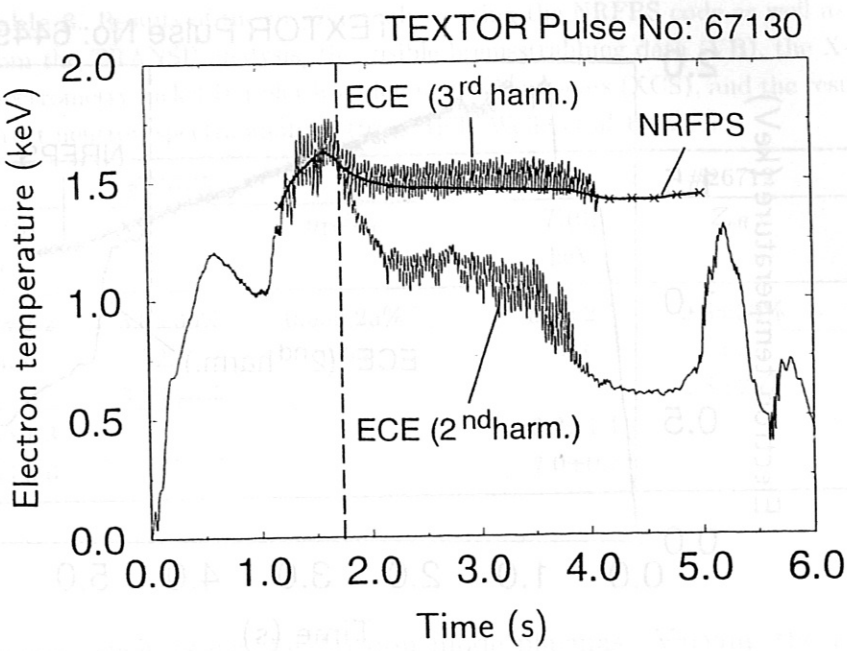

Figure 31. Measured central values of the electron temperature second harmonic ECE emission and from third harmonic ECE emission together with the results of a time-dependent electron temperature interpretation calculation with the NRFPS code for TEXTOR discharge #67130 (from Wolle *et al* 1997).

which provides reliable cross-checks for the temperature measurements by using third harmonic ECE emission.

This kind of application has for the first time be carried out for selected discharges at the TEXTOR tokamak (Wolle *et al* 1997). For standard TEXTOR plasma data with a toroidal field of $B_T = 2.25$ T the critical density is about 9×10^{19} m^{-3} in the plasma centre.

Figures (30) and (31) show the results of time-dependent electron temperature interpretation calculations using the NRFPS code together with the temperature values deduced from second harmonic ECE emission for the discharges #64496 and #67130. In figure (31), the temperature values deduced from third harmonic ECE emission are also shown. At about 4.4 s into discharge #64496, the critical density 8.95×10^{19}m^{-3} for the cut-off of the second harmonic ECE radiation was reached in the plasma centre. For discharge #67130 the critical density was reached in the plasma centre at an early stage at about 1.7 s into the discharge.

In order to determine the central electron temperature out of the measured neutron production a fitted electron temperature profile of parabolic type, i.e. $T_e = T_e(0)(1-\rho^a)^b$ where ρ labels the flux surface, was used. In the first part of the discharges where

reliable T_e-measurements are available, the value of n_D was iterated until the set of input plasma data was consistent with the measured neutron signals and other plasma measurements. The time evolution of the n_D-profiles and the profile shape for T_e was extrapolated into the phase where the second harmonic ECE radiation measurement becomes impossible. As can be seen in figures (30) and (31) the iterated electron temperature differs substantially from the second harmonic ECE measurement after the cut-off density has been reached in the plasma centre. However, as shown in figure (31), the iterated temperature values agree well with the temperature values deduced from third harmonic ECE emission. Based on the numerical results of a sensitivity analysis the errors of the electron temperature calculations could be estimated. For these plasma discharges a systematic 10% error in n_e within one-third of the plasma radius accounts for an error of about 5% in the calculated T_e. The influences of systematic errors in T_i and n_D are about 2% and 4%, respectively. Hence, the final error in the in time extrapolated and determined electron temperature is only in the order of 10%. Therefore, this analysis procedure is sufficiently accurate in order to provide reliable electron temperatures out of measured neutron signals.

4.4. Information on ion thermal diffusivities

Usually, the ion diffusivity χ_i is deduced by transport analysis using transport codes such as TRANSP. For auxiliary heating the value of the deduced ion diffusivity depends very much on the calculated heating power deposition and the measured density, temperature and impurity profiles. Therefore, the estimated uncertainties are in the order of about 50% (see, for example, Watkins *et al* 1990).

Recent progress in neutron emission profile measurements has permitted studies of plasma transport to be carried out in increasing detail. For thermal plasmas, the neutron emission profile data together with measured Z_{eff}-data and electron density profiles can be used to infer ion temperature profiles which can be used to deduce the ion thermal diffusivity for comparison with neoclassical theory. This has been demonstrated by Esposito *et al* (1993) for ohmically and ICRF heated plasmas at JET. Sasao *et al* (1994) used the neutron emission profile data for times just after neutral-beam heating has been switched off. Mainly owing to effects of the ion thermal conductivity, the ion energy content is in this phase decreasing gradually. This allows to obtain the decay rate of the ion stored energy. For simplicity, the thermal neutron emission profiles can assumed to be parabolic, i.e. $Q_{th}(\rho) = Q_{th}(0)(1-\rho^2)^\alpha$, and the exponent κ in the thermal neutron scaling $Q_{th} \sim n_D^2 T_i^\kappa$ can be taken as constant. Then, from the equation describing the local power balance in a one-dimensional, cylindrical plasma

$$\frac{dW_i}{dt} = \frac{3}{2}\frac{n_e(T_e - T_i)}{\tau_{eq}} + \frac{1}{\rho}\frac{\partial}{\partial\rho}\left(\rho n_i(\rho)\chi_i(\rho)\frac{\partial T_i}{\partial\rho}\right) \qquad (73)$$

the rate of change in the ion stored energy can be expressed by

$$\frac{\mathrm{d}W_\mathrm{i}}{W_\mathrm{i}\mathrm{d}t} = \frac{1}{\kappa}\frac{\partial Q_\mathrm{th}(\rho)}{Q_\mathrm{th}(\rho)\partial t} - \left(1-\frac{2}{\kappa}\right)\frac{\partial n_\mathrm{D}}{n_\mathrm{D}\partial t} \tag{74}$$

$$= \frac{n_\mathrm{e}(T_\mathrm{e}-T_\mathrm{i})}{\tau_\mathrm{eq} n_\mathrm{D} T_\mathrm{i}} + \frac{2}{3n_\mathrm{D}T_\mathrm{i}}\frac{\partial}{\rho\partial\rho}\left(\rho n_\mathrm{i}(\rho)\chi_\mathrm{i}(\rho)\frac{\partial T_\mathrm{i}}{\partial\rho}\right) \tag{75}$$

where τ_eq is the equipartition time. Usually, the change in n_e and Z_eff is small and, thus, the second term in equation (74) can be neglected. Furthermore, the first term in equation (75) can also shown to be small. Therefore, for determining χ_i only relative rates of changes in deuteron density, ion temperature and neutron rate, the peaking factor of the ion temperature profile, and the neutron emission rate decay constant $\mathrm{d}Q/Q\mathrm{d}t$ are needed. Results of a χ_i determination are shown in figure 32, where the experimental values for $\rho = 0.3$ are plotted against Z_eff (Sasao *et al* 1994). The experimental χ_i is found to be smallest for $Z_\mathrm{eff} = 2.2$ and is increasing with increasing Z_eff. Also shown are the predictions of neoclassical theory which are much smaller than the experimental values for low Z_eff but increase rapidly. They become comparable with the experimental values for the highest Z_eff obtained.

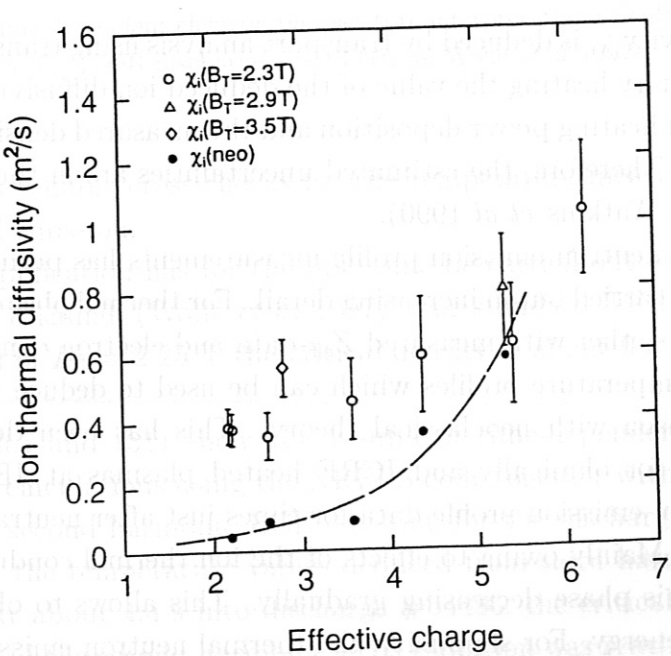

Figure 32. The Z_eff dependence of χ_i values obtained from neutron emission profile analysis of the 'after-glow' behaviour of NBI heated JET single-null plasmas at $\rho = 0.3$. The symbols (○), (△) and (◇) denote toroidal fields of $B_\mathrm{T} = 2.3$, 2.9 and 3.5 T, respectively. The line connects the χ_i values expected from neoclassical theory (•) (from JET, Sasao *et al* 1992).

4.5. Studies of MHD activity

Appreciable effects on the neutron signals have been observed for a variety of MHD activity in auxiliary heated tokamak plasmas. Some detailed investigations are available for an instability that can be identified by its fishbone-like bursts of oscillations in particular in the signals of soft X-ray emission and magnetic pick-up coils, i.e. the so-called fishbone instability (McGuire *et al* 1983). One of the most significant aspects of the fishbone is the observed sharp drop in neutron emission correlated with each burst, corresponding to a substantial loss of energetic ions (Nave *et al* 1991, Sadler *et al* 1990, Strachan *et al* 1985). The first quantitative measurements of the energetic ion confinement time during fishbone events have been deduced at PDX from the time evolution of the neutron emission by Strachan *et al* (1985). Recently, a comprehensive study of the performance deterioration in neutron source strength due to fishbones and low (m,n) MHD modes has been carried out for the high performance operation regime at TFTR (Chang *et al* 1994).

The majority of experimental and theoretical studies of the influence of MHD activity on the neutron emission has been made with respect to one of the most typical forms of MHD activity in a tokamak plasma, i.e. sawteeth. Sawteeth oscillations are periodic relaxation oscillations of the plasma temperature, density and other plasma parameters in the central region of the plasma. They develop when the magnetic winding index on axis, q_0 drops below unity. A slow rise which is determined by transport and heating, is followed by a rapid drop, the sawtooth crash. This crash is triggered by the instability of an internal $m = 1$ kink mode. An understanding of the influence of sawtooth activity on the ions is important for studying and simulating ion transport or fusion performance. Sawtooth activity is expected to play an important role in ITER plasmas (Kolesnichenko *et al* 1994). In recent years, therefore, considerable efforts have been made to improve and to develop the theoretical modelling (see e.g. Kadomtsev 1976, Wesson 1986, Kolesnichenko *et al* 1992, Porcelli *et al* 1996). In addition, detailed experimental studies of the sawtooth oscillations of neutron signals in ohmic and auxiliary heated plasmas have also been carried out at various tokamaks, for example at PLT, DIII-D, and TFTR (Lovberg *et al* 1989), FT (Batistoni *et al* 1990), and JET (e.g. Marcus *et al* 1991, Marcus *et al* 1994). Within this framework it was shown that the predictions of the theoretical model described by Kolesnichenko *et al* (1992) are consistent with available q-profile data and measured neutron data (Anderson *et al* 1993, Anderson *et al* 1994). The model has also been successfully used to predict the observed redistribution of fast ions for large orbit with energetic ^{3}He ions produced by ICRF heating (Ödblom *et al* 1995) and the redistribution of non-thermal confined alpha particle in D-T discharges at TFTR (Stratton *et al* 1996). Wolle (1996) used the model in order to assess the errors introduced in volume-integrated neutron simulation and interpretation calculations for

NBI-heated plasmas due to the neglect of sawtooth oscillations. It was concluded that when deducing deuteron densities from the measured neutron rates, in the post-crash phase the n_D/n_e-ratios are systematically underestimated by up to 10% which is too small to be in obvious disagreement with results from other diagnostics.

This rather simple sawtooth model by Kolesnichenko *et al* (1992) is based on ideal MHD conservation laws and assumes that magnetic flux and the volumes of the connected layers are conserved. According to this model, the post-crash velocity distribution, $f^+(\rho)$, can for a given radius point be written as a weighted mean of contribution of the pre-crash distribution from inside ($f^-(\rho_<)$) and outside ($f^-(\rho_>)$) the $q = 1$ surface as follows:

$$f^+(\rho) = \begin{cases} \nu_<\gamma_< f^-(\rho_<) + \nu_>\gamma_> f^-(\rho_>) & \text{for } 0 \le \rho \le \rho_{\text{mix}}, \\ f^-(\rho) & \text{for } \rho_{\text{mix}} < \rho \le 1, \end{cases} \tag{76}$$

where the weighting factors $\nu_<$ and $\nu_>$ (with $\nu_< + \nu_> = 1$), the radial coordinates and the mixing radius ρ_{mix} all depend on the q-profile before the crash. Furthermore, the factors $\gamma_<$ and $\gamma_>$ account for the deviation of the actual volume elements from cylindrical geometry and $\rho_<$ and $\rho_>$ denote the normalized radii inside and outside the inversion radius which connect during the crash to form the post-crash distribution at radius ρ, respectively. In analogy to equation (76), equations for the temperatures and densities can also be defined. As pointed out by Anderson *et al* (1993), the weighting factors can be calculated using

$$\nu_< = -\frac{\mathrm{d}\rho_<}{\mathrm{d}\rho} \qquad \text{and} \qquad \nu_> = \frac{\mathrm{d}\rho_>}{\mathrm{d}\rho}. \tag{77}$$

The functions $\rho_<(\rho)$ and $\rho_>(\rho)$ follow from the conservation of the flux ($\psi(\rho_<) = \psi(\rho_>)$) and volume.

As an illustrative example, results of a simulation based this model are shown in figure 33. Here, the time evolution of the total neutron source strength S_n for a test case plasma is shown with and without taking sawtooth activity into account (see Wolle 1996). The test case plasma data in this simulation are typical for NBI-heated low-density H-mode discharges at JET. (The decomposition of the neutron source strength into components due to thermal (S_{th}), beam-thermal (S_{bt}) and beam-beam (S_{bb}) neutron production is also shown. As can be seen, in this situation the sawtooth activity in the volume-integrated neutron signal is completely due to the sawtooth activity of the volume-integrated beam-beam component of the neutron production. The level of S_{th} remains unchanged and the beam-thermal neutron source strength is almost unaffected by the sawtooth activity. However, there is a significant reduction in the average level of S_{bb} for the case when sawtooth activity is taken into account as compared to the case when sawtooth activity is neglected. The average level of the

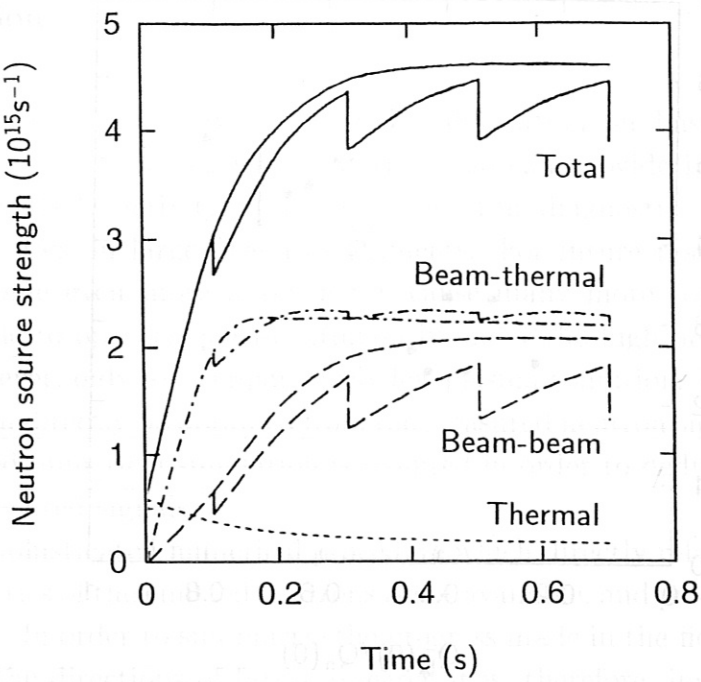

Figure 33. Time evolution of the total neutron source strength (——) for the test case plasma with and without taking sawtooth activity into account and the decomposition into components due to thermal (- - - -), beam-thermal (— · —) and beam-beam (— — —) neutron production. The plasma data were as follows: $T(\rho)\,[\mathrm{keV}] = (T_0 - 0.5)(1-\rho^2)^{2.4} + 0.5$ with $T_\mathrm{i}(0) = 8.5$ keV and $T_\mathrm{e}(0) = 5.5$ keV, $n_\mathrm{e}(\rho)\,[10^{19}\mathrm{m}^{-3}] = 2.0(1-\rho^2)^{1.3} + 0.1$, dilution ratio $n_\mathrm{D}/n_\mathrm{e} = 0.76$ with carbon as impurity ion species, and a constant Z_eff-profile (from Wolle 1996).

total sawtooth-affected source strength stays also below the one without any sawtooth crashes. From these results it can be concluded that the sawtooth oscillations cause no significant variation in the distribution function and the fast-ion content within the mixing radius. (The calculated fast-ion content within the mixing radius was for time points at the end of the sawtooth cycles only by about 2% smaller than that of the sawtooth-free simulation. In addition, the calculated line-integrated neutron spectra in the simulations with and without sawtooth differ only marginally.) The reasons are that, firstly, the sawtooth period (0.2 s) is substantially less than the slowing-down time for the ions on electrons ($\tau_s \approx 1.1$ s) for the conditions studied and, secondly, the average slowing-down time within the mixing radius does not change substantially during the sawtooth cycle. The theoretical results are consistent with the experimental results obtained from tomographic analysis of the neutron emission profiles during the early NBI-phase at JET (Marcus *et al* 1994). This is shown in figure 34 where the post-crash to pre-crash ratios of the axial neutron rates, $Q_\mathrm{n}^+(0)/Q_\mathrm{n}^-(0)$, are plotted versus the fractional pre-crash beam-thermal neutron emission in the plasma centre, $Q_\mathrm{bt}^-(0)/Q_\mathrm{n}^-(0)$

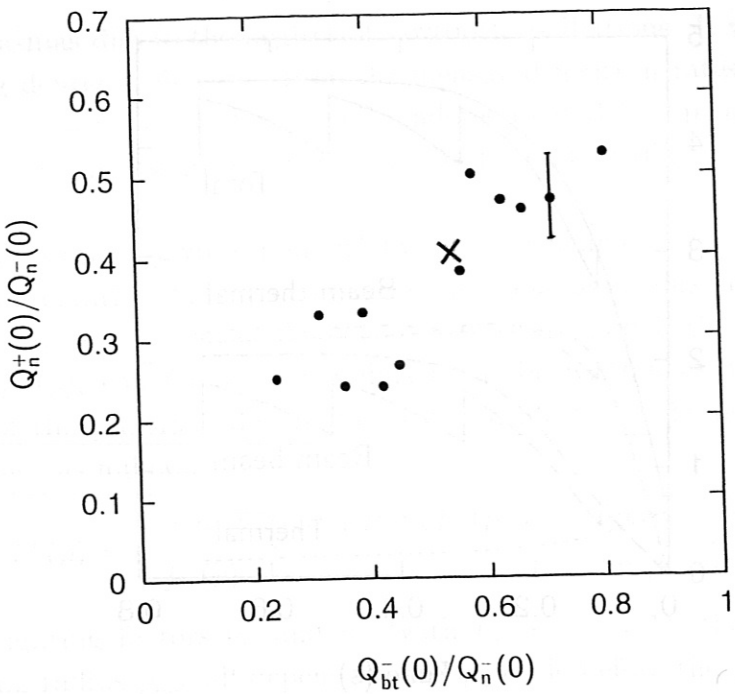

Figure 34. Post-crash to pre-crash ratio of the axial neutron rate, $Q_n^+(0)/Q_n^-(0)$, versus fractional contribution of the beam-thermal neutron emission in the plasma centre just before the crash ($Q_{bt}^-(0)/Q_n^-(0)$). The analysed discharges are low-density NBI-heated H-mode JET plasmas with injection powers of $\approx$ 15 MW (from JET, Marcus *et al* 1994). The cross denotes the result of a theoretical study for a test plasma with similar plasma parameters (from Wolle 1996).

(Marcus *et al* 1994). The cross denotes the result of the theoretical study based on the model after Kolesnichenko *et al* (from Wolle 1996). Finally it was noted by Wolle (1996) that in the plasma centre the fast particle oscillation is out of phase with that of the thermal particles. This has been experimentally confirmed for helium beam-fuelled plasmas with the CXRS diagnostic (von Hellerman *et al* 1993). This behaviour is typical for plasmas with low densities and high injection powers. The reason is that the density profile remains essentially unchanged during the sawtooth crash and the heating profile is rather peaked in the plasma centre. The central layers with rather large fractions of fast particles are connected with the colder layers having larger thermal fractions. In the plasma core, this results in a reduction of fast particles and an increase of thermal ones.

5. Discussion

Neutron diagnostics not only can provide information on basic plasma parameters such as densities and temperatures but they also can provide information on particle transport and MHD activity. Therefore, neutron diagnostics play a major role in plasma diagnostics on large fusion experiments. For future machines, such as ITER, they will become even more important because many more conventional diagnostics are not capable to operate quasi-continuously under the high neutron and gamma-ray fluences. However, only for comparatively few plasma conditions information on plasma parameters can directly be obtained from the measured neutron signals. Instead, in most cases dedicated numerical simulation is required in order to deduce plasma parameters out of the measured signals.
Presently, a sophisticated numerical procedure which directly relates detector signals to physics properties of the emitted neutrons is not available, and progress towards this goal is incremental. In order to summarize the progress made in the field and to obtain some indication of the directions of future research it is, therefore, important to distinguish two categories of numerical simulation, namely 'neutron transport simulations' and 'theoretical simulations'.

Neutron transport simulations are intended to treat the behaviour of a neutron detector system in a tokamak neutron field directly. In present Monte Carlo neutron transport models the variance and therefore the number of Monte Carlo particles required to achieve a certain degree of accuracy is reduced by applying non-analogue Monte Carlo techniques. However, these techniques are not efficient for treating small neutron detectors such as e.g. activation samples. Furthermore, the modelling of complex geometries makes it highly desirable to use geometry models from engineering designs based on present-day CAD systems. However, since the geometry modelling concepts of commonly available neutron transport codes and CAD systems are not compatible, this is presently not feasible.

In the past two decades, the 'theoretical simulations' that are mainly meant to analyse the measured neutron data in order to deduce plasma parameters improved significantly. Partly, this progress was due to improvements of the experimental methods. Mainly, however, the progress is attributable to a better understanding of the measured signals with the help of theoretical simulations based on plasma simulation codes such as TRANSP and spectra codes such as NSPEC (Scheffel 1984) or FSPEC (Sadler and van Belle 1987). Following this trend, NRFPS, the first dedicated time-dependent computer code for directly using measured neutron signals from non-thermal plasmas in order to deduce plasma parameters was recently presented (Wolle *et al* 1994).

Table 9. The main plasma parameters that can be deduced using the measured neutron signals S_n (source strength), Q_n (spatial neutron rate, i.e. neutron emission profile), and Λ_n (neutron spectrum). An estimate of the quality of the data to be expected as compared to the usual standard diagnostics is indicated by the symbols $\ominus$ (poor), $\odot$ (normal), $\otimes$ (good). Further symbols used are: 'p' (profile data), 'f' (feasible, but no published results available), '–' (impossible), '?' (presently questionable), and '??' (presently very questionable).

Plasma type	Measured neutron signal	Parameter deduced						
		n_D/n_e	n_H/n_e	T_i	T_e	$\chi_i(r)$	τ_s	v_{rot}
Ohmic D^+	S_n	$\odot$		$\otimes$				
	$Q_n \cup S_n$	$\odot$ p		$\otimes$ p		$\odot$		
	Λ_n			$\otimes$				
	$S_n \cup \Lambda_n$	$\otimes$		$\otimes$				
	$Q_n \cup \Lambda_n \cup S_n$	$\otimes$ p		$\otimes$ p		$\odot$		
$H^\circ \rightarrow D^+$ NBI	S_n	$\odot$	$\odot$	$\otimes$				
	$Q_n \cup S_n$	$\odot$ p	$\odot$ p	$\otimes$ p		$\odot$		
	Λ_n			$\otimes$				$\otimes$
	$S_n \cup \Lambda_n$	$\otimes$	$\odot$	$\otimes$				$\otimes$
	$Q_n \cup \Lambda_n \cup S_n$	$\otimes$ p	$\odot$ p	$\otimes$ p		$\odot$		$\otimes$
$D^\circ \rightarrow D^+$ NBI	S_n	$\otimes$		–, $\ominus$	$\odot$		$\odot$	
	$Q_n \cup S_n$	$\otimes$ p f		–, $\ominus$ p f	$\odot$ p f	$\odot$ f	$\odot$ p	
	Λ_n			–, $\ominus$	$\odot$			$\otimes$
	$S_n \cup \Lambda_n$	$\otimes$		–, $\odot$	$\odot$		$\odot$	$\otimes$
	$Q_n \cup \Lambda_n \cup S_n$	$\otimes$ p f		–, $\odot$ p f	$\odot$ p f	$\odot$ f	$\odot$ p	$\otimes$
2^{nd} harm. ICRH	S_n	?	$\odot$	??	?		$\odot$	
	$Q_n \cup S_n$	? p	$\odot$ p f	?? p	?? p	??	$\odot$ p	
	Λ_n			??				$\odot$
	$S_n \cup \Lambda_n$	?	$\odot$	??	?		$\odot$	$\odot$
	$Q_n \cup \Lambda_n \cup S_n$	? p	$\odot$ p f	?? p	p ??	??	$\odot$ p	$\odot$

On using such dedicated simulation and interpretation codes based on suitable computational models and concepts, there is a variety of plasma parameters that can be obtained form neutron diagnostics, and many plasma physics deductions can be made. The main plasma parameters that can be deduced using measured neutron signals (source strength, emission profile and neutron spectrum) from deuterium plasmas are summarized in table 9. (Some other plasma data, e.g. fast and thermal densities, are also accessible by using the information of neutron measurements, but they have not been included in the table.) An estimate of the quality of the data to be expected as compared to the usual standard diagnostics is also indicated. Table 9 shows that the quality of the obtained plasma data is in many cases comparable to, or better than the results

from the conventional standard diagnostics.
For plasmas with Maxwellian deuterium velocity distributions, i.e. ohmically heated plasmas and deuterium plasmas with hydrogen injection, the analysis of the measured neutron signals can be carried out by simple analytical means. Here, the main accessible plasma data are the core temperatures and average dilution ratios. From the table one can see that neutron diagnostics can be most effectively used by combining the informations from the different neutron diagnostic systems. For instance, absolute neutron emission profiles are obtained by combining the measured relative spatial emissivity and the absolute neutron source strength. Thus, absolute temperature profiles or dilution profiles can be inferred. Furthermore, it should be noted that by combining the information of the neutron spectra with the source strength or absolute emission profile data, the accuracy of the deduced dilution ratios n_D/n_e or n_H/n_e in general improves and consistent sets of plasma data are being obtained.
The most significant progress in the past decade has been achieved in the simulation and analysis of neutron signals of deuterium plasmas heated by deuterium neutral-beam injection. On analysing the measured neutron data by computational means it is possible to deduce dilution ratios with good accuracy. In addition, electron temperatures can also be obtained. However, the ion temperature in deuterium beam-heated plasmas is for most plasma conditions not accessible through neutron diagnostics, and if it can be deduced the errors are rather large. A higher degree of accuracy can again be obtained by combining the information of the neutron spectra and the neutron source strength. Further important plasma data that can be deduced are the rotation velocity and the ion diffusivity. In addition, information on the slowing-down time can be obtained. It should be noted that for plasmas with $D^\circ \rightarrow D^+$ NBI some applications (e.g. deducing dilution profiles, diffusivity profiles and temperature profiles) are feasible, but published results are, as yet, not available.
Table 9 also shows that the present simulation and analysis methods are mainly applicable to Maxwellian deuterium plasmas and plasmas with deuterium injection. For ICRF heating, suitable simulation and analysis procedures are presently being developed and tested. Therefore, published results from a direct analysis of the measured neutron signals are presently only available for the determination of minority ion concentrations and the slowing-down time scales.

In conclusion, there are in principle two ways in which the field of numerical simulation and analysis of neutron signals can progress, namely (i) by improving and augmenting numerical techniques, and (ii) by providing refined computational models and simulations that help the development of diagnostic methods and improve theoretical data analysis. As far as the first point is concerned, it must be said that in the past two decades technical progress has somewhat slowed down as compared to the preced-

ing years where the subject foundations in the areas of Fokker-Planck codes, neutron transport codes, Monte Carlo or finite element methods were laid.
Therefore, in the near future the main progress in the field will be related to the second point. Here, a main direction of future research is an extension of the analysis procedures to plasma conditions with RF heating. Finally, a clear trend in the field is to amend the analysis procedures for deuterium beam-heated plasmas in order to obtain information on other plasma quantities that are more difficult to measure such as e.g. the injected fast particle source rates or the q-profiles in the sawtooth cycle from neutron measurements.

Acknowledgments

I am grateful to all members of the fusion research community whom I have consulted. In particular, I wish to thank Prof K Hübner for many helpful and stimulating discussions. Thanks are also due to Drs L-G Eriksson and T Elevant for their constructive comments on the manuscript.

References

Adams J M, Balet B, Boyd D A, Campbell D J, Challis C D, Chrisiansen J P, Cordey J G, Core W G F, Costley A E, Cottrell G A, Edwards A W, Elevant T, Eriksson L-G, Hellsten T, Jarvis O N, Lallia P P, Lawson K, Lowry C, Nielsen P, Sadler G, Start D F H, Thomas P R, von Hellermann M and Weisen H 1991 *Nucl. Fusion* **31** 891

Anderson D, Lisak M and Pekkari L-O 1985 *Phys. Fluids* **28** 3590

Anderson D, Core W, Eriksson L-G, Hamnén H, Hellsten T and Lisak M 1987 *Nucl. Fusion* **27** 911

Anderson D, Core W, Eriksson L-G, Hamnén H, Hellsten T and Lisak M 1988 *Physica Scripta* **37** 83

Anderson D, Batistoni P, Lisak M and Wising F 1993 *Plasma Phys. Control. Fusion* **35** 733

Anderson D, Kolesnichenko Ya I, Lisak M, Wising F and Yakovenko Yu V 1994 *Nucl. Fusion* **34** 217

Angelone M, Batistone P, Martone M, Pillon M, Rapisarda M and Rollet S 1991 *Fusion Technol.* **19** 431

Antozzi P, Gorini G, Källne J and Ramström E 1996 *Nucl. Instr. and Meth.* **A 368** 457

Arter W 1995 *Rep. Prog. Phys.* **58** 1

Bätzner R, Hübner K, Ingrosso L, Bosch S, Rapp H, Wolle B, van Calker C, Robouch B V, Kucinski J and Brzosko J S 1989 *Proc. 16th EPS Conf. on Contr. Fusion and Plasma Physics (Venice 1989)* vol 13B, part IV, p 1449

Ballabio L, Gorini G and Kallne J 1997 *Rev. Sci. Instrum.* **68** 585

Barnes C W, Larson A R and Roquemore A L 1996 *Fusion Technol.* **30** 63

Batistoni P, Rapisarda M and Anderson D 1990 *Nucl. Fusion* **30** 625

Beikert G, Wolle B, Jauch Z, Baloui T and Hübner K 1995 *Proc. 22nd EPS Conf. on Contr. Fusion and Plasma Physics (Bournemouth 1995)* vol 19C, part III, p 201

Bernstein I B and Baxter D C 1981 *Phys. Fluids* **24** 108

Bosch H-S and Hale G M 1992 *Nucl. Fusion* **32** 611

Brambilla M and Krücken T 1988 *Nucl. Fusion* **28** 1813

Brésard I, Diop C M, Giancarli L and Gervaise F 1991 *Fus. Eng. Design* **18** 377

Briesmeister J F (Ed) 1993 MCNP – A general Monte Carlo n-particle transport code, Version 4A *Report* LA-12625-M (Los Alamos National Laboratory, Los Alamos, New Mexico)

Brysk H 1973 *Plasma Physics* **15** 611

Budny R V 1994 *Nucl. Fusion* **34** 1247

Chang Z, Fredrickson E D, Callen J D, McGuire K M, Bell M G, Budny R V, Bush C E, Darrow D S, Janos A C, Johnson L C, Park H K, Paul S F, Scott S D, Strachan J D, Synakowski E J, Wieland R M, Zarnstorff M C, Zweben S J and TFTR Team 1994 *Nucl. Fusion* **34** 1309

Cheng E T, Forrest R A and Pashchenko A B 1994 Report on the second international activation calculation benchmark comparison study *Report* INDC(NDS)-300 (International Nuclear Data Committee, IAEA, Vienna)

Cheng E T, Pashchenko A B and Kopecky J 1996 *Fusion Technol.* **30** 1182

Chrien R E, Colestock P L, Eubank H P, Hosea J C, Hwang D Q, Strachan J D and Thompson H R jr 1981 *Phys. Rev. Lett.* **46** 535

Clayton D D 1968 *Principles of Stellar Evolution and Nucleosynthesis* (McGraw-Hill, New York)

Connor J W and Cordey J G 1974 *Nucl. Fusion* **14** 185

Cordey J G and Houghton M J 1973 *Nucl. Fusion* **13** 215

Cordey J G, Core W G F and Sheffield J 1975 *Nucl. Fusion* **15** 755

Cordey J G 1976 *Nucl. Fusion* **16** 499

Cordey J G, Marx K D, McCoy M G, Mirin A A and Resnik M E 1978 *J. Comput. Phys.* **28** 115

Core W G F 1987 A note on the computation of thermonuclear reactivities in plasma-fusion applications *Report* JET-IR(87)11 (JET Joint Undertaking, Abingdon, Oxfordshire)

Core W G F 1993 *Nucl. Fusion* **33** 829

Corrigan G, Muir D G and Tibone F 1992 Neutral beam-plasma interaction in JET: comparison of PENCIL and TRANSP modelling results *Report* JET-R(91)14 (JET Joint Undertaking, Abingdon, Oxfordshire)

Costley A E 1982 *Proc. Int. School Plasma Physics, Course of Diagnostics for Reactor Conditions (Varenna 1982)* p 129

Drosg M and Schwerer O 1987 Production of monoenergetic neutrons between 0.01 and 23 MeV *Handbook of Nuclear Activation Data* (IAEA, Vienna) p 111

Duesing G, Altmann H, Falter H, Goede A, Hange R, Hemsworth R S, Kupschus P, Stork D and Thompson E 1987 *Fusion Technology* **11** 163

Elevant T 1981 *Nucl. Instr. and Meth.* **185** 313

Elevant T, van Belle P, Grosshög G, Hoek M, Jarvis O N, Olsson M and Sadler G 1992 *Rev. Sci. Instrum.* **63** 4586

England A C, Howe H C, Mihalczo J T and Fowler R H 1977 Neutron time behavior for deuterium neutral beam injection into a hydrogen plasma in ORMAK *Report* ORNL/TM-6035 (Oak Ridge National Laboratory, Oak Ridge, Tennessee)

Esposito B, Marcus F B, Adams J M, Conroy S, Jarvis O N, Loughlin M J, Sadler G, van Belle P and Watkins N 1993 *Plasma Phys. Control. Fusion* **35** 1433

Eriksson L-G, Hellsten T and Willén U 1993 *Nucl. Fusion* **33** 1037

Feng Y, Wolle B and Hübner K 1995 *Comput. Phys. Commun.* **88** 161

Fieg G 1992 Monte Carlo calculations with MCNP for the collimation system of the ASDEX-Upgrade He-3 neutron spectrometer *Report* KfK-Primärbericht 31.01.02 P01A (Kernforschungszentrum Karlsruhe, Karlsruhe-Leopoldshafen)

Fiore C L, Boivin R, Granetz R S, Fuller T and Kurz C 1992 *Rev. Sci. Instrum.* **63** 4530

Fowler R H, Callen J D, Rome J A and Smith J 1976 FIFPC: A fast ion Fokker-Planck code *Report* ORNL/TM-5487 (Oak Ridge National Laboratory, Oak Ridge, Tennessee)

Fowler R H, Holmes J A and Rome J A 1979 NFREYA - A Monte Carlo beam deposition code for non-circular tokamak plasmas *Report* ORNL-TM-6845 (Oak Ridge National Laboratory, Oak Ridge, Tennessee)

Freeman R L and Jones E M 1974 Atomic collision processes in plasma physics experiments *Report* CLM-R137 (Culham Laboratory, Abingdon, Oxfordshire)

Galeev A A and Sagdeev R Z 1968 *Soviet Pysics JETP* **26** 233

Gamov G 1928 *Zeitschr. Physik* **51** 204

Gerstel U, Horton L, Summers H P, von Hellermann M and Wolle B 1997 to appear in *Plasma Phys. Control. Fusion* **39** (5)

Goldston R J, McCune D C, Towner H H, Davis S L, Hawryluk R J and Schmidt G L 1981 *J. Comput. Phys.* **43** 61.

Grisham L R, Eubank H P, Kamperschroer J H, Kugel H W, Martin G D, Prechter R E, Prichard jr B A, Williams M D, Winje R A and Wright K E 1985 *Nucl. Instr. and Meth.* **B 10/11** 478

Hale G M and Dodder D C 1980 *Nuclear Cross Sections for Technology*, edited by J L Fowler, C H Johnson and C D Bowman, *Special Publications* 594 (National Bureau of Standards, Washington

DC) p 650

Hawryluk R J 1980 *Proc. International School of Plasma Physics, Course of Physics of Plasmas close to Thermonuclear Conditions (Varenna 1979)* vol 1, p 19

Heidbrink W E 1984 *Nucl. Fusion* **24** 636

Heidbrink W E and Sadler G J 1994 *Nucl. Fusion* **34** 535

Heinrichs G, Schöpf K, Riedler J, Feldbacher R, Heindler M and Kernbichler W 1989 *Proc. 12th Int. Conf. on Plasma Physics and Contr. Nuclear Fusion Res. (Nice 1988)* vol 3, p 459

Hellsten T, Appert K, Core W, Hamnén H and Succi S 1985 *Proc. 12th EPS Conf. on Contr. Fusion and Plasma Physics (Venice 1989)* vol 9F, part II, p 124

Hellsten T, Carlsson J and Eriksson L-G 1995 *Phys. Rev. Lett.* **74** 3612

Hendel H W 1986 *IEEE Trans. Nucl. Sci.* **33** 670

Hendel H W, England A C, Jassby D L, Mirin A A and Nieschmidt E B 1986 *J. Fusion Energy* **5** 231

Hendel H W and Jassby D L 1990 *Nucl. Sci. Eng.* **106** 114

Hinton F L and Oberman C 1969 *Nucl. Fusion* **9** 319

Hinton F L and Hazeltine R D 1976 *Phys. Fluids* **48** 239

Hinton F L and Robertson J A 1984 *Phys. Fluids* **27** 1243

Hinton F L and Rosenbluth M N 1996 *Nucl. Fusion* **36** 55

Hoek M, Nishitani T, Ikeda Y and Morioka A 1995 *Rev. Sci. Instrum.* **66** 885

Hübner K, Bätzner R, Ingrosso L, Koch S, Saghiri A A, Wolle B and Robouch B V 1994 *Proc. 21st EPS Conf. on Contr. Fusion and Plasma Physics (Montpellier 1994)* vol 18B, part III, p 1344

Hutchinson I H 1987 *Principles of plasma diagnostics* (Cambridge University Press)

ITER Confinement Database and Modelling Group 1995 *Proc. 15th Int. Conf. on Plasma Physics and Contr. Nuclear Fusion Res. (Seville 1994)* vol 2, p 525

Itoh K, Itoh S-I and Fukuyama A 1984 *Nucl. Fusion* **24** 13

Janev R K, Boley C D and Post D E 1989 *Nucl. Fusion* **29** 2125

Jarmie N 1986 Requirements for charged-particle reactons cross sections in the D-T, D-D, T-T and D-^{3}He fuel cycles *Report* LA-UP 86-3705 (Los Alamos National Laboratory, Los Alamos, New Mexico)

Jarvis O N, Gorini G, Hone M, Källne J, Sadler G, Merlo V and van Belle P 1986 *Rev. Sci. Instrum.* **57** 1717

Jarvis O N, Gorini G, Källne J, Merlo V, Sadler G and van Belle P 1987 *Nucl. Fusion* **27** 1755

Jarvis O N, Adams J M, Balet B, Conroy S, Cordey J G, Elevant T, Gill R D, Loughlin M J, Mandl W, Morgan P D, Pasini D, Sadler G, Watkins M, van Belle P, von Hellermann M and Weisen H 1990 *Nucl. Fusion* **30** 307

Jarvis O N, Clipsham E W, Hone M A, Laundy B J, Pillon M, Rapisarda M, Sadler G J, van Belle P and Verschuur K A 1991 *Fusion Technol.* **20** 265

Jarvis O N 1994 *Plasma Phys. Control. Fusion* **36** 209

Jassby D L, Barnes C W, Bell M G, Bitter M, Boivin R, Bretz N L, Budny R V, Bush C E, Dylla H F, Efthimion P C, Fredrickson E D, Hawryluk R J, Hill K W, Hosea J, Hsuan H, Janos A C, Jobes F C, Johnson D W, Johnson L C, Kamperschroer J, Kieras-Phillips C, Kilpatrick S J, LaMarche P H, LeBlanc B, Mansfield D K, Marmar E S, McCune D C, McGuire K M, Meade D M, Medley S S, Mikkelsen D R, Mueller D, Owens D K, Park H K, Paul S F, Pitcher S, Ramsey A T, Redi M H, Sabbagh S A, Scott S D, Snipes J A, Stevens J, Strachan J D, Stratton B C, Synakowski E J, Taylor G, Terry J L, Timberlake J R, Towner H H, Ulrickson M, von Goeler S, Wieland R M,

Williams M, Wilson J R, Wong K-L, Young K M, Zarnstorff M C and Zweben S J *Phys. Fluids B* **3** 2308

JET Team 1992 *Nucl. Fusion* **32** 187

Johnson L C, Barnes C W, Krasilnikov A, Marcus F B, Nishitani T and the ITER Joint Central Team and Home Teams 1997 *Rev. Sci. Instrum.* **68** 569

Kadomtsev B B 1976 *Sov. J. Plasma Phys.* **1** 389

Källne J, Gorini G and Ballabio L 1997 *Rev. Sci. Instrum.* **68** 581

Karlsson J and Elevant T 1995 Scaling formulas for DD neutron emission in JET *Report* JET-IR(95)04 (JET Joint Undertaking, Abingdon, Oxfordshire)

Kennel C F and Engelmann F 1966 *Phys. Fluids* **9** 2377

Killeen J, Kerbel G D, McCoy M G, and Mirin A A 1986 Computational methods for kinetic models of magnetically confined plasmas *Springer Ser. Comput. Phys.* (Springer, New York, Berlin, Heidelberg, Tokyo)

Knoll G F 1989 *Radiation Detection and Measurement* (John Wiley & Sons, New York)

Kolesnichenko Ya I, Lutsenko V V and Yakovenko Yu V 1994 *Fusion Technol.* **25** 302

Kolesnichenko Ya I, Yakovenko Yu V, Anderson D, Lisak M and Wising F 1992 *Phys. Rev. Lett.* **68** 3881

Kovanen M A, Core W G F and Hellsten T 1992 *Nucl. Fusion* **32** 787

Ku L P, Hendel H W, Liew S L and Strachan J D 1991 *Fusion Technol.* **19** 418

Lane A M and Thomas R G 1958 *Rev. Mod. Phys.* **30** 257

Laundy B J and Jarvis O N 1993 *Fusion Technol.* **24** 150

Lao L L, Hirshmann S P and Wieland R M 1981 *Phys. Fluids* **24** 1431

Lehner G and Pohl F 1967 *Zeitschr. Physik* **207** 83

Lister G G, Post D E and Goldston R 1976 *Proc. Third Symposium on Plasma Heating in Toroidal Devices (Varenna 1976)* p 303

Lister G G 1985 A fully 3-D neutral beam injection code using Monte Carlo methods *Report* IPP 4/222 (Max-Planck Institut für Plasmaphysik, Garching)

Loughlin M J, van Belle P, Hawkes N P, Jarvis O N, Sadler G and Syme D B 1989 *Nucl. Instr. and Meth.* **A 281** 184

Lovberg J A, Heidbrink W W, Strachan J D and Zaveryaev V S 1989 *Phys. Fluids* **B 1** 874

Lux I and Koblinger L 1990 Monte Carlo particle transport methods: neutron and photon calculations (CRC Press, Boca Raton, Ann Arbor, Boston)

Mandrekas J 1992 Physics models and user's guide for the neutral beam module of the SUPERCODE *Report* GTFR-102 (Georgia Institute of Technology, Atlanta)

Marcus F B, Adams J M, Cheetham A D, Conroy S, Core W G F, Jarvis O N, Loughlin M J, Olsson M, Sadler G, Smeulders P, van Belle P and Watkins N 1991 *Plasma Phys. Control. Fusion* **33** 277

Marcus F B, Adams J M, Bond D S, Hone M A, Howarth P J A, Jarvis O N, Loughlin M J, Sadler G J, van Belle P and Watkins N 1994 *Nucl. Fusion* **34** 687

Matsuda S, Akiba M, Araki M, Dairaku M, Ebisawa N, Horiike H, Itoh T, Kanai T, Kawai M, Komata M, Kuriyama M, Kitamura S, Matsuoka M, Mizuhashi K, Ogha T, Ohhara H, Ohuchi Y, Ohara Y, Okumura Y, Shibanuma K, Shibata T, Shirakata H, Sugawara T, Tanaka S and Watanabe K 1987 *Fusion Eng. and Design* **5** 85

McGuire K, Goldston R, Bell M, Bitter M, Bol K, Brau K, Buchenauer D, Crowley T, Davis S, Dylla F, Eubank H, Fishman H, Fonck R, Grek B, Grimm R, Hawryluk R, Hsuan H, Hulse R, Izzo R,

Kaita R, Kaye S, Kugel H, Johnson D, Manickam J, Manos D, Mansfield D, Mazzucato E, McCann R, McCune D, Monticello D, Motley R, Oasa K, Okabayashi M, Owens K, Park W, Reusch M, Sauthoff N, Schmidt G, Sesnic S, Strachan J, Surko C, Slusher R, Takahashi H, Tenny F, Thomas P, Towner H, Valley J and White R 1983 *Phys. Rev. Lett.* **50** 891

Moran M J and Hall J 1997 *Rev. Sci. Instrum.* **68** 521

Morgan G L and England A C 1975 *Nucl. Instr. and Meth.* **129** 1

Murphy J A 1992 The SNAP user's guide *Report* PPPL-TM-393 (Plasma Physics Laboratory, Princeton University)

Mukhovatov V S and Shafranov V D 1971 *Nucl. Fusion* **11** 605

Nakai S, Nakatsuka M, Fujita H, Miyanaga N, Jitsuno T, Kanabe T, Izawa Y, Norimatsu T, Takagi M, Yamanaka T, Kato Y, Azechi H, Nishimura H, Shiraga H, Nakai M, Tanaka K A, Kodama R, Takabe H, Nishihara K, Mima K, Kitagawa Y, Sakabe S, Yamanaka M, Kosaki Y, Yamanaka C, Sasaki T, Mori Y, Miyazaki K, Nishikawa M, Kan H, Himura T, Soman Y, Ito H, Perlado J M, Alonso E, Munoz E and Sanz J 1996 *Fusion Technology* **30** 625

Nave M F F, Campbell D J, Joffrin E, Marcus F B, Sadler G, Smeulders P and Thomsen K 1991 *Nucl. Fusion* **31** 697

Niikura S, Nagami M and Horiike H 1988 *Fusion Eng. and Design* **6** 181

Nishitani T, Takeuchi H, Kondoh T, Itoh T, Kuriyama M, Ikeda Y, Iguchi T and Barnes C W 1992 *Rev. Sci. Instrum.* **63** 5270

Nishitani T, Ishida S, Kikuchi M, Azumi M, Yamagiwa M, Fujita T, Kamada Y, Kawano Y, Koide Y, Hatae T, Mori M and Tsuji S 1994 *Nucl. Fusion* **34** 1069

Ödblom A, Anderson D, Eriksson L-G and Lisak M 1995 *Nucl. Fusion* **35** 1571

Olsson M, van Belle P, Conroy S, Elevant T and Sadler G 1993 *Plasma Phys. Control. Fusion* **35** 179

Ongena J P H E 1994 *Fusion Technol.* **25** 133

Orlinskij D V and Magyar G 1988 *Nucl. Fusion* **28** 611

Park H K, Bell M G, Tang W M, Taylor, G, Yamada M, Budny R V, McCune D C and Wieland R M 1994 *Nucl. Fusion* **34** 1271

Pekkari L O, Anderson D, Hamnén H and Lisak M 1983 *Nucl. Fusion* **23** 781

Pillon M, Jarvis O N and Conroy S 1990 *Proc. 13th IEEE Symp. on Fusion Engineering (Knoxville 1989)* (IEEE, New York) p 160

Porcelli F, Boucher D and Rosenbluth M N 1966 *Plasma Phys. Control. Fusion* **38** 2163

Ragheb M M and Maynard C W 1975 A version of the MORSE multigrosup transport code for fusion reactors blankets and shields studie *Report* BNL-20376 (Brookhaven National Laboratory, Upton, New York)

Rebut P-H, Chuyanov V, Huguet M, Parker R R, Shimomura Y, and the ITER Joint Central Team and Home Teams 1995 *Proc. 15th Int. Conf. on Plasma Physics and Contr. Nuclear Fusion Res. (Seville 1994)* vol 2, p 451

Riviere A C 1971 *Nucl. Fusion* **11** 363

Robouch B V, Hübner K, Bätzner R, Roos M, Ingrosso L, Rapp H and Wurz H 1987 *Proc. 14th Eur. Conf. on Controlled Fusion and Plasma Physics (Madrid 1987)* vol 11D, part II, p 1298

Rome J A, Callen J D and Clarke J F 1974 *Nucl. Fusion* **14** 141

Rose P F and Danford C C 1992 ENDF-VI formats manual *Report* IAEA-NDS-76 (IAEA, Vienna)

Rosenbluth M N, MacDonald W M and Judd D L 1957 *Phys. Rev.* **107** 1

Rust N, Wolle B, Hübner K, Kick M, Penningsfeld F P, Stroth U and Walter H 1995 *Proc. 22nd EPS*

Conf. on Contr. Fusion and Plasma Physics (Bournemouth 1995) vol 19C, part III, p 137

Sadler G J, Conroy S W, Jarvis O N, van Belle P, Adams J M and Hone M A 1990 *Fusion Technol.* **18** 556

Sasao M, Adams J M, Conroy S, Jarvis O N, Marcus F B, Sadler G and van Belle P 1994 *Plasma Phys. Control. Fusion* **36** 1

Scheffel J 1984 *Nucl. Instr. and Meth.* **224** 519

Scheffel J 1985 Solution to the Fokker-Planck equation for high-energy ions *Report* TRITA-PFU-85-09 (Royal Institute of Technology, Stockholm)

Sivukhin D V 1966 *Coulomb Collisions in a fully ionized Plasma*, in Reviews of Plasma Physics (Consultants bureau, New York) vol 4, p 93

Slaughter D 1985 LINE: A code which simulates spectral line shapes for fusion reaction products generated by various speed distributions *Report* LLNL UCID-20374 (Lawrence Livermore National Laboratory, Livermore, California)

Slaughter D 1986 *Proc. 13th Eur. Conf. on Controlled Fusion and Plasma Heating (Schliersee 1986)* vol 10C, part II, p 293

Smeulders P, Appel L C, Balet B, Hender T C, Lauro-Taroni L, Stork D, Wolle B, Ali-Arshad S, Alper B, de Blank H J, Bures M, de Esch B, Giannella R, König R, Kupschus P, Lawson K, Marcus F B, Mattioli M, Morsi H W, O'Brien D P, O'Rourke J, Sadler G J, Schmidt G L, Stubberfield P M and Zwingmann W 1995 *Nucl. Fusion* **35** 225

Speth E 1989 *Rep. Prog. Phys.* **52** 57

Stix T H 1975 *Nucl. Fusion* **15** 737

Strachan J D, Colestock P, Eubank H, Grisham L, Hovey J, Schilling G, Stewart L, Stodiek W, Stooksberry and Young K M 1979 *Nature* **279** 626

Strachan J D, Colestock P L, Davis S L, Eames D, Efthimion P C, Eubank H P, Goldston R J, Grisham L R, Hawryluk R J, Hosea J C, Hovey J, Jassby D L, Johnson D W, Mirin A A, Schilling G, Stooksberry R, Stewart L D and Towner H H 1981 *Nucl. Fusion* **21** 67

Strachan J D, Grek B, Heidbrink W, Johnson D, Kaye S M, Kugel H W, Le Blanc B and McGuire K 1985 *Nucl. Fusion* **25** 863

Strachan J D, Nishitani T and Barnes C W 1988 *Rev. Sci. Instrum.* **59** 1732

Strachan J D, Bell M G, Bitter M, Budny R V, Hawryluk R J, Hill K W, Hsuan H, Jassby D L, Johnson L C, Le Blanc B, Mansfield D K, Marmar E S, Meade D M, Mikkelsen D R, Mueller D, Park H K, Ramsey A T, Scott S D, Snipes J A, Synakowski E J, Taylor G and Terry J L 1993 *Nucl. Fusion* **33** 991

Strachan J D, Adler H, Alling P, Ancher C, Anderson D, Anderson J L, Ashcroft D, Barnes C W, Barnes G, Batha S, Bell M G, Bitter M, Blanchard W, Bretz N L, Budny R, Bush C E, Camp R, Caorlin M, Cauffman S, Chang Z, Cheng C Z, Collins J, Coward G, Darrow D S, DeLooper J, Duong H, Dudek L, Durst R, Efthimion P C, Ernst D, Fisher R, Fonck R J, Fredrickson E, Fromm N, Fu G Y, Furth H P, Gentile C, Gorelenkov N, Grek B, Grisham L R, Hammett G, Hanson G R, Hawryluk R J, Heidbrink W, Herrmann H W, Hill K W, Hosea J, Hsuan H, Janos A, Jassby D L, Jobes F C, Johnson D W, Johnson L C, Kamperschroer J, Kugel H, Lam N T, LaMarche P H, Loughlin M J, LeBlanc B, Leonard M, Levinton F M, Machuzak J, Mansfield D K, Martin A, Mazzucato E, Majeski R, Marmar E, McChesney, McCormack B, McCune D C, McGuire K M, McKee G, Meade D M, Medley S S, Mikkelsen D R, Mueller D, Murakami M, Nagy A, Nazikian R, Newman R, Nishitani T, Norris M, O'Connor T, Oldaker M, Osakabe M, Owens D K, Park H,

Park W, Paul S F, Pearson G, Perry E, Petrov M, Phillips C K, Pitcher S, Ramsey A T, Rasmussen D A, Redi M H, Roberts D, Rogers J, Rossmassler R, Roquemore A L, Ruskov E, Sabbagh S A, Sasao M, Schilling G, Schivell J, Schmidt G L, Scott S D, Sissingh R, Skinner C H, Snipes J A, Stevens J, Stevenson T, Stratton B C, Synakowski E, Tang W, Taylor G, Terry J L, Thompson M E, Tuszewski M, Vannoy C, von Halle A, von Goeler S, Voorhees D, Walters R T, Wieland R, Wilgen J B, Williams M, Wilson J R, Wong K L, Wurden G A, Yamada M, Young K M, Zarnstorff M C and Zweben S J 1994 *Phys. Rev. Lett.* **72** 3526

Strachan J D, McCauly J S, Munat T, Barnes C W, Budny R V, Jassby D L, Johnson L C, McCune D C and Roquemore A L 1996 *Nucl. Fusion* **36** 1189

Stratton B C, Fonck R J, McKee G R, Budny R V, Chang Z, Wising F and Ödblom A 1995 *Nucl. Fusion* **36** 1586

Stringer T E 1974 *Nucl. Fusion* **14** 685

Stubberfield P M and Watkins M L 1987 Multiple pencil beam *Experimental Department Research Note* DPA(06)87 (JET Joint Undertaking, Abingdon, Oxfordshire)

Sweetman D R 1973 *Nucl. Fusion* **13** 157

Succi S, Appert K, Core W, Hamnén H, Hellsten T and Vaclavik J 1986 *Comput. Phys. Commun.* **40** 137

van Belle P and Sadler G 1987 *Proc. Course and Workshop on Basic and Advanced Diagnostic Techniques for Fusion Plasmas (Varenna 1986)* vol III, EUR 10797 EN, p 767

Verschuur K A 1983 FURNACE calculations for JET neutron diagnostics *Report* ECN-146 (Stichting Energieoderzoek Centrum Nederland, Petten)

von Hellermann M G, Core W G F, Frieling J, Horton L D, König R W T, Mandl W and Summers H P 1993 *Plasma Phys. Control. Fusion* **35** 799

Watkins M J, Balet B, Bhatnagar V P, Cordey J G, Hammett G W, Hellsten T, Keilhacker M, Milora S L, Morgan P D, Sack C, Schmidt G L, Taroni A, Thomas P R, Thomsen K, Tibone F, von Hellermann M and Weisen H 1989 *Plasma Phys. Control. Fusion* **31** 1713

Wesson J A 1986 *Nucl. Fusion* **30** 2545

Wesson J A 1987 Tokamaks (Oxford University Press, Oxford)

Wolle B, Bomba B and Hübner K 1990 *Proc. 17th EPS Conf. on Contr. Fusion and Plasma Heating (Amsterdam 1990)* vol 14B, part IV, p 1516

Wolle B, Eriksson L-G, Hübner K, Morgan P D, Morsi H W, Sadler G and von Hellermann M G 1991 *Plasma Phys. Control. Fusion* **33** 1863

Wolle B, Eriksson L-G, Gerstel U and Sadler G 1994 *Plasma Phys. Control. Fusion* **36** 1051

Wolle B, Gerstel U, Hübner K, Eriksson L-G, Sadler G and van Belle P 1995 *Plasma Phys. Control. Fusion* **37** 1187

Wolle B 1996 *Plasma Phys. Control. Fusion* **38** 889

Wolle B, Feng Y, Koch S, Hübner K and Bätzner R 1996 *Nucl. Instr. and Meth.* **A 368** 425

Wolle B, Helbing S, Krämer-Flecken A, Bonheure G and Van Wassenhove G 1997 *Plasma Phys. Control. Fusion* **39** 541

Wolle B 1997a to appear in *Contrib. Plasma Phys.*

Wolle B, Jauch Z and Eriksson L-G 1997b to appear in *J. Plasma Physics*

Wu T-Y 1966 Kinetic equations of gases and plasmas (Addison-Wesley, Reading, Palo Alto, London, Don Mills)

Yamagiwa M 1992 *Plasma Phys. Control. Fusion* **34** 1503

Zankl G, Strachan J D, Lewis R, Pettus W and Schmotzer J 1981 *Nucl. Inst. and Meth.* **185** 321